Fabrication of the heterogeneous metal-free carbo-catalysts for the removal of organic pollutants

Aminu Magaji

Submitted in accordance with the requirements for the degree of Doctor of Philosophy

The University of Leeds

School of Chemistry

September 2023

I confirm that the work submitted is my own and that appropriate credit has been given where reference has been made to the work of others.

Acknowledgements

My profound gratitude goes to my supervisor, Natalia Sergeeva, for her support, guidance and understanding throughout this project.

I would like to thank my employer Sule Lamido University Kafin-Hausa, Jigawa State, Nigeria for their support and funding my research for good 3 years.

My sincere appreciation goes to my group and colleagues for their support and help.

I would also like to thank all the collaborators who contributed to some of the work in this project and have been attributed with the work they have done.

Finally, I would like to thank my mother, wife, kids and friends for their support and understanding throughout this journey.

Abstract

Carbonaceous materials have shown undisputable promise as catalysts in various applications. The ability to tune key features such as specific surface area and functionality to improve their activity represents a key advantage. This requires the development of general, facile and cost-effective synthetic methods to deliver these multifunctional materials for efficiency, reproduceability and affordability purpose. This work describes the fabrication of a series of graphene-chromophore (dye) systems, fabrication of graphene-chitosan (two-component), graphene-chromophore-chitosan (three-component), as well as the application of graphene-chromophore hybrids using physisorption and photocatalytic activity studies. Two photochemical methods involving 2-step procedure; diazonium salt formation, isolation and storage, followed with functionalization of graphene using with diazonium salt. Other method is *in-situ* production of diazonium salt and subsequent functionalization of graphene in *one-pot* reaction mixture was employed in the fabrication of the graphene-chromophore. It was found that the two-step procedure is limited by the stability of the diazonium salts and thus has a limited application. The *one-pot* method allows preparation of a wide range of different composites in an easy and inexpensive manner. To compare the the grafting rate and performance efficiency of the catalysts, functionalisation of graphene-chromophore-chitosan was conducted in *one-pot* and *2-step* covalent radical procedure, while fabrication of graphene-chitosan was conducted through *one-pot* covalent and non-covalent pathways. Synthesised samples were characterised by a range of methods including electron microscopy and optical analysis such as, X-ray diffraction, gas adsorption, infra-red, UV-Vis and fluorescence spectroscopy. Optical analysis of the UV-vis absorption spectra shows substantial alteration through both bathochromic (red) and hypsochromic (blue) shifts due to introduced functionalities proving successful surface modification. Changes in a peak pattern have been observed in the FTIR spectra of the modified graphene. Further analyses using PXRD, BET and TGA shows evidence of functionalised graphene surface. Lorentz peak fitting and BET surface analysis show about 12-38% increase in the FWHM values and up to 65% decrease in the surface area of the graphene-chromophores compared to

unmodified graphene. TEM analysis reveals an ordered array of chromophores on the surface of the graphene nanoplatelets. Adsorption experiments of the modified graphene using two most common basic dyes (cationic) and one most common weak acidic (anionic) dye as model dyes: methyl blue (MB), rhodamine B (RhB) and methyl orange (MO) were used and showed different range of adsorption capacities: GP-Chr; (38.3 mg/g, 58.19 mg/g and 21.40 mg/g), GP-Acr; (47.9 mg/g, 63.0 mg/g and 33.50 mg/g), GP-Acn; (30.0 mg/g, 61.77mg/g and 16.19 mg/g), GP-Pnz; (32.6 mg/g, 33.15 mg/g and 9.97 mg/g), GP-Fsc; (49.6 mg/g, 63.5 mg/g and 24.75 mg/g) and GP-Thio; (43.5 mg/g, 45.05 mg/g and 14.79 mg/g). Kinetics studies of materials using the same dye models (MB, RhB and MO) were conducted under dark and light illuminations. Performance efficiency of all the catalysts was higher using RhB and MB than MO, this is because the structure of MO is not flat and therefore not favourable for efficient electrostatic interactions such as π-π stacking. However, some catalysts manifested higher removal rate with illumination than in the dark due to photocatalytic activity.

List of Figures

Figure 1.1: Graphene monolayer structure copied from (Ref. 299) 3
Figure 1.2: Surface area and multi-functionality of graphene-based composites photocatalyst (Ref. 300) 4

Figure 1.3: Graphene energy band dispersion in momentum space within simple tight-binding (FMO) theory; Copied from (Ref. 54). 5
Figure 1.4: Schematic illustration of various graphene synthesis techniques. (a) Graphene flake synthesis by mechanical exfoliation form HOPG. (b) Epitaxial graphene growth on metal single crystals. (c) Epitaxial growth of graphene on carbide wafers by graphitization or deposition. (d) CVD synthesis of large area graphene on metal (Ni or Cu) foils. (e) Chemical synthesis of graphene from graphite oxide, copied from Ref (205) 8
Figure 1.5: Bottom-up and Top-down approaches of graphene synthesis copied from (Ref. 155) 9
Figure 1.6: Schematic illustration of chemical vapour deposition (CVD) copied from ref. 301. 11
Figure 1.7: Different synthesis methods of graphene from oxidation of graphite (starting material) to epoxiliation of graphite oxide through; chemical, thermal and electrochemical reduction of graphene oxide, sourced from Ref. (206) 14

Figure 1.8: Origin of chemical reactivity of graphene. (A) Intrinsic reactivity arising from the delocalized π-bonding system. (B) Zigzag and armchair edges. (C) Monovacancy. (D) bending/curved graphene consisting of the dangling bonds, copied from Ref (208) 15
Figure 1.9: a) Illustration of graphene edges b) armchair track and c) zig-zag track and their respective reactivity strength below copied from (Ref. 296) and (Ref. 297) respectively. 17
Figure 1.10: (left) Structures of HGO containing the dangling bonds copied from Ref (202). (right) Schematic illustration bending in graphene (strain) copied from Ref. (203) 17
Figure 1.11: Overview of the various structures of graphene-based nanomaterials (GNs) and the illustration of their covalent and non-covalent functionalisation, copied from Ref. (207) 19

Figure 1.12: Illustration of covalent radical modification of graphene by diazo chemistry copied from (Ref. 298) 21
Figure 1.13: Diels-Alder addition to graphite copied from Ref (210) 22

Figure 1.14: Covalent functionalisation of graphite and GO by Hummer's method, copied from Ref. (211) 23
Figure 2.1: Schematic representation of Photo-induced surface functionalisation via electron transfer copied from Ref (19) 34
Figure 2.2: Illustration of electron grafting of aryl diazonium salt copied from Ref. (111) 35

Figure 2.3: General strategies for fabricating graphene-dye composites: Method A (two-step procedure) and Method B (*in situ* one-pot). 41

Figure 2.5: UV-Vis Absorption spectra of the organic chromophores, graphene and its composites; The black and red coloured spectra appeared in all the graphs (a-f) represents pristine graphene and dye chromophores respectively. a) GP-Chr (yellow), b) GP-Acr (orange), c) GP-Acn (blue), d) GP-Pnz (green), e) GP-Fsc (Olive), and f) GP-Thio (Violet). 44

Figure 2.6: Fluorescence spectra of the graphene composites collected with the excitation wavelength of 350 nm. The coloured lines spectra representing GP-Chr (yellow), GP-Acr (orange), GP-Acn (blue), GP-Pnz (green), GP-Fsc (olive), GP-Thio (violet). 45

Figure 2.7: Normalised PXRD stack spectra (intensity count) of the graphene and its composites; a) The black spectra present in all the graphs represents pristine graphene, and orange spectrum represents GP-Acr composite, b) Blue spectrum, represents GP-Acn composite, c) Green spectrum represents GP-Pnz composite, d) Olive spectrum represents GP-Fsc composite, e) Violet spectrum, represents GP-Thio composite and f) Yellow spectrum represents, GP-Thio composite. 46

Figure 2.8: TEM images and their Fast Fourier Transformations (FFTs) for the samples: (a) GP-Pnz TEM image; (b) GP-Chr TEM image; (c) GP-Fsc TEM image; (d) GP-Thio TEM image; (e) GP-Pnz FFT image; (f) GP-Chr FFT image; (g) GP-Fsc FFT image; (h) GP-Thio FFT image. The areas used to calculate FFT images (e-g) are indicated by a red square in the corresponding TEM images (a-d). 49

Figure 2.9: TGA thermograms for percentage mass loss of graphene, chromophores and the composites; The black and red coloured spectra appeared in all the graphs (a-f) represents pristine graphene and dye chromophores respectively. a) GP-Pnz (green), b) GP-Thio (violet), c) GP-Acn (blue), d) GP-Acr (Orange), e) GP-Chr (yellow) and f) GP-Fsc (olive). 52

Figure 2.10: TGA 1st Derivatives for (a) starting dyes; Chr (black), Acr (red), Acn (blue), Pnz (green), Fsc (purple) and Thio (orange), (b) graphene (black) and graphene composites; Gr (black), Gr-Chr (red), Gr-Acr (blue), Gr-Acn (green), Gr-Pnz (purple), Gr-Fsc (orange) and Gr-Thio (cyan) 53

Figure 3.1: (a) FTIR spectra of chitosan. (b) FTIR spectra of graphene (Gr, black), Graphene-Chitosan physical mixture (Gr-Cht-PM, red) and Graphene-Chitosan covalent mixture (Gr-Cht-CM, blue) 60

Figure 3.2: UV-Vis spectra of graphene (GP, black), Graphene-Chitosan physical mixture (GP-Cht-PM, red), Graphene-Chitosan covalent mixture (GP-Cht-CM, blue). 61

Figure 3.3: PXRD spectra of graphene (GP, black), Graphene-Chitosan physical mixture (GP-Cht-PM, red), Graphene-Chitosan covalent mixture (GP-Cht-CM, blue) and Chitosan (Chit, green). 62

Figure 3.4: SEM Images of graphene samples: (top) graphene platelets (copied from Ref 245), (left) GP-Cht prepared by sonication, and (right) by radical chemistry. 63

Figure 3.5: (a) Weight loss (%) against temperature and (b) normalized 1st derivatives thermogravimetric analysis of graphene (black), GP-Cht composite

prepared by physical mixture (blue) and GP-Cht composite prepared by diazonium chemistry (red) 66
Figure 3.6: FTIR analysis of Graphene (black), Gr-Chr-Cht (red), , Gr-Acr-Cht (blue) and Gr-Gnn-Cht (green) 68
Figure 3.7: UV-Vis absorption spectroscopic analysis of Gr, Chr, Gr-Chr-Cht, Gr, Acr, Gr-Acr-Cht (top) and Gr, Gnn, Gr-Gnn-Cht (bottom) 70
Figure 3.8: PXRD spectra of chitosan (red), graphene (black), Gr-Chr-Cht (blue), Gr-Acr-Cht (green) and Gr-Gnn-Cht (violet) composites 71
Figure 3.9: SEM Images of (top left) GP-Chr-Cht, (top right) GP-Acr-Cht and (bottom) GP-Gnn-Cht prepared by radical chemistry 72
Figure 3.10: (a) Weight loss (%) against temperature and (b) normalized 1st derivatives thermogravimetric analysis of graphene (black), GP-Chr-Cht composite (red), GP-Acr-Cht composite (blue) and GP-Gnn-Cht (green) 73
Figure 3.11: Preparation of graphene-benzamyl-chitosan and graphene-benzoyl-chitosan material via two step approach 76
Figure 3.12: FTIR spectra of pristine graphene (black), GP-ArCOOH (red) and GP-ArCO-NHCht (blue). 77
Figure 3.13: UV-Vis spectra of pristine graphene (black), GP-ArCOOH (red) and GP-ArCO-NHCht (blue) 78
Figure 3.14: PXRD spectra of pristine graphene (black), GP-ArCOOH (red) and GP-ArCO-NHCht (blue) 79
Figure 3.15: SEM images of GP-ArCOOH (left) and GP-ArCO-NHCht (right). 79
Figure 3.16: (a) Weight loss (%) against temperature and (b) normalized 1st derivatives thermogravimetric analysis of graphene (black), Gr-ArCOOH composite (red), Gr-ArCO-cht composite (blue) 81
Figure 4.1: The model and structure methylene blue (MB) copied from Ref. (214) 93
Figure 4.2: The model and structure Rhodamine B (RhB) copied from Ref. (262) 95
Figure 4.3: Illustration of (photo)degradation of dye models 98
Figure 4.4: (a) Standardisation curves prepared by adding 0.01 mL of the corresponding dye stock solution (MB, MO, RhB; 9.44 × 10^{-4} M); (b) Standardisation curves of RhB, MB and MO presented as a function of the dye concentration (M) 102
Figure 4.5: (a) Photostability of MB under visible light, in neutral, basic, and acidic pH illuminated by Xenon lamp @75W for 30 min, (b) Self-degradation (photolysis) of MB under neutral and 75W and 150W visible illumination for 120 min. 104
Figure 4.6: (a-f) Plots of MB absorption intensity at 650 nm against the volume of added catalyst stock solution (50 - 200µL or 0.05 - 0.2 mL) for 20 min at time interval of 5 min: a) GP-Chr (AM1), b) GP-Acr (AM2), c) GP-Acn (AM15), d) GP-Pnz (AM16), e) GP-Fsc (AM21), f) GP-Thio (AM22). 107
Figure 4.7: Average adsorption intensities of the adsorbates: (a) Mass loading of Methylene blue (MB),(b) Mass loading of Rhodamine B (RhB) and (c) Mass loading of Methyl Orange (MO), 0.01-0.1mL against constant concentration (0.0323 g/L) of the catalyst 111
Figure 4.8: a,c and e right) are summary of adsorption capabilities of MB, MO and RhB dyes for GP modified samples (0.0323 g/L) studied by spectrophotometric method monitoring absorbance decreases at 464 nm (MO), 664 nm (MB) and 553 nm (RhB) over 120 min. (b, d and f left) are linear adjustment of pseudo-second

order kinetic model.(a-f) colours represents the following composites; GP-Chr (red), GP-Acr (blue), GP-AcnOH (green), GP-Pnz (purple), GP-Fsc (orange) and GP-Thio (cyan). 113
Figure 4.9: (a-f) Average dye removal calculated for MB (blue), MO (orange) and RhB (red) monitored over 120 min in the dark in the presence of the catalyst (0.0323 g/L). and desorption of the dye upon addition of EtOH (D-Dyes). Graphs (a-f) represents dark activities of; a) GP-Chr, b) GP-Acr, c) GP-Acn, d) GP-Pnz, e) GP-Fsc, f) GP-Thio. 116
Figure 4.10: Photoinduced removal of MB (blue), MO (orange) and RhB (red) by the composites monitored during 120 min under white light illumination. Plots of average remaining dye against time; and desorption of the dye upon addition of EtOH (D-Dyes). Graphs (a-g) represents Light activities of; a) GP, b) GP-Chr, c) GP-Acr, d) GP-Acn, e) GP-Pnz, f) GP-Fsc, g) GP-Thio. 118

List of Tables

Table 2.1: Summary of XRD data of the (002) peak and BET data for GP and the modified samples. 47
Table 2.2: The total %mass loss and the inflection temperatures of (T_i) for the graphene composites and their corresponding starting dyes. (f=fast; s=slow process) 53
Table 3.1: Summary of BET data of two-component system and TGA values recorded at two key regions with inflection temperatures T_1 and T_2. 66
Table 3.2: Summary of BET data of two-component system and TGA values recorded at two key temperatures (T_1 and T_2) regions. 74
Table 4.1: Summary of experimental molar absorptivity co-efficient (e), optimal concentrations (OC), and the transmittance (T) of dye solution at OC. 102
Table 4.2: Calculated q(t) values in mg/g for the range of concentrations (g/L) of the hybrid materials recorded at 5 min, 10 min, 15 min and 20 min for the MB adsorption. 107
Table 4.3: Summary of MB removal-desorption studies for GP and the modified samples under light (L) and dark (D) conditions. 119

Abbreviations

Abs	Absorbance
Can	7-Aminoanthraquinone
Acr	9-Aminoacridine
AFM	Atomic Force Microscopy
AM1	Graphene-2-Methylchromone
AM2	Graphene-Acridine
AM15	Graphene-Anthraquinone
AM16	Graphene-Phenazine
AM21	Graphene-Flouresceimine
ASGM	Artisanal Small-scale Gold Mining
BET	Brunauer-Emmett Teller (Theory)
BOD	Biological Oxygen Demand
CB	Conductance Band
Chr	7-Amino-2-methylchromone
COD	Chemical Oxygen Demand
CNT	Carbon nanotube
CVD	Chemical Vapour Deposition
DMF	Dimethylformamide
DFT	Density Function Theory
DMF	Dimethylformamide
DMSO	Dimethylsulphoxide
DOS	Density of States
Fsc	5-Aminofluorescein
GCMS	Gas Chromatography Mass Spectroscopy
GP	Graphene nanoplatelet
GNs	Graphene Nanomaterials
GO	Graphene Oxide
HOMO	Highest Occupied Molecular Orbital
FTIR	Fourier Transformed Infrared
LED	Light Emitting Diode
LPE	Liquid-phase Exfoliation
LUMO	Lowest Unoccupied Molecular Orbital
MB	Methylene Blue
MO	Methyl Orange
MWCNT	Multi-Walled Carbon Nanotube
m/z	Mass/Charge
NEXAFS	Near Edge X-ray Absorption Fine Structure
NMR	Nuclear Magnetic Resonance
ORR	Oxygen Reduction Reaction
Pnz	Aminophenaine (Neutral Red)

PXRD	Powder X-Ray Diffraction
Ref.	Reference
rGO	Reduced Graphene Oxide
RhB	Rhodamine B
ROS	Reactive Oxygen Species
SEM	Scanning Electron Microscopy
STM	Scanning Tunneling Microscopy
TA	Terephthalic Acid
TDS	Total Dissolved Solids
TEM	Transmission Electron Microscopy
TFA	Trifluoroacetic Acid
TGA	Thermo-Gravimetric Analysis
Thio	Aminothionine
UHV	Ultra-high Voltage
ULAB	Used Lead Acid Battery
UV	Ultraviolet
UNWWD	United Nation World Water Development
VB	Valence Band
XPS	X-ray Photoelectron Spectroscopy

Table of Contents

Acknowledgements i

Abstract ii

List of Tables viii

Abbreviations ix

CHAPTER 1 1

1.0 Introduction to Research 1

1.1 Graphene 3

1.2 Key Properties of Graphene 4

1.3 Synthesis of Graphene 7

1.4 Bottom-up Approach 9

1.5 Top-down Approach 12

1.6 Reactivity of Graphene 14

1.7 Functionalisation of Carbon Materials by Electron Transfer Chemistry 18

1.8 Covalent Functionalisation of the Graphitic Surface 20

1.9 Introduction to Polymers 24

1.10 Naturally Occurring Polymers 25

1.10.1 Chitin 26

1.10.2 Chitosan 27

1.11 Justification for Research 28

1.12 Aim and Objectives 29

Covalent radical modification of graphitic surface with organic chromophores 31

2.1 Abstract 31

2.3 Diazonium Chemistry in Graphitic Surface Modification 33

2.4 Covalent Radical Functionalisation Using Visible Light Chromophores 37

2.5 Materials and Methods 39

2.5.1 General procedure to fabricate graphene-dye systems. Method A.[20] ... 40

2.5.2 General procedure to fabricate graphene-dye systems. Method B..... 40

2.6 Results and Discussion 41

2.6.1 Analysis by Fourier Transform Infrared Spectroscopy (FTIR)..... 42

2.6.2 Analysis by UV-Visible Absorption Spectroscopy 43

2.6.3 Analysis by Fluorescence Spectroscopy 45

2.6.4 Analysis by Powder X-Ray Diffraction (PXRD) 45

2.6.5 Analysis by Brunauer-Emmett-Teller (BET) 47

2.6.7 Analysis by Transmission Electron Microscopy (TEM) 48

2.6.8 Thermogravimetric Analysis (TGA)..... 51

2.7 Summary..... 54

2.8 Conclusion 55

CHAPTER 3 56

Covalent and Non-covalent Functionalisation of Graphitic Surface by Chitosan: Two- and Three Component Systems..... 56

3.1 Abstract..... 56

3.2 Non-Covalent Functionalisation of Graphitic Surfaces 56

3.3 Materials and Methods 57

3.3.1 Two-Component System 57

3.3.2 Three-Component System 58

3.4 Results and Discussion 59

3.4.1 Two-component system - Graphene-Chitosan 59

3.4.1.1 Analysis by Fourier Transform Infrared Spectroscopy (FTIR) and UV-Vis Absorption Spectroscopy 59

3.4.1.2 Analysis by Powder X-Ray Diffraction (PXRD) and Scanning Electron Microscopy (SEM) 61

3.4.1.3 Thermogravimetric Analysis (TGA) 64

3.4.2 Three-component system: Graphene-Chitosan-Chromophore 67

3.4.2.1 Analysis by Fourier Transform Infrared Spectroscopy (FTIR) and UV-Vis Absorption Spectroscopy 68

3.4.2.2 Analysis by Powder X-Ray Diffraction (PXRD) and Scanning Electron Microscopy (SEM) 70

3.4.2.3 Thermogravimetric Analysis (TGA) 72

3.4.3 Three-component system: Graphene-Linker-Chitosan (Gr-ArCO-Cht) 75

3.4.3.1 Analysis by Fourier Transform Infrared Spectroscopy (FTIR) and UV-Vis Absorption Spectroscopy 76

3.4.3.2 Analysis by Powder X-Ray Diffraction (PXRD) and Scanning Electron Microscopy (SEM) 78

3.4.2.3 Thermogravimetric Analysis (TGA) 80

3.5 Summary 82

3.6 Conclusions 82

CHAPTER 4 85

4.0 Physisorption and Photocatalytic Study 85

4.1 Abstract 85

4.2 Heterogeneous Photocatalysis 86

4.3 Examples of Multicomponent Heterogeneous Photocatalytic Systems 87

4.4 Physisorption and Chemisorption 89

4.5 Models of Adsorption and Adsorption Isotherms 90

4.6 Adsorption Kinetics to Study Dye Removal 90

4.7.1 Dyes as Model Systems to Study Environmental Pollution 93

4.8 Materials and Methods 96

4.8.1 Preparation of the Stock Solutions of Dyes (pollutants) and Hybrids 96

4.8.2 Spectrophotometric Experiments 96

4.8.3 Spectrophotometric Study of Dye Photostability 97

4.8.4 Preparation of Standardisation curve 97

4.8.5 Determination of Optimal Loading of the Hybrids using MB as Dye Model 98

4.8.6 Initial Catalyst Loading 98

4.8.7 Kinetic Study 98

4.9 Results and Discussion 101

4.9.1 Determination of Optimal Concentrations of the Model Dyes: Standardisation Curve 101

4.9.2 Photostability of the Model Dyes Under Different Illumination and pH Conditions 103

4.9.3 Determination of Optimal Mass Loading of Graphene-Based Materials 105

4.9.4 Optimal Loadings of the Catalysts Using MB as the Dye Standard 105

4.9.5 Adjusting the Optimal Concentration of MB, RhB and MO Dyes for the Optimised Catalyst Loading 110

4.9.6 Kinetics Study 112

4.9.7 Adsorption Study of the Dye Models 112

4.9.8 Photodegradation of Model Dyes: MO, RhB and MB 116

4.10 Summary 121

4.11 Conclusions 122

5 Thesis Conclusion and Future Work 123

References 125

CHAPTER 1

1.0 Introduction to Research

Industrial growth and its environmental implications, especially to water sources, has become an overwhelming problem of the world and a challenge for researchers to come up with a viable solution. Water is the most essential natural resource on Earth, vital for animal and plant life. Although 70% of Earth is covered by water, only 3% of it is freshwater suitable for our consumption and the mismanagement of this scarce commodity by human actions is alarming [38]. Worldwide, rapid growth in human population brought about industrial revolution as well as the development of new technologies to reinforce the natural resources of livelihood. While this might be a relief for survival however, its implications such as climate change, water pollution and consequently, drought [37] becomes life threatening and a source of concern. According to the United Nation World Water Development (UNWWD) report, about 440 million people in the world do not have access to quality water, and the industrial demand of water will rise to 400% by 2050 [39]. A more recent report by the UNWWD (2019) shows that by the year 2050, more than 5 billion people in the world will be affected by the shortages of water due to climate change, consumption, and pollution.

Industrial effluents, oil spillage, mining activities, agricultural practices, Lead-Acid battery recycling etc. are known to be the main causes of water pollution [91]. Organic pollutants resulting from polymer, colorant, leather, textile, drug, food industries, and phenolic contents of crude oil, pesticides have been the major threat to the aquatic environment, as well as human health. Synthetic dyes are usually designed for specific function or application and therefore, have Improved properties and more advantageous than the

natural ones, however, their increased stability to light, temperature, chemical and microbial degradation are major threat for aquatic life and human health. [37, 270-271]

Dye industries together with other nine industries such as used lead acid battery (ULAB), mining and ore processing, lead smelting, tanneries, artisanal small-scale gold mining (ASGM), industrial dumpsites, industrial estates, chemical manufacturing, and product manufacturing, have been identified as the top 10 industries responsible for endangering the lives of about 200 million people in low- and middle-income countries [91]. The major source of dyestuff waste discharged into the environment comes from textile industries and constitutes a significant percentage (17-20%) of industrial effluents worldwide of about 200,000 tons annually. [91, 271-272]

Because of the complexity of the synthetic organic pollutants, the traditional processes such as adsorption, chlorination, ozonation and flocculation are insufficient options to treat these effluents [1-2] to total mineralization. Other factors reducing quality of water also include high alkalinity, biological oxygen demand (BOD), chemical oxygen demand (COD) and total dissolved solids (TDS) [1, 37, 93]. A more economic, and efficient method for the treatment of these pollutants have been discovered, among which heterogeneous photocatalysis (see chapter 4) is prominent for its potential in water treatment.[1-2, 25, 29, 37].

1.1 Graphene

Graphene is a single monolayer of sp^2 hybridized carbon atoms in a densely ordered honey-comb crystal lattice, from which carbon-based materials of various dimensions, e.g., fullerenes (0D), nanotubes (1D), and graphitic materials (2D and 3D), can be built up [4,31]. (figure 1.1) It is considered as a new member of the carbon materials family, exhibiting unique properties such as significant carrier mobility (200,000 $cm^2v^{-1}s^{-1}$) at room temperature, large surface area (2630 m^2g^{-1}), Young modulus (~1.0 Tpa), along with superior thermal conductivity (~5000 W $m^{-1}k^{-1}$), high optical transparency (~97.79%), and good electrical conductivity. [4, 34, 59, 273]. These extraordinary properties make graphene a highly applicable and important component in areas of catalysis, optical electronics, photovoltaic systems, and

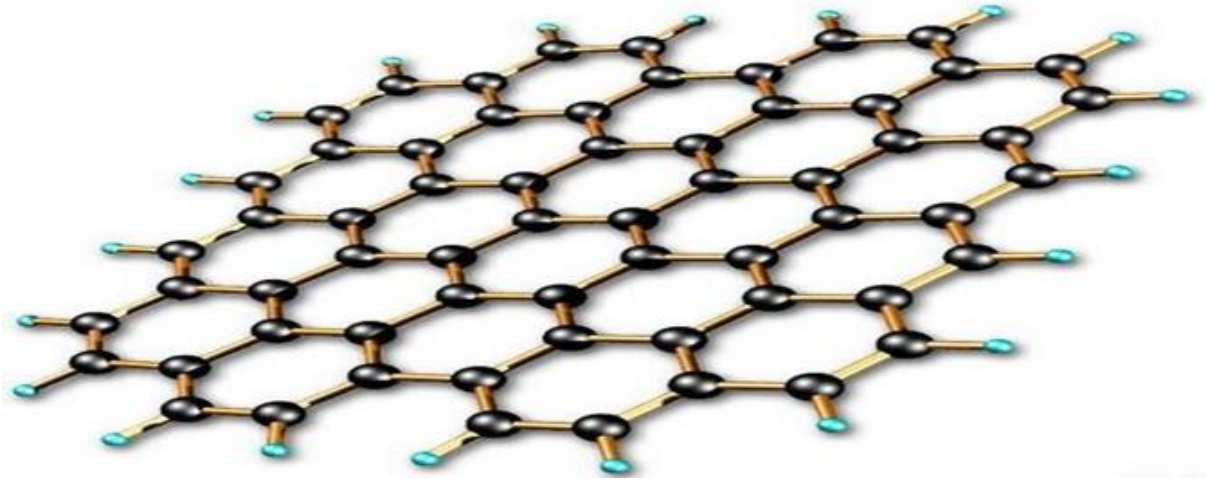

Figure 1.1: Graphene monolayer structure copied from (Ref. 299)

multifunctional composites [36, 58, 201.] Electron transported on to the graphene surface will be transported faster to the reactive oxidizing species thereby minimizing rate of recombination. Large surface area in pristine graphene will provide avenue for high degree of functionalization.

1.2 Key Properties of Graphene

High Surface Area. One of the most interesting properties graphene exhibited is a large theoretical surface area of about 2630 m^2 g^{-1}, which is twice the size of the SWCNT.[60] However, aggregation may occur between the exfoliated single sheets of graphene in the samples through π- π stacking facilitated by Van der Waals forces if the sheets are not well separated from each other by surface modification or functionalization [53, 61]. Modification or functionalization can be carried out on the basal plane and or edges [50, 51, 53, 55]. During heterogeneous catalysis, the adsorption and the catalytic degradation occur on the surface [42, 43, 44, 46, 47]. Because graphene sheet is an extended conjugated system that is 100 to 1000 times larger than the size of a typical organic molecule, therefore the surface provides an opportunity for the creation of the active sites producing a new catalytic material with enhanced characteristics [35]. Graphene has also shown good 'foldability', recovering its electrical properties after bending and unbending[150]. (Figure 1.2)

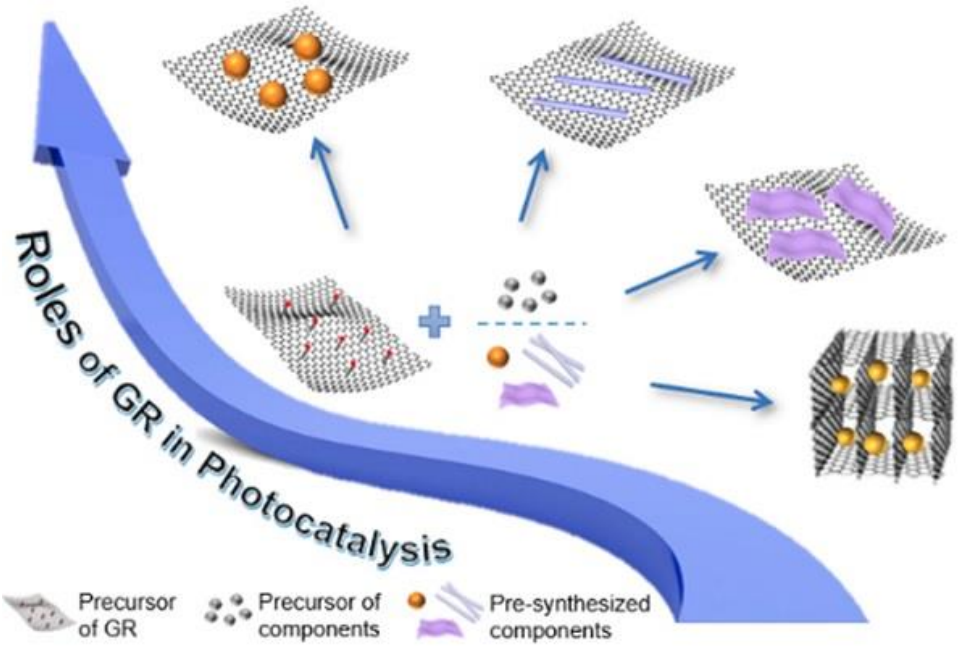

Figure 1.2: Surface area and multi-functionality of graphene-based composites photocatalyst (Ref. 300)

Intrinsic mobility and the zero-band gap. One of the unique properties of graphene, is exhibiting a zero-band gap [31, 54, 58, 59]. This was explained by the overlapping of the valence and conduction band in a single point in K space, referred as Dirac point (Brillouin zone with two non-equivalent points' k and k'). The dispersion relation of the electrons by the Dirac point (k-k') was achieved by the nearest band interaction. For this reason, graphene is referred as a zero- band gap semiconductor, and the density of states at the honeycomb lattice in direct space but rotated 90^{o}C.

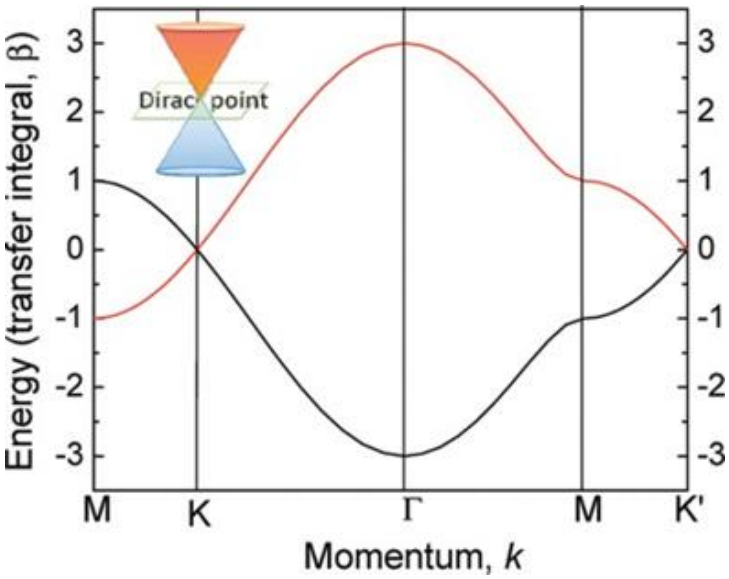

Figure 1.3: Graphene energy band dispersion in momentum space within simple tight-binding (FMO) theory; Copied from (Ref. 54).

Experimental observation of the cyclotron mass dependence on the square root of the electronic density in graphene was pointed as evidence for the existence of massless Dirac quasi particles in graphene [65, 67]. As a zero-band gap semiconductor, graphene displays an ambipolar electric field effect and charge carriers can be tuned continuously between electrons and holes in concentrations as high as 10^{13} cm^{-2}, with room temperature mobility of up to 15,000 cm^2 V^{-1} s^{-1} [64]. Similarly, minimizing the impurities in graphene suspension and controlling its room temperature, maintained the ultra-high mobility value of around 200,000 cm^2 V^{-1} s^{-1} even in high densities of both chemically and

electrically doped devices [66].

Thermal Conductivity. Graphene as 2D material, has little or no phonon scattering. The low-energy phonons in the system are involved in heat transfer, therefore providing higher thermal conductivity [31]. In general, the thermal conductivity of graphene is dominated by phonon transport, characterized as diffusive conduction at high temperature and ballistic conduction at sufficiently low temperature [59]. The thermal conductivity has proven to be very sensitive to the isotopic disorder, with percentage in the low disorder region having more than 40% reduction in thermal conductivity than isotopic disorder percentage by less than 5%; while for higher disorder percentage, the thermal conductivity keeps almost unchanged[70].

Mechanical Properties. The mechanical properties of monolayer graphene including the Young's modulus and fracture strength have been investigated by molecular dynamics [59]. In continuum mechanics, the relations between load and deformation have been developed before making a solution. Homogeneous and isotropic materials can be represented by two independent constants: Young's modulus and Poisson's ratio [69]. The Young modulus of graphene has been experimentally measured to be 1.0 Tpa ± 0.1 using atomic force microscopy (AFM) through introducing external strain on graphene and record the force displacement relation [70, 71]. If the external strain is applied on graphene, the internal force or potential can be calculated in different approaches such as interatomic potentials [71] etc. Other factors such as temperature, size of the particles, isotopic disorder can alter the value of the Young's modulus of graphene[59].

Optical Properties: Graphene has experimentally proven to be 97.7 % optically transparent in the visible range, whereby its transparency linearly decreases with increasing the layers of graphene[59]. Many of the electronic properties of graphene with its linear dispersion near the Fermi level, can be attributed in terms of massless Dirac fermions. In this view, the predicted conductivity can be viewed as an intrinsic property of two-dimensional massless fermions. This universal optical conductivity may be viewed as the high frequency counterpart of the minimal conductivity of graphene, an interesting area of investigation[72].

1.3 Synthesis of Graphene

Since after the successful isolation of graphene in 2004 by Geim and Novoselov, after several attempts in many years, graphene synthesis and its applications became a point of interest in the materials science[31, 35, 52]. However, the production of single layer graphene for commercial applications faces some challenges, especially, in the improvement of its quality, scale and size[36]. Several efforts were, and still being made to develop efficient techniques of producing best quality graphene, as well as large production[76]. (Figure 1.4)

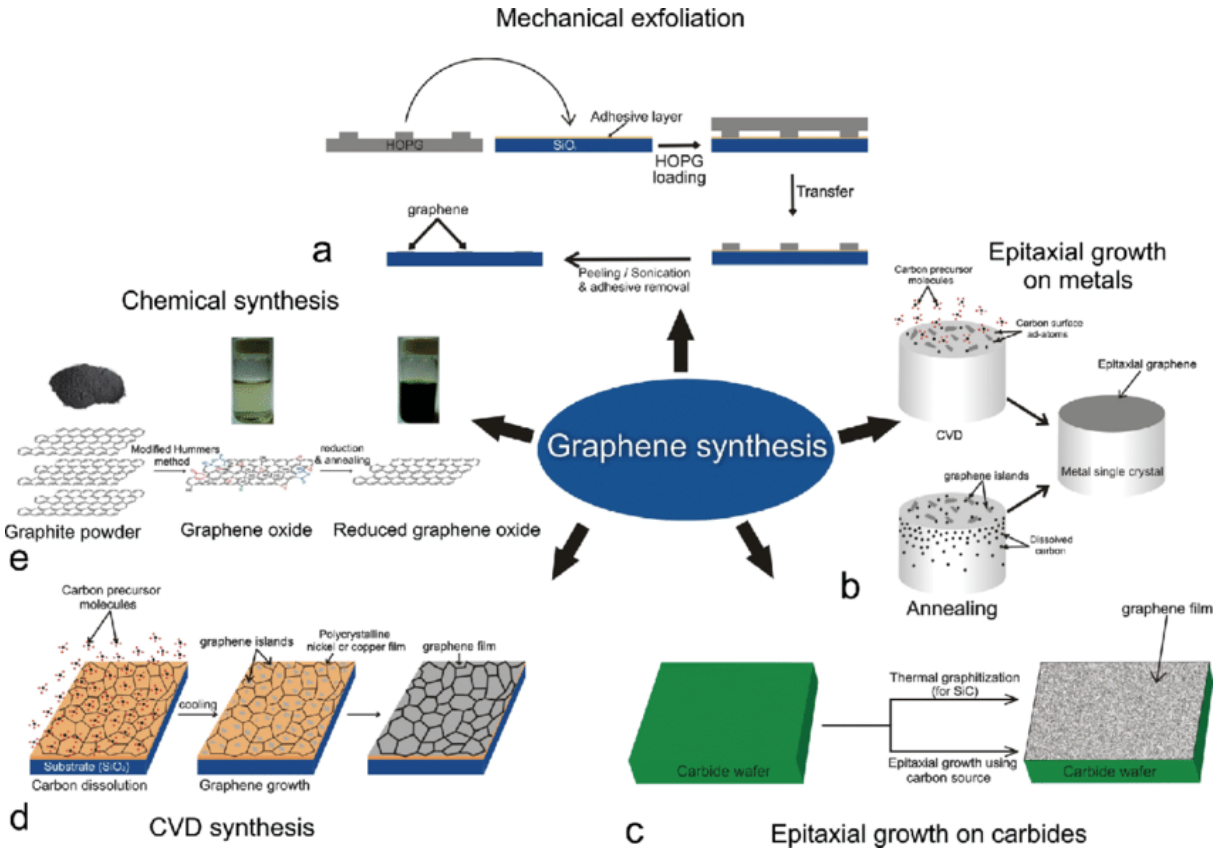

Figure 1.4: Schematic illustration of various graphene synthesis techniques. (a) Graphene flake synthesis by mechanical exfoliation form HOPG. (b) Epitaxial graphene growth on metal single crystals. (c) Epitaxial growth of graphene on carbide wafers by graphitization or deposition. (d) CVD synthesis of large area graphene on metal (Ni or Cu) foils. (e) Chemical synthesis of graphene from graphite oxide, copied from Ref (205)

Production of graphene can be carried out by two main approaches: top-down (destruction) and bottom-up (construction) methods[149]. (Figure 1.5) The top-down approach such as micromechanical cleavage, arc discharge, oxidative exfoliation-reduction, liquid-phase exfoliation (LPE), involves separating stacked layers of graphite to produce single graphene sheets, while bottom-up approach involves synthesising graphene from alternative carbon sources[150]. Top-down method involves de-stacking of the sheets, meaning that van der Waals forces that hold the layers together must be overcome, which is difficult considering the relatively low interlayer bonding energy[149, 150]. Generally, some top-down methods are highly scalable and produce high quality products.[149] But, some challenges such as effectively separating the layers without

damaging the sheets and preventing re-agglomeration of the sheets once the layers have been exfoliated[150] still exist. The setback for the top-down approaches generally includes low yields, multiple steps, dependency on finite graphene precursors and inconsistency in their properties[149, 150]. For bottom-up methods, high levels of graphitisation must be promoted to produce a good quality material, so these methods generally require high temperatures. The processes involved are usually simple, although the material produced can contain higher levels of defects than that observed for top-down methods. In addition, the bottom-up approach can utilise other carbon sources apart from graphite and atomic-sized precursors. The methods include chemical vapor deposition (CVD), epitaxial growth, total organic synthesis, template route and substrate-free gas-phase synthesis (SFGP)

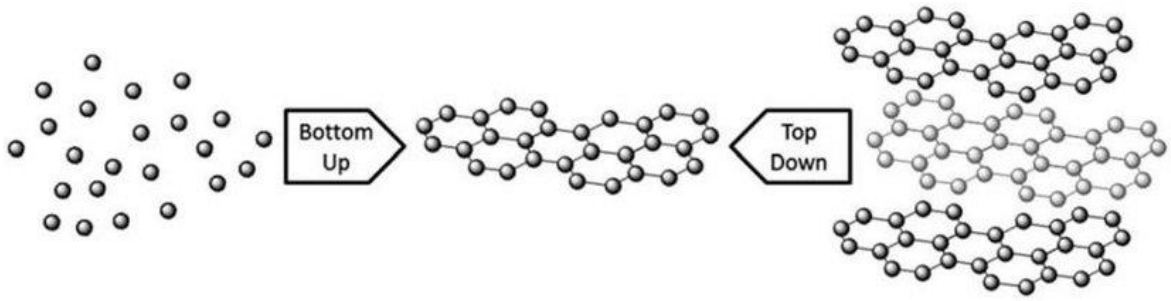

Figure 1.5: Bottom-up and Top-down approaches of graphene synthesis copied from (Ref. 155)

1.4 Bottom-up Approach

Chemical Vapour Deposition (CVD). This is the most promising method of synthesizing single-layer graphene amongst others, proven to be and capable of producing high quality products [5, 52, 77]. It can be described as the deposition of gaseous reactants onto a substrate by combination of gaseous precursors in a reaction chamber under favourable condition. (Figure 1.6) A film is formed on a substrate surface support, when gas interacts with the surface in the reaction chamber, releasing the unutilised gases. However,

throughout the deposition process the coating on the substrate is prepared in microns and at a very low speed[75]. Hydrocarbon gases such as methane (CH_4), acetylene (C_2H_2), ethylene (C_2H_4) and hexane (C_6H_{14}) and other biomass materials can be used to grow graphene sheet on metallic catalysts such as Cu and Ni films at elevated temperatures (650–1000 °C).[180-181] On landing at the hot surface of metal catalyst, the carbon precursor dissociates into free carbon and hydrogen atoms. The carbon atom then diffuses through the surface and the bulk of metal catalyst, and subsequently forms graphene sheet on the metal surface upon reaching the carbon solubility limit[149, 174-177]

Depending on the metal type, CVD graphene growth can either be surface catalysed or be achieved by segregation methods. For surface catalysed reactions the decomposition of the carbon containing species and graphene formation occur at the metal surface, and growth can be described as “self-limiting” to monolayer graphene as the surface is mollified once covered. In segregation process, graphene forms via the diffusion of carbon dissolved in the bulk metal on the metal surface, which generally occurs upon cooling due to the reduced solubility of carbon in metals at lower temperatures[149-150, 174-179]. The number of graphene layers produced by segregation depends on various factors including the amount of carbon dissolved and the rate of cooling. [150]

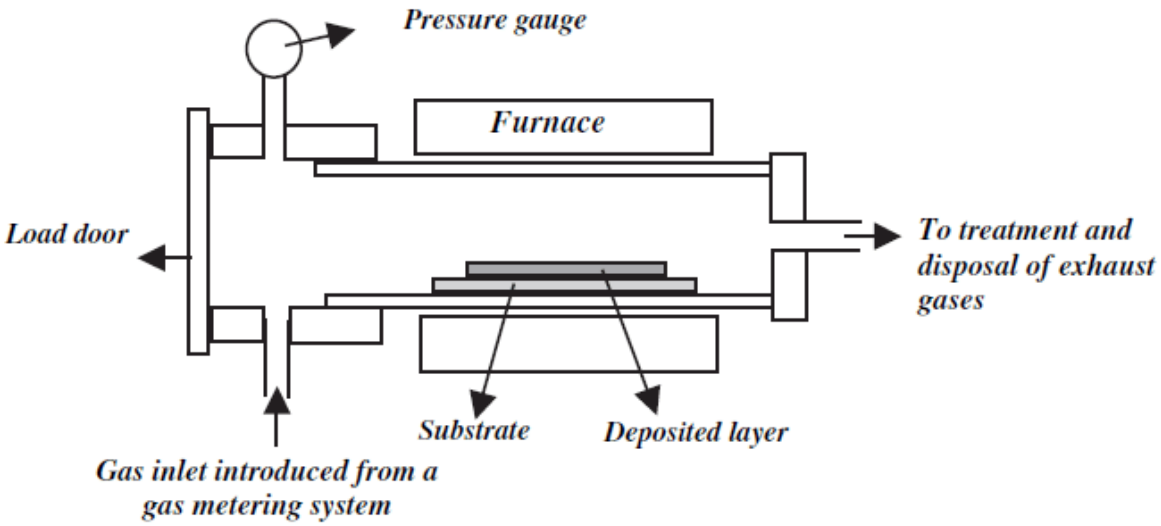

Figure 1.6: Schematic illustration of chemical vapour deposition (CVD) copied from ref. 301.

Epitaxial Growth. Graphene can also be epitaxially grown on single crystal of silicon carbide (SiC) by vacuum graphitization at high temperature[78, 149-150]. High temperature treatment causes silicon (Si) to sublimate at melting temperature of Si ca. 1100 °C, leaving excessive C atoms to aggregate and form a sp^2 hybridized network which induces graphene growth[149, 182]. Growth in argon atmospheres[183-184] or in the presence of small quantities of disilane[185-186] have shown to reduce the rate of silicon sublimation, allowing higher temperatures to be used which results in higher quality graphene. Preferential Si sublimation can also be induced by pulsed electron irradiation[187-188]. The number of epitaxial graphene layers can be controlled, and the quality of such graphene is good. However, the carrier scattering at epitaxial graphene on SiC is induced by geometry. This method prepares graphene of larger sample size, but it is costly because it requires high reaction temperature and the expensive SiC wafers. In addition, the prepared graphene is

inferior to the mechanical exfoliated graphene in quality and crystallite size[77].

1.5 Top-down Approach

Micromechanical Cleavage (Scotch tape). This method involves the exfoliation of graphite using adhesive tape to cleave the layers apart or peel-off and was the first method used to experimentally isolate graphene[150, 151]. Repeated cleavage yields mono, bi, and few-layer graphene which are identified by optical microscopy over specially prepared SiO_2(300 nm)/Si substrates, taking advantage of the change in refractive index between graphene and 300 nm thick silicon dioxide.

The sheets are of high quality because of the limited graphite processing required, but the method is slow and labour intensive, so the material produced is often reserved for study of the fundamental properties of graphene rather than use in commercial applications[150, 151]. Mechanical exfoliation can be classified based on directional routes such as normal force and shear force vectors. One of the recent studies on the normal force synthesis route is the peeling of graphite using advanced machinery of ultra-sharp single crystal diamond wedge [153]. This method is time and cost effective and replaces the need for manual operation. Shear force-based methods such as ball milling and fluid dynamic methods have been gaining much attention recently. Ball milling, which is commonly used in grinding minerals, ceramic, cement and fertilizer, utilizes balls to generate the mechanical force via impact and attrition, exfoliating graphite to form graphene flakes [149]. This technique facilitates exfoliation and fragmentation of graphite to graphene of nano-size thickness[154].

Arc Discharge. A technology to pass a direct current between high purity graphite electrodes has been widely used in the synthesis of carbon nanomaterials including

fullerenes and nanotubes[149, 150, 152]. The reaction chamber consists of an anode (carbon precursor) and a cathode (graphite rod) which are submerged either in a gas or a liquid medium. The applied electrical current dissociates the medium to generate high temperature plasma reaching up to 3727–5727 °C, sufficient to sublime the precursor. The synthesis of graphene has been investigated under different inert gas conditions which is generally expensive due to the use of vacuum equipment[149]. A few-layer graphene has been recently synthesized in different buffer gases using arc discharge. The hydrogen gas in the buffer was important for termination of the dangling carbon bonds inhibiting the rolling-up and closing of graphitic sheets.[156-162] A mixture of helium and hydrogen gas was found to produce the highest crystallinity material from a number of different buffer gases studied[150].

Oxidative-Exfoliation-Reduction. The most popular method of producing graphene is exfoliation of graphite oxide into graphene oxide (GO), followed by reduction of GO to produce graphene[149-152]. The synthesis of graphite oxide involves the use of concentrated acids and strong oxidants as done in the past by Straudenmaier [149, 165], Brodie [149, 166] methods, and Hummers methods[58, 149, 150, 164, 167, 206] which is still the most widely used method today[150]. The structure of graphene oxide has been described by a number of different models, namely the Hofmann, Ruess, Scholz-Boehm, Nakajima-Matsuo, Lerf-Klinowski and Szabo models[168-169]. The widely accepted model is the Lerf–Klinowski model[149-150, 171-172] which describes it as a layered structure with hydroxy and epoxy groups on the basal planes and carboxylic and carbonyl groups at the sheet edges. These oxygen containing groups make graphene oxide hydrophilic, and the presence of functional groups between layers also results in graphene oxide having a larger interlayer spacing (6–12 Å) depending on the amount of intercalated water) than graphite (3.4 Å) [150].

(Figure 1.7)

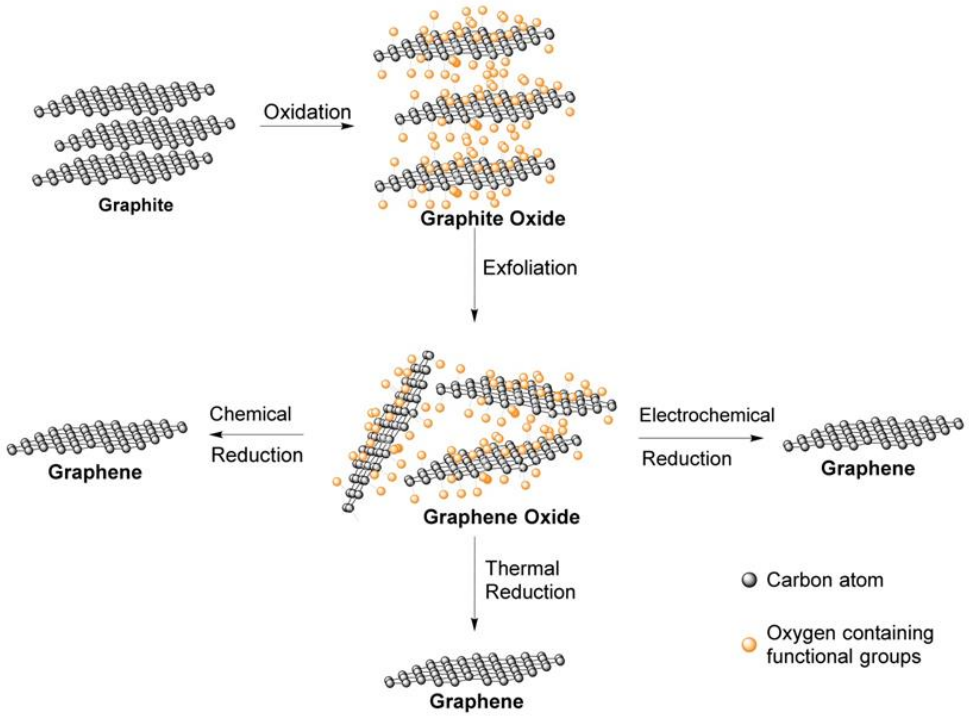

Figure 1.7: Different synthesis methods of graphene from oxidation of graphite (starting material) to epoxiliation of graphite oxide through; chemical, thermal and electrochemical reduction of graphene oxide, sourced from Ref. (206)

1.6 Reactivity of Graphene

Considering the chemical behaviour of graphene, a number of structural and electronic properties have been found useful in understanding its reactivity as a chemical substrate[54, 96]. Graphene chemistry resembles that of the fullerenes and carbon nanotubes, except their strain role in promoting addition chemistry[35, 54]. Absence of functional groups in graphene makes direct chemical modification on the basal plane impossible for normal

aromatic substitution reactions.

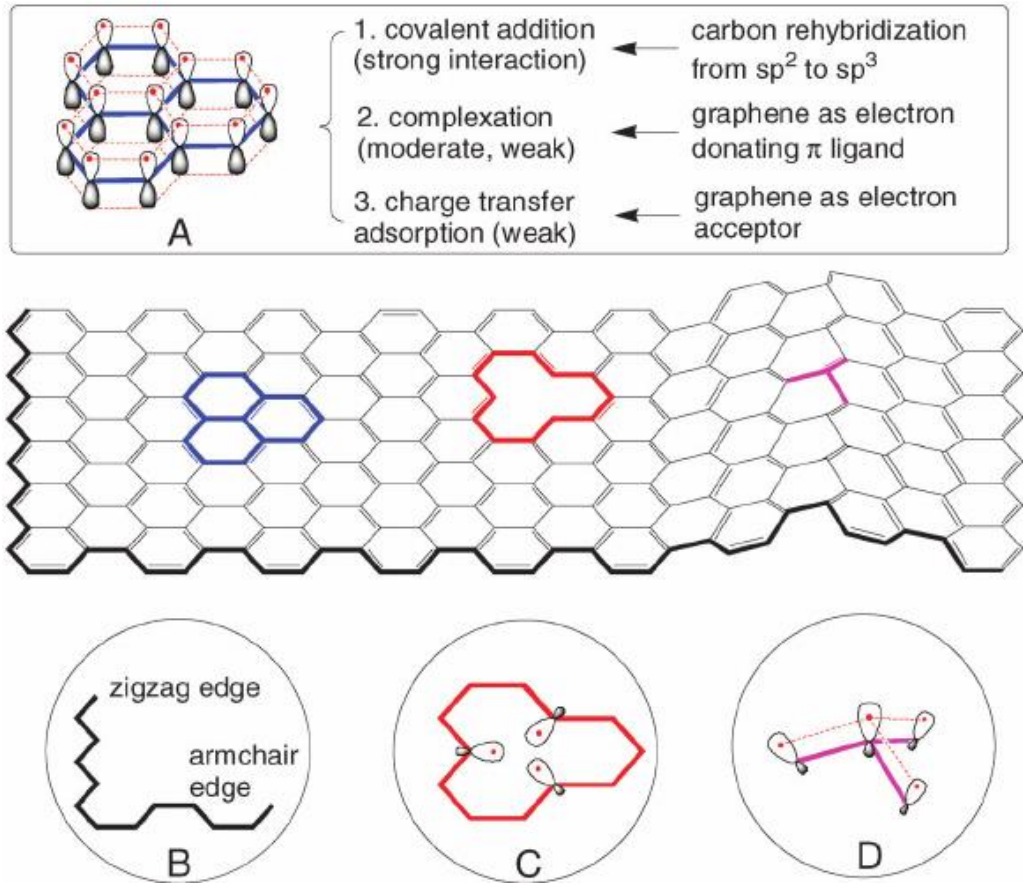

Figure 1.8: Origin of chemical reactivity of graphene. (A) Intrinsic reactivity arising from the delocalized π-bonding system. (B) Zigzag and armchair edges. (C) Monovacancy. (D) bending/curved graphene consisting of the dangling bonds, copied from Ref (208)

However, it has already been described that the atomically flat surface of graphene provides an opportunity to create sp^3-hybridized carbon centres from sp^2 carbons in the honeycomb lattice of graphene resulting from the application of aryl or alkyl molecules through carbon-carbon bond formation[54, 81, 97]. Figure 1.8 Depicts the reactivity positions of the 2D-graphene as follows; blue coloured point (A), represents the intrinsic/planer reactivity of the graphene through a covalent interaction of $–sp^2$ carbon atom in graphene and a substituent group forming sp^2-sp^3 hybridization, electrostatic π-π interaction between the graphene and aromatic ring of the substituent and also ionic interaction between the negatively charged electrons in graphene and positively charged ions of the

bonding molecules. In covalent bonding, an unpaired electron which is created at the site adjacent to the point of bonding, enhances the reactivity at that point, leading to a chain reaction from the point of initial attack and unzipping of the conjugated tracks[35]. Bold portion (B) of graphene structure in figure 1.8, represent the two different forms of graphene edges; arm chair and zig-zag tracks respectively. Due to the two-dimensional nature of graphene sheets, the edge regions play an important role in the electronic structure of the molecules[35, 54] which was further discussed in figure 1.9. Red coloured portion (C) of the structure represents the monovacancy position of graphene reactivity while the purple coloured portion (D) shows the bending/ curved position of graphene reactivity. Figure 1.10 explained reactivity of graphene from dangling bond.

Figure 1. shows the orientation of the edge along the honeycomb structure, resulting from bonds breakage between adjacent carbon atoms of the π-conjugation network. In the zig-zag edges, the realisation of aromatic sextets is frustrated in the majority of the rings, hence such a structure is thermodynamically unstable compared to the armchair edges. It can be expected that the zig-zag edges will display higher reactivity as compared to the armchair edges[35, 63, 118]. Naturally, an edge does not grow along a unique crystallographic direction and leads to more complex geometries, often with alternated zig-zag and armchair segments known as a “chiral edge”[118]. Comparable insights into the graphene reactivity can be obtained from graphene-like polyaromatic hydrocarbons where stable zig-zag edged molecules are more challenging to synthesize than the arm-chaired ones[35].

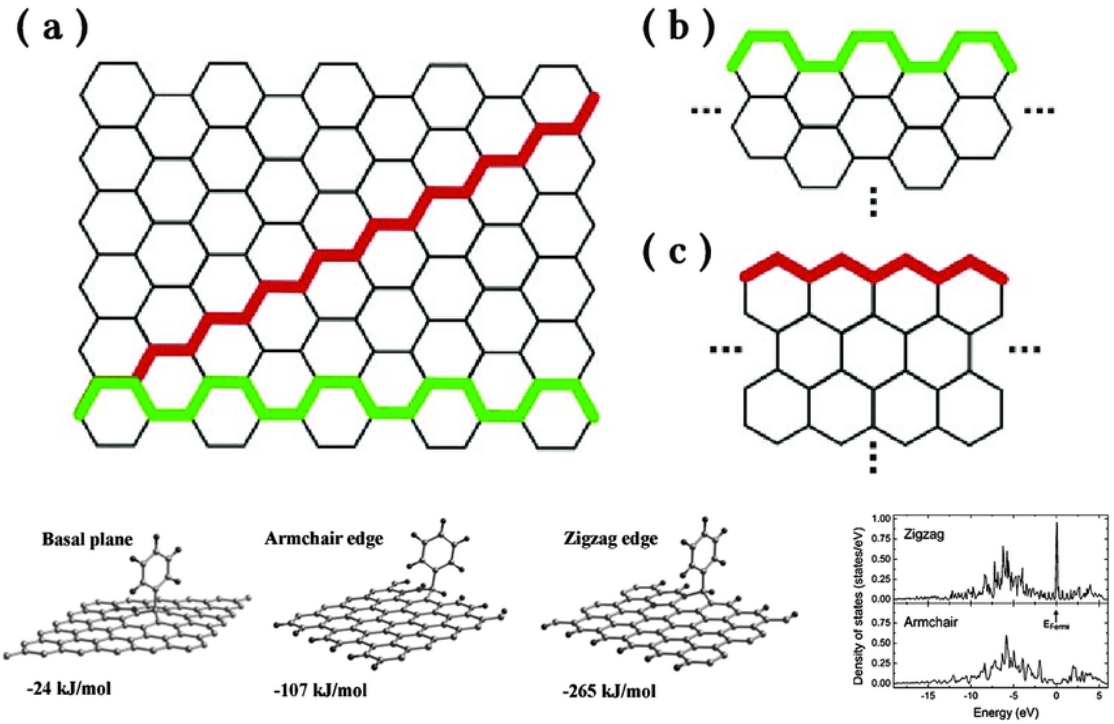

Figure 1.9: a) Illustration of graphene edges b) armchair track and c) zig-zag track and their respective reactivity strength below copied from (Ref. 296) and (Ref. 297) respectively.

Dangling bonds (Figure 1.10) can develop during the edge formation, and are the most reactive sites[54, 96, 118] within basal plane. Thus, the energetically favourable processes involve the chemisorption of functional groups in different sub-lattices, rather than on the same sub-lattice[35, 54], which can lead to a geometric strain.

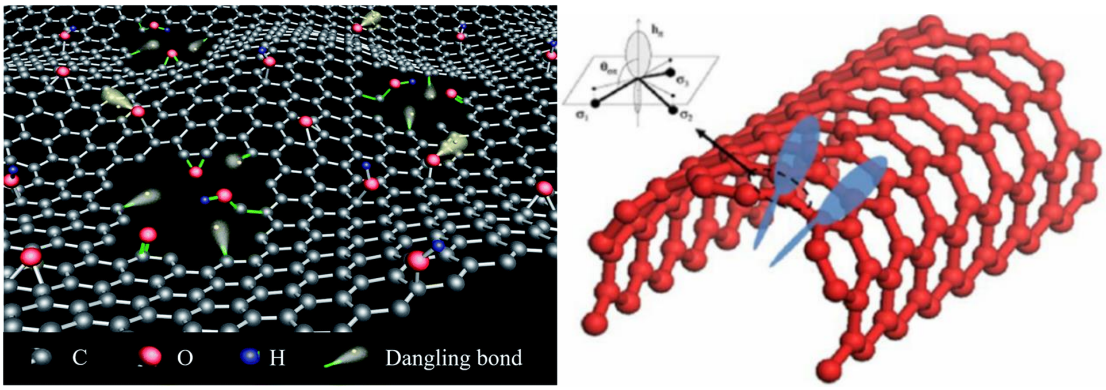

Figure 1.10: (left) Structures of HGO containing the dangling bonds copied from Ref (202). (right) Schematic illustration bending in graphene (strain) copied from Ref. (203)

Moreover, the principle of minimization of geometric strain may direct the reactivity to attain relaxation of the strained areas and flow through re-hybridization[17, 35, 54]. Strain engineering on the surface lattice of graphene in a periodic manner can control the reactivity and degree of functionalization of graphene.

1.7 Functionalisation of Carbon Materials by Electron Transfer Chemistry

Despite the unique properties of graphene and its potential applications, it is important to note that the inertness of graphene to chemical reaction and its zero-band gap, limits the potential of graphene in many fields including, but not limited to, semiconductors, sensors, catalysis[55, 98]. For this purpose, and by virtue of its great advantage of large surface area, the limitation in graphene can be addressed by chemical modification or functionalisation with organic and inorganic materials through covalent and non-covalent interaction[53-58]. (Figure 1.1). Covalent functionalization of graphene can be achieved in two routes; i. free-radical and dienophile functionalization of pristine graphene, and ii. Covalent functionalization of GO with organic functional groups. While the non-covalent functionalization can be achieved through π- π interaction, ionic interaction, π-Ligand interaction etc.

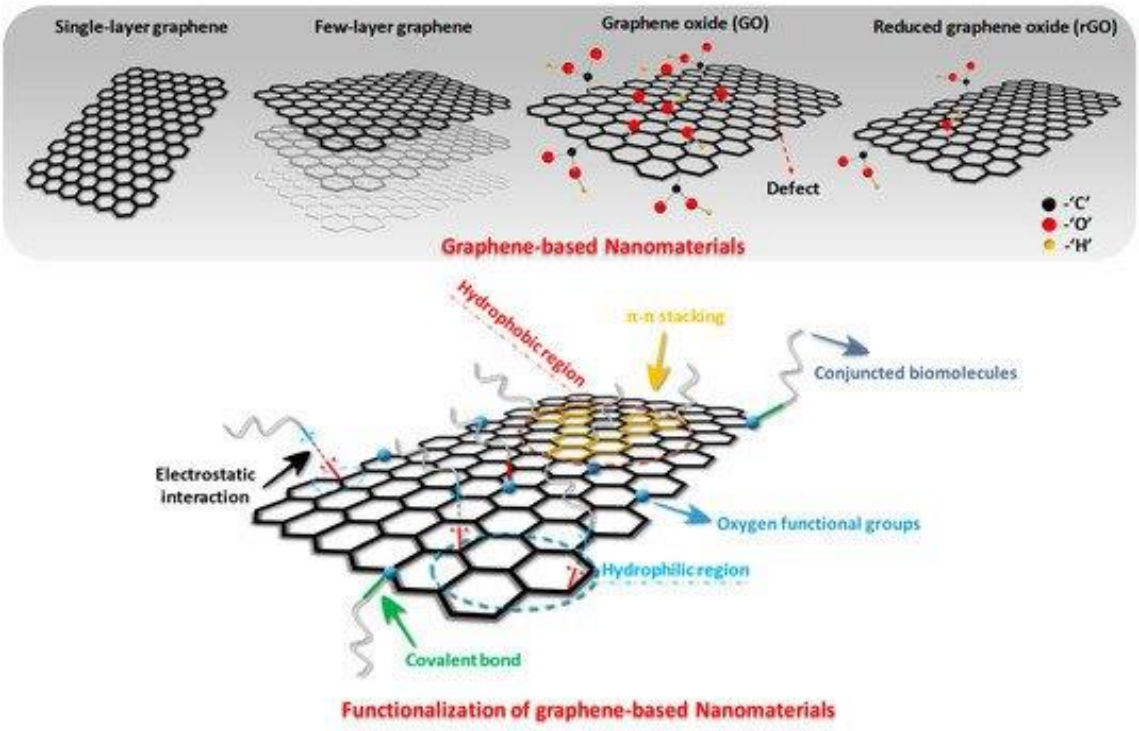

Figure 1.11: Overview of the various structures of graphene-based nanomaterials (GNs) and the illustration of their covalent and non-covalent functionalisation, copied from Ref. (207)

Functionalisation of pristine graphene sheets with organic functional groups has been developed for different purposes, the major being to improve dispersibility of graphene in common organic solvents[55] as it has a limited solubility in most organic solvents other than strong ones such as N-methyl pyrrolidone and 1,2-dichlorobenzene[53]. Functionalisation of graphene by either physisorption of surfactants or polymers, or chemisorption (chemical modification) with organic molecules improves solubility/ dispersibility of graphene in many solvents including water [68]. This is due to hybridization of sp^2 (C=C) to sp^3 (C-C) in covalent bonding, and the Individual graphene sheets can easily aggregate due to the van der Waals forces inducing the π-π stacking interactions between graphene layers[73] in non-covalent interaction. Functionalisation of graphene provides stabilisation in their composite by lowering the surface energy of the material [68, 74].

Previous studies on electron transfer chemistry proved to be successful on various

materials such as conductors e.g. stainless steel[141], semiconductors[142-143] e.g. TiO_2, MOS_2, ZnO and nanomaterials[136-140,144] e.g. nanotubes, fullerenes, nanohorns when utilising aryl diazonium salts in photochemical, thermal, and electrochemical methods. Raman and UV–Vis–NIR spectroscopies have been used to study the functionalisation products derived from aryl diazonium precursors reacting with SWNTs[140]. Another method utilizing arenediazonium salts in a solvent-free and aqueous-based media used GC–MS thermolysis and XPS analysis to confirm the arene group as the only functionality on single wall carbon nanotubes. The mechanism revealed a direct aryl radical addition to the SWNT or electron injection from the nanotube to the arene diazonium species, reaction of the SWNT-radical cation with an aryl radical, followed by an electron transfer to the nanotube[137]. A sophisticated tool of electrochemical functionalization of CNT in a selective and controlled manner has been developed[136]. This originated from the superior electrocatalytic properties of the CNTs and their high surface-to-volume ratio, as compared to other carbon materials[139]. A constant potential or a constant current is applied to a CNT electrode immersed in a solution containing a suitable reagent. A highly reactive radical molecule is generated through electron transfer between the CNT and the reagent. Organic radical species may have the tendency to self-polymerize, leading to a covalent or non-covalent layer of polymer on the sidewalls of the tubes, or even react with the starting reagent[136]. These examples demonstrate a great potential of electron transfer chemistry and its adaptation to graphene modification, because CNT was derived from graphene (roll-up graphene), hence are both allotropes of carbon in 1 and 2 dimensional structures.

1.8 Covalent Functionalisation of the Graphitic Surface

The primary purpose for the functionalisation of pristine graphene is to achieve dispersion

in many common organic solvents, by tuning its solubility, making it a suitable system for composites formation[35, 55]. Covalent functionalisation of pristine graphene typically requires reactive species that can form covalent adducts with the sp^2 carbon structures in graphene[53]. Functionalisation can occur on the surface, at the edges and at the defect sites[99]. (Figure 1.12)

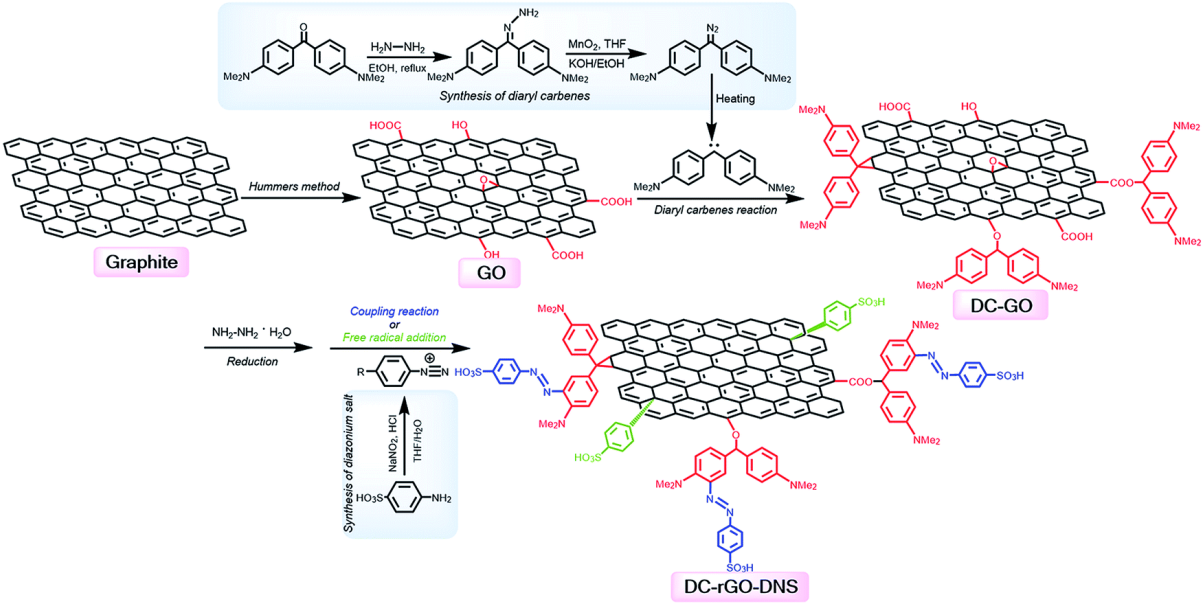

Figure 1.12: Illustration of covalent radical modification of graphene by diazo chemistry copied from (Ref. 298).

Covalent functionalisation of graphene affects its extended aromatic structure from sp^2 to sp^3 thereby changing the properties of the graphene e.g., tuneability in electrical conductivity, optical and photovoltaic properties[53, 55]. Covalent functionalisation reactions of graphene involve two important approaches: Very reactive species such as free radicals and dienophiles interaction with C=C bonds of pristine graphene and the formation of covalent bond of organic functional groups via addition and condensation reactions, nucleophilic and electrophilic substitutions.[68, 99, 116-120]

Radical covalent functionalisation can be initiated through benzoyls peroxides[53], styrenes[53], however the most common method is using diazonium salt[56, 110]. Theoretical

study of the electronic and magnetic properties of the radically functionalised graphene at single carbon centres has shown a possibility of generating a band gap and under certain conditions may lead to ferro- (ferri-) magnetism[81]. Apart from diazonium chemistry reaction, dienophiles also react with sp^2 carbons of graphene[53]. One of the most common dienophiles successfully applied in the functionalisation of carbon nanostructures e.g. fullerenes, nanotubes, nanohorns etc, is azomethine ylide employed in 1,3-dipolar cycloaddition. (Figure 1.13)

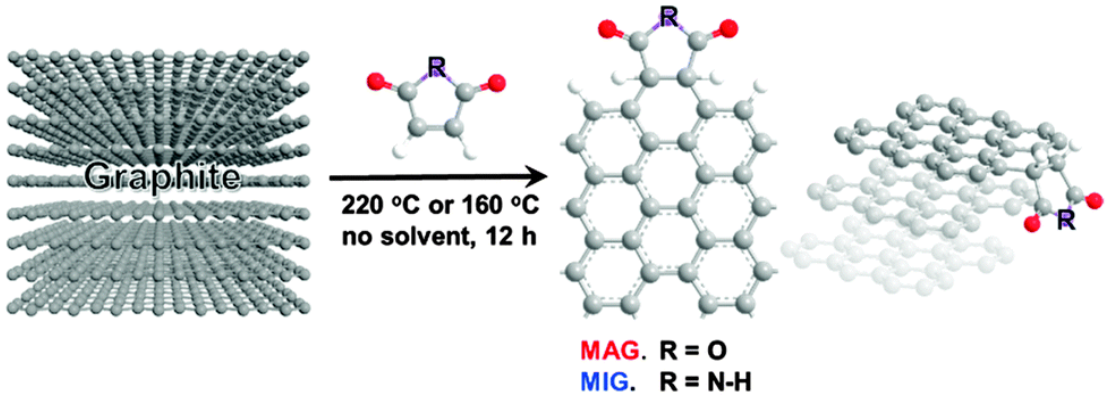

Figure 1.13: Diels-Alder addition to graphite copied from Ref (210)

Nitrene chemistry became a useful technique for the chemical modification of carbon nanotubes and fullerenes[121-124] and consequently was successfully adapted to graphene[53, 121, 125-129]. When light or heat is applied, the azide functionality dissociates into molecular nitrogen and a highly reactive singlet nitrene species[125-129]. The potential of singlet nitrene, especially the aromatic ones such as phenyl nitrene, has been explored over a long period of time[130-135]. Diazirines are three-membered heterocyclic rings that have a sp^3 carbon atom bonded to an azo group. Similar to azides, diazirines decompose upon heating or irradiation to release molecular nitrogen and give the electron-deficient carbene species. The highly reactive carbene is capable of undergoing insertion reaction to C-H bonds and [1+2] cycloaddition reaction to C=C bonds in high yield, if there is no competing reaction pathways[53]. Cycloaddition, CH insertion and click reaction exhibit regioselective reactions

based on zig-zag, armchair conjugated tracks on the graphene plane. However, the detailed reactivity of graphene in terms of possibility of stoichiometric control, size and shape are still under study[35].

Other form of covalent modification of graphene involves the reactions of the oxygenated groups on the graphene edges. However, the abundance of these functionalities is rather low. This can be rectified by oxidizing graphite into graphene oxide (GO) by Hammer method. (Figure 1.14)

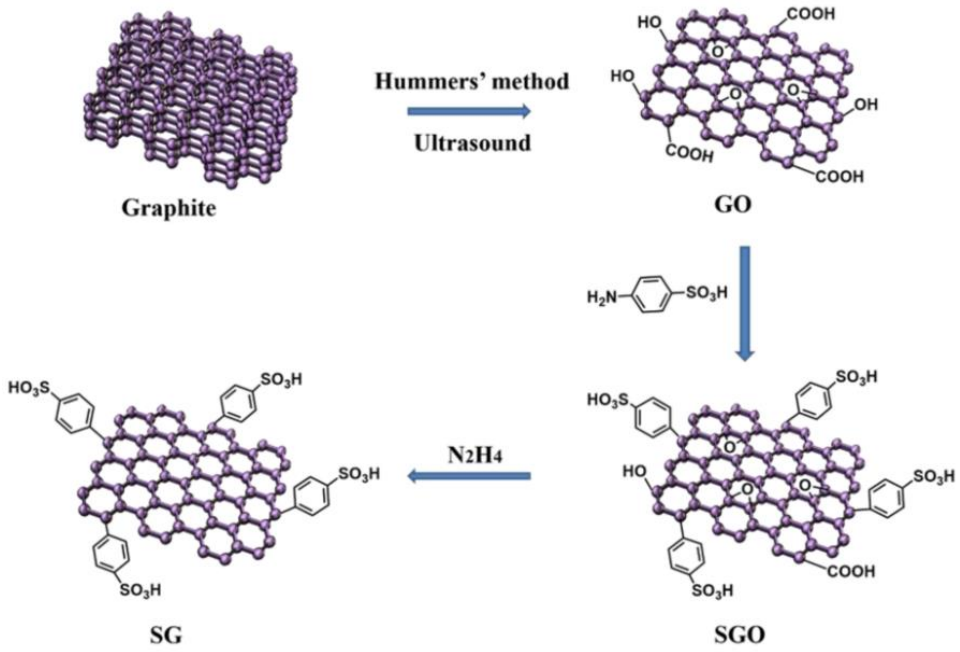

Figure 1.14: Covalent functionalisation of graphite and GO by Hummer's method, copied from Ref. (211)

GO can be characterised as a single graphitic monolayer with randomly distributed aromatic regions, sp^2 carbon atoms, the sp^3 carbon atoms and oxygenated aliphatic regions. The presence of oxygen groups on the surface of GO provides a remarkable hydrophilic character and a similar chemical activity[55]. (Figure 1.14) GO contains many such groups e.g. carboxylic at the edge, and epoxy, hydroxyl, along with C=C groups in the basal plane.[115, 126] Carboxylic acid functional groups of GO which mainly found at the edges, can form a covalent bond with amines, alcohols and phenols to form amides and

esters respectively. Hydoryl groups on the core plane of GO can form silanization[145-146] and etherification[147] reactions respectively with silane and hydroxy group. While the epoxy groups on the basal plane can be functionalised with amine-terminated molecules or sodium azide through a nucleophilic ring-opening reaction. The opening of the epoxy ring is mainly performed with amino moieties. The major setback in GO is the presence of oxygenated groups on graphene which makes π-conjugation difficult, and therefore GO becomes an insulator[35]. Another set-back is the risk of secondary and mild reaction because of its instability[56]. GO is non-stoichiometric in nature due to a random distribution of oxygenated groups from the oxidation process; this leads to imbalance in the GO density resulting in a non-stoichiometric functionalisation of GO.

1.9 Introduction to Polymers

The term polymer refers to substances forming building blocks from many repetitive units called monomers usually connected by covalent bonds. The prefixes ‘poly’ and ‘mono’ are Greek words referred to ‘many’ and ‘one’ or ‘single’ respectively, while the suffix ‘meros’ shortened as ‘mer’, means ‘parts’ or ‘units’. Polymer can be a naturally occurring or a synthetic with linear, branched, or crosslinking geometry. In the synthesis of many polymers monomers are linked together in the same manner to form a single chain consisting of covalently connected repeating units[246, 247, 249]. Among various branches of chemistry polymer science is relatively new and multidimensional area, and its classification was originally done in 1929 by Carothers into addition and condensation polymers based on the compositional difference between the polymer and the monomer(s) originated[249]. Condensation polymers are types of polymers that were formed from at least a bifunctional[248] or polyfunctional monomers by the various condensation reactions using organic chemistry with the elimination of some small molecule such as water[249]. Different

applications of natural polymers have been identified and documented since immemorial time[246].

Early proof of the existence of large organic molecules was provided by Roult's (1882) and Vant's Hoff (1887), they carried out a cryoscopic molecular weight determinations on rubber, starch, and cellulose nitrate. Through the formulation of solution laws, and their methods, a molecular weight of 10,000 to 40,000 were demonstrated[247]. However, this great discovery received a major setback by the scientists of that time, for the fact that the work was unable to differentiate macromolecules from colloidal substances that could be obtained in low molecular weight. In the end of 18th and beginning of 19th centuries, the idea of molecular complexes was generally accepted and was used to explain polymer structures in terms of physical aggregates of small organic molecules[246, 247]. Only the pioneering work of the late Hermann Staudinger (1926), a Nobel laureate, in the 1920s provided the basis for a systematic understanding of this class of materials[246, 247, 248]. In the decades since then, polymer science has developed to become both technically demanding and industrially extremely important. Because of its technologically relevant macromolecules based on a carbon backbone, macromolecules used in classical materials, great applications in medical technologies, highly specialised applications, such as artificial heart valves, eye lenses, or materials for medical devices and many other important applications including crucial biological areas. Polymers are considered an interdisciplinary in nature[246, 248]. Without a doubt, the most important polymer in the world, without which human existence would have been impossible, is the DNA[246].

1.10 Naturally Occurring Polymers

There are many naturally occurring polymeric materials of which many are complex and has been randomly classified and divided into six main categories [247]:

i. Polysaccharides, e.g., starch, cellulose, chitin, pectin, natural gums etc.

ii. Proteins or naturally occurring polyamides found in animal and vegetable sources.

iii. Polynucleotides include all the deoxyribonucleic acid (DNAs) and all the ribonucleic acids (RNAs) found in all living organisms.

iv. Polyisoprenes or natural rubbers and similar materials that are isolated from saps of plants.

v. Lignin or polymeric materials of coniferyl alcohol and related substances.

vi. Naturally occurring miscellaneous polymers e.g., shellac, a resin secreted by the Lac insect.

1.10.1 Chitin

Chitin is a nitrogen containing polysaccharide, which can be deacetylated to yield an amine group bearing polysaccharide[247, 250, 251]. It resembles cellulose except that the OH at C–2 atom is replaced by an acetamido group (CH_3CONH)[250, 252] (figure 2.1). Chitin is the main component of the hard external covering (exoskeleton) of crustaceans such as lobsters, crabs, and shrimp [247,249]. Like cellulose, the processing of chitin into polymeric products is limited by its insolubility (due to hydrophorbic property of acetyl group) and decomposition without melting. The availability in huge quantities has encouraged many attempts to find commercial applications of chitin, but very few have been found to be economically feasible[249].

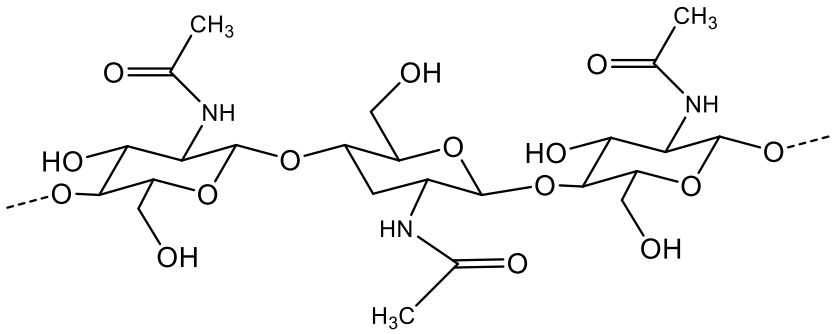

Scheme 1.1: *Structure of Chitin*

1.10.2 Chitosan

Chitosan is a linear polymer of α (1-4) linked 2-amino-2-deoxy-β-D-glucopyranose, derived from partial deacetylation of chitin[250-252]. It is the second most abundant polysaccharide after cellulose, extracted from crustaceans, insects and certain fungi[250, 251]. Ordinarily, chitosan is insoluble in water or organic solvents, but in acidic pH, when the free amino groups are protonated, chitosan becomes a soluble cationic polymer with high-charge density[250]. Owing to its many attractive properties; hydrophobicity, biocompatibility, biodegradability, non-toxicity and the presence of functionality, a very reactive amino ($–NH_2$), secondary and primary hydroxyl (–OH) groups in its backbone, makes chitosan an effective adsorbent material for the removal of wastewater pollutants[251]. Other applications of chitosan include food and cosmetics industry as well as the biomedical field in relation to tissue engineering, and the pharmaceutical industry associated to drug delivery[250].

The main advantage of chitosan over other polysaccharides (cellulose or starch) is their chemical structure that allows specific modifications to design the polymer for selected applications[251]. In addition, chitosan can be grafted with other molecules through covalent bonding. The amino groups can be used for acetylation, quaternization, reactions with aldehydes and ketones, chelation of metals etc. The hydroxyl groups can lead to *o*-acetylation, H-bonding with polar atoms etc. Primary derivatization followed by grafting

improves the solubility, antibacterial, antioxidant, chelating, complexing, bacteriostatic and adsorbing properties while maintaining its mucoadhesive, biodegradability and biocompatibility. Functionalities can also be used for interaction of chitosan with ions[250].

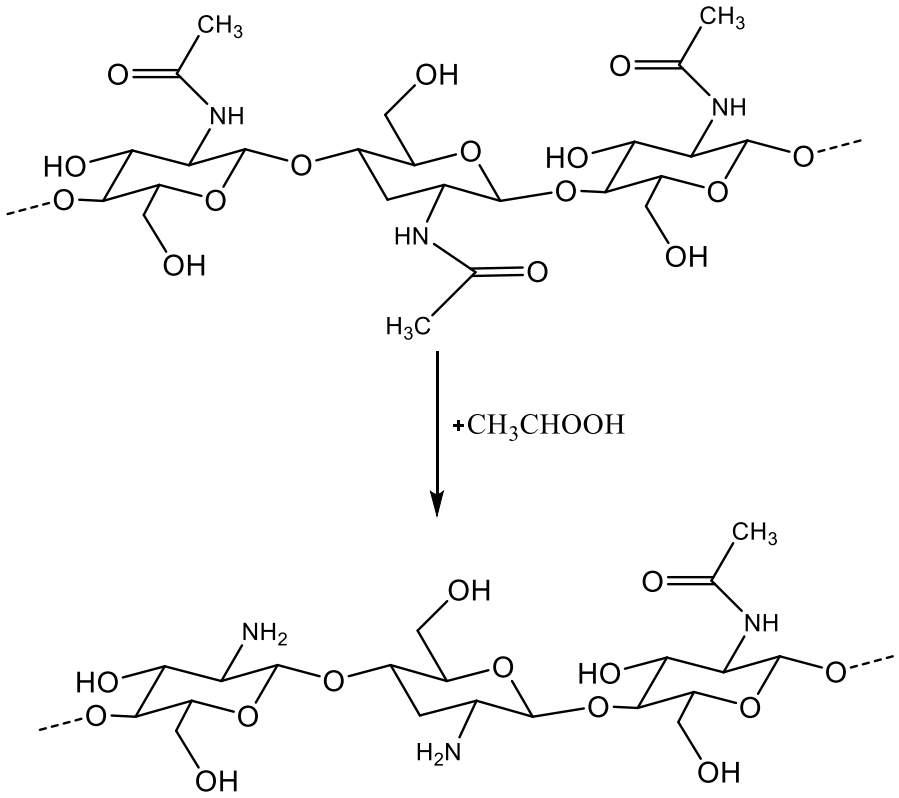

Scheme1.2: *Production of Chitosan from Chitin*

1.11 Justification for Research

Unfortunately, materials with a large band gap e.g TiO_2 require a limited source of energy (UV) to be activated. [2] Nanomaterials may have zero or little band gaps e.g, graphene [31, 54, 58, 59], graphene oxide (GO), reduced GO (RGO). [1, 84] By virtue of its, large surface area, graphene has great advantage in the construction of catalysts.

Covalent functionalisation of graphene surface with diazonium salt (strong electrophile) via electron transfer, is the most common and promising routes to modify pristine graphene surface, especially the basal plane which has very poor reactivity (inert). Organic dye

(chromophores) modification of graphene and other carbon nanomaterials is one of the new strategies of extending light absorption zone of the photocatalysts and enhancing their activity.

Incorporation of light harvesting molecules on semiconductor photocatalysts becomes an alternative approach to extend photon absorption in the region of visible light for photocatalysis[6]. However, the challenges are to develop a system with a good stability, intensive visible light harvesting capability and efficient photocatalytic activity. To achieve these goals, certain parameters must be accounted for such as nature of the reactants (dye), type of light to apply, and the type of linkage between the photosensitisers and the nanoparticles.

In this system, an electron will be excited through absorbing light of UV or visible region of the solar spectrum by the covalently bonded molecule on the semiconductor surface. A high-energy electron (photon) will generate from the valence band (HOMO) of the dye, creating a hole (h^+), and get excited to the conduction band (LUMO) of a dye. The photon is quickly transferred on to the graphene surface (a good electron acceptor and transporter)[3, 25, 30, 106, 107], and then scavenged by reactive oxygen species (ROS) on the surface. This action prevents electron recombination, and the dye hole reacts with other species in the reaction mixture. Details of this will be discussed under chapter 4.

1.12 Aim and Objectives

This work aimed to develop series of methodologies to modify graphene surface with a range of organic molecules (light harvesting chromophores) through covalent radical functionalisation in two different methods; 2-step and in-situ methods, called methods A and B respectively.. To improve adsorption capabilities of the catalysts and produce a multi-functional composites, covalent and non-covalent modification of graphene with

polymer (chitosan) were developed. Characterization of the modified materials through range range of techniques, such as UV-vis absorption, SEM, TEM, BET, FTIR, PXRD and TGA was necessary to confirm the success of the fabrication and to understand the nature of the bonding between graphene and organic entity.

The validation of composites as potential materials for pollutant removal can be tested by assessing their (photo)activity and adsorption ability. This can be tested through removal of three known hazardous dyes such methylene blue (MB), rhodamine B (RhB) and methyl orange (MO) using UV-vis spectrophotometry. Desorption experiments to separate degradation from physisorption processes during the dye removal are also can be studied.

Objectives of the project were:

- To synthesise diazonium salts of six different organic chromophores; Aminochromone, Aminoacridine, Aminoanthraquinone, Aminophenazine, Aminoflouresceneimine and Aminothionine, to modify the surface of graphene;
- To develop a *one-pot* procedure, which can be utilized unstable diazonium salts;
- To improve adsorption and dispersion capabilities of graphene by employing chitosan using covalent and non-covalent approaches and to modify graphene with chitosan and organic molecules (three-component system);
- To characterise the modified materials by spectroscopic and microscopic techniques such as UV-Vis and fluorescence spectroscopy, FTIR, PXRD, BET, SEM, TEM, and TGA;
- To test the efficiency of the synthesized materials to remove organic pollutants employing UV-vis spectrophotometry.

Chapter two

Covalent radical modification of graphitic surface with organic chromophores

2.1 Abstract

Modification of graphene with different light harvesting chromophores; 7-Amino-2-methylchromone, 9-Aminoacridine, 1-Amino-4-hydroxyanthraquinone, 3-Amino-7-dimethylamino-2-methylphenazine hydrochoride, 6-Aminoflourescein and 3-7-diaminophenothiazin-5-ium chloride have been successful. Modification of Gr-phenazine was used as templete using two different synthetic methods; *2-steps and one-pot*. However, the one-pot method (method B) was adopted for the fabrication of all other composites which involve several steps: i) *in-situ* generation of diazonium salts of a range of organic dyes, ii) the photoactivation and release of active radicals, and ii) the modification of the graphitic surfaces through electron transfer chemistry. The success of this functionalisation was probed by a variety of spectroscopic and microscopic techniques including FTIR, PXRD, BET, SEM, TEM, TGA, UV-Vis absorption and fluorescence spectroscopy.

2.2 **Introduction**

Environmental pollution with organic compounds, known as emerging contaminants, is one of leading causes for concern as conventional water treatment plants do not remove these contaminants efficiently.[274] Adsorption remains a promising process to remove these pollutants since it provides low initial costs, a simple design and a choice of adsorbents.[274, 275] Moreover, the emergence of multi-functional carbonaceous materials (adsorption and catalytic oxidation) such as biochar,[276, 277] reduced graphene oxide,[278]

carbon nanotubes,[279] g-C_3N_4[280] proved to be potential alternatives.[275, 281] Their ability to remove pollutants through (non-) radical pathways[276] is driven by the availability of reactive groups. Graphene is well suited to remove emerging contaminants, which are present at low concentrations and generate a hazard to the environment.[282] Graphene also has distinct advantages over composites of transition metals because it is relatively inexpensive, environmentally friendly, non-toxic and produces no secondary pollution.[283] However, it is highly hydrophobic and has a tendency to aggregate. Moreover, a lack of functionalities limits graphene's adsorption capability to π-π interactions, and irreversible trapping of pollutants is difficult to achieve. Although graphene-based materials have emerged as highly promising candidates for a variety of applications[284] including strong potential in processes such as photoreduction of CO_2,[285] Fischer-Tropsch synthesis,[286] water splitting,[287] and water treatment[288], the materials involved in these transformations normally contain metal-based active centres,[289] whereby graphene plays a role of support. This is partially due to pristine graphene having a low density of (electronic) states (DOS) near the Fermi level, and therefore, the activity is driven by the intrinsic characteristics of the non-graphene component of the system.[290] Consequently, in order to create truly metal-free systems based on graphene manipulation of electronic properties through the tuning of its band structure[291] is required. This can be achieved by the functionalisation of graphene basal plane *via* chemisorption, physisorption or doping with heteroatoms.[21, 56, 282, 292, 293] These approaches can be used to create defects and active sites on the graphene surface,[282, 293] and significantly expanding its potential as a catalyst. Moreover, its dispersibility in common organic solvents and water can also be improved through a lowering of the surface energy[282]. Covalent functionalisation is a more suitable pathway to fabricate materials for environmental remediation, because it leads to more prominent changes in the electronic properties due to the disruption of the crystal

lattice[17], this in turn helps to create active sites for catalysis and efficient adsorption. Thus, significant efforts aimed at covalent functionalisation of the graphene surface in order to tune the band gap and modulate its doping level have been undertaken.[294] Due to the inert nature of the sp^2-hybridised lattice of the pristine graphene basal plane, covalent modification involves reaction with reactive radicals or dienophiles.[293, 295] Our group have previously reported a two-step photochemical method using radical grafting induced by white light to produce a graphene-phenazine hybrid with improved solubility and a modified band gap.[20] The report, was for the first time, a general photochemical methodology that can be applied to a wide range of structurally different molecules to fabricate a diverse family of graphene-chromophore systems in an easy and cost-effective manner. It has also evaluated their ability as new materials for dye removal using a combined adsorption and photocatalytic strategy.

2.3 Diazonium Chemistry in Graphitic Surface Modification

Diazonium chemistry is the most common method used to covalently functionalise conducting and semiconducting materials[53]. It is a wet chemistry technique employed to modify a variety of surfaces, including polymers[48] and carbon materials[47]. Diazonium compounds e.g. diazonium salts are a group of organic molecules sharing a common functional group $R\text{-}N{\equiv}N^+ X^-$ where R can be any organic residue such as alkyl or aryl organic moieties, while X^- is an inorganic or organic counter-anion. The process of forming diazonium compounds is called ‘‘diazotization’’[51]. The reaction was first reported by Griess in 1858, who subsequently discovered several reactions of this new class of compounds[51]. One of the most popular approaches for the generation of aryl radicals involves the spontaneous reduction of the corresponding diazonium salts. However, a major drawback of diazonium chemistry is the limited covalent grafting density in combination with

multilayer formation or dendritic growth.[110] Due to the absence of functional groups on the planar surface of the graphene nanosheets, a more sophisticated method of functionalizing the surface with the electron transfer chemistry has been considered. Covalent functionalisation of the graphene using diazonium chemistry proved to be successful with a high yield.[17] (Figure 2.1)

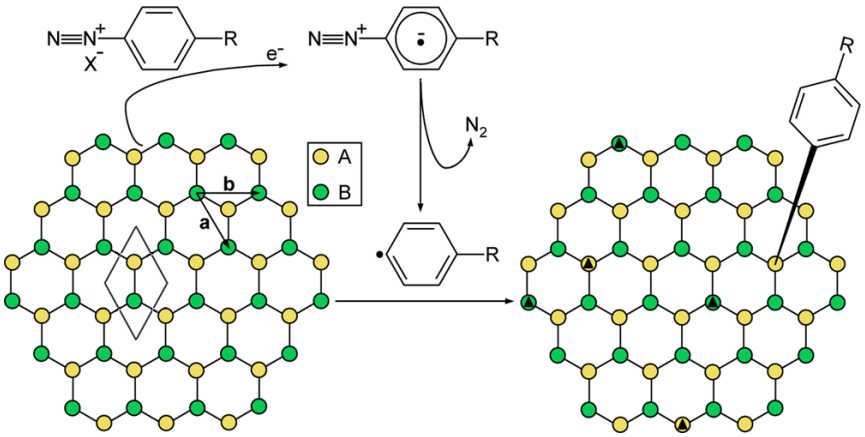

Figure 2.1: Schematic representation of Photo-induced surface functionalisation via electron transfer copied from Ref (19)

Significant effort was focused on covalently functionalising graphene to achieve band gap tuning and modulation of its doping level for various optoelectronic and sensing applications and for interfacing graphene with other materials. Covalent functionalisation is more robust than non-covalent (weak and fragile) one and changes the electronic properties more strongly due to the disruption of the graphene's crystal lattice[18]. The stability of the extended delocalized π-system ensures that the basal plane of graphene is fairly chemically stable[19]. The atomically flat surface of graphene creates a chance to form carbon-carbon bond, forming chemical reactions to facilitate the electronic mobility of graphene. Covalent functionalisation of the basal plane or the edge of graphene ribbons provides a novel design that can control the energy band gap, affect electron scattering, and direct current flow by producing dielectric regions in a graphene wafer [73].

Pinson and co-workers described in their pioneering paper on aryl diazonium salt, the

reaction mechanism for the modification of carbon electrodes.[111] This opens door of further investigation, fundamentals and applied aspects of the surface chemistry of aryl diazonium salts.[112]. Aryl radical covalent addition on graphene was first reported by Tour and co-workers[55, 99] with several techniques for aryl radical generation reported. However, the diazonium salts reduction gives the simplest route for the functionalisation, large choice of reactive functional groups, high reactivity and strong aryl–surface covalent bonding [19, 53-54, 82-83]. (

Figure 2.2)

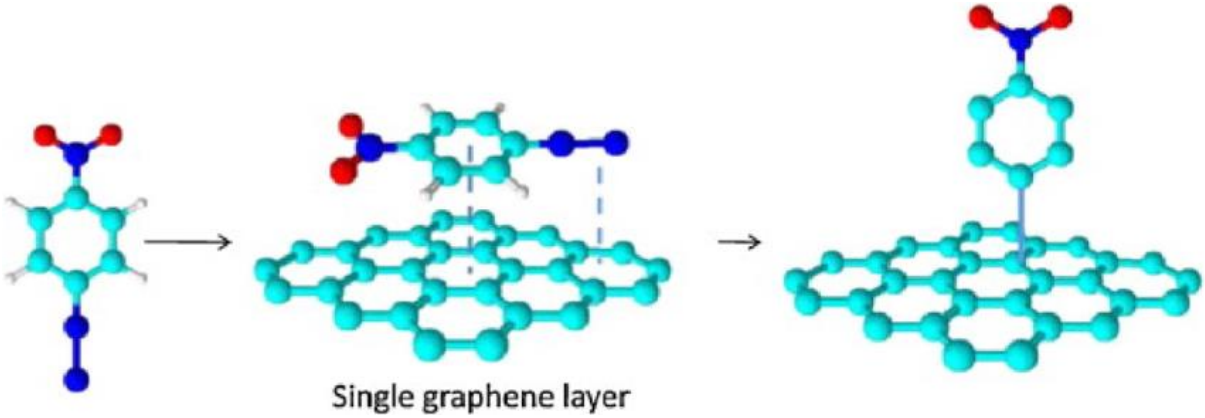

Figure 2.2: Illustration of electron grafting of aryl diazonium salt copied from Ref. (111)

In acidic environments, the diazonium salt is ionic and undergoes a polar reaction which results in an aryl cation. While under neutral or basic conditions, the reaction mechanism goes through a free radical step. Either way leads to a release of N_2 gas from the diazonium salts[117]. Successive reaction between aryl radical and graphene surface takes place [51, 55, 110-113]. The addition of aryl radicals to graphene [27, 38, 49-52] leads to the creation of carbon-carbon (C-C) bonds between graphene and organic chromophores (aryl moieties), and consequently accompanied by the formation of sp^3 centres protruding outside the plane[99] to replace the sp^2 hybridized carbons in the graphene honeycomb lattice.

Huddon *et al*[17] reported the first successful functionalisation of graphene with para-nitrobenzene via diazonium chemistry. They demonstrated with a help of Raman and STM analysis the degree of surface functionalisation and densities that have been produced by the chemical derivatization of epitaxial graphene as well as the related changes in the electronic and magnetic properties of the graphene surface layer. Englert and co-workers[21] used thermogravimetric analysis and mass spectroscopy (TGA/MS) to prove that 4-tert-butylphenyldiazonium tetrafluoroborate (4-TBD) functionalised graphene loses mass in two steps; small portion (1 %) at 210°C due to a removal of physiosorbed molecules and a large portion (12%) at a higher temperature 480°C due to the cleavage of the covalently bonded molecules, as compared to the standard which remained unchanged. Hossain *et al*, [22] reported STM and STS study on epitaxial graphene functionalised with 4-nitrophenyldiazonium tetrafluoroborate (4-NPD). STM images of the chemically modified graphene after annealing at ~500 °C in UHV showed that the adsorbed layer is covalently bound to the surface and contains a significant fraction of aryl oligomers. STS measurements reveal that the physiosorbed portions of the aryl oligomers do not significantly perturb the electronic structure of the underlying graphene and provide information about the band gap tuning, suggesting that high density organic covalent modification system can be used to tune the bulk electronic structure of graphene. Koehler *et al* [23], demonstrated how Raman spectroscopy can be used to differentiate between the physisorption and chemisorption. By exposing single layer graphene to a concentrated 4-nitrobenzyldiazonium tetrafluoroborate (4-NBD) solution as well as to the corresponding pure nitrobenzene, the authors observed a strong increase in the value of the integrated peak intensity ratio (I_D/I_G) initially and later detected an upshift of the G-peak position and a decrease of the 2D/G intensity ratio (I_{2D}/I_G), both confirmed doping[24]. Under many reaction conditions, a combination of either covalent binding or chemisorption (increased I_D/I_G) and

non-covalent doping or physisorption (shifts in the G and 2D peak, as well as decreased I_{2D}/I_G) is present.[26, 27]

Noteworthy, electron transfer chemistries depend on the Fermi energy level of graphene and the density of states of the reagents. Moreover, the reaction rate depends on the number of graphene layers, nature of edge, atomic structure, defects, and the electrostatic environment [100]. Raman spectroscopy can be conveniently employed to track the progress of reactions, and to estimate the differences in the reactivity between single layer graphene, bi-layer graphene, few layer graphene, tri-layer graphene and highly oriented pyrolytic graphene.[53, 148] The pioneering work published by Strano and co-workers[53] provided a detailed study on the reactivity of graphene of different layers (single and multilayers graphene sheets) using electron transfer chemistry. The sheets were prepared by mechanical exfoliation of bulk graphite on silicon wafers followed by annealing, and subsequent treatment with a diazonium salt to allow only the top layer and the edges of graphene sheets to react. They found the single layer graphene to be 10 times more reactive than the bilayer or multilayer materials using the Raman D/G ratio as a measure of the degree of functionalisation. Contributions from the edges were determined by examining the D peak intensity before and after diazonium functionalisation, this is because the intensity of the disorder (D peak) for graphene edges is polarization dependent. The authors observed at least two-time higher reactivity of the edge than the bulk for single-layer graphene[53-54, 110].

2.4 Covalent Radical Functionalisation Using Visible Light Chromophores

Incorporating dyes or chromospheres to pristine graphene with zero band gap, does not only tune the graphene or shift the photo-response of the composite towards the visible region of the spectrum, but can also improve its photocatalytic efficiency [2, 6].

Our group reported two powerful photochemical and covalent radical grafting method that offers a graphene modification using photoactive dye (phenazine) induced by white light to produce the of graphene/phenazine composite with improved solubility and tuned band gap of 1.95 eV and 0.8 eV respectively. The first functionalisation method was conducted using multi-layer graphene nanoplatelets and they have shown to produce a new type of 3D-graphene hybrid[20], using Raman, PXRD, FTIR and UV-Vis and Fluorescence spectroscopy characterisation methods. While the second method was reported on graphene grown on technologically important cubic silicon carbide (SiC). Result demonstrated a self-limited growth of one monolayer of the phenazine molecules that are standing up on the graphene surface and exhibit a short-range order with a rectangular unit cell. Density Functional theory (DFT) calculations based on scanning tunnelling microscopy (STM) results revealed the model for the phenazine over- layer and show the covalent attachment to every eighth carbon atom of the individual graphene. Based on the STS analysis and total DOS calculations of their findings, phenazine-graphene hybrid exhibited band gap of 0.8eV[28]. Dmitri *et al*[98] reported a high yield, simple and stable covalent functionalisation of phenazine over a single layer graphene grown on β-SiC (001) wafer via diazonium chemistry. Stability of the composite was measured using x-ray photoelectron spectroscopy (XPS) after sonication and annealing under ultra-high voltage (UHV). Orientation of the molecules on the graphene/SiC wafer was identified using near edge x-ray absorption fine structure (NEXAFS) and scanning tunnelling microscopy (STM). STS measurements and secondary electron cut-off revealed a modification of the electronic structure during the functionalization, which results in the emergence of a bandgap in the DOS of the phenazine dye/graphene system in some cases exceeding 2 eV and a change of the work function.

2.5 Materials and Methods

Materials. High purity (99%) graphene nanoplatelets (GP) were obtained from Sigma-Aldrich. Organic dyes (7-Amino-2-methylchromone, 9-Aminoacridine, 1-Amino-4-hydroxyanthraquinone, 3-Amino-7-dimethylamino-2-methylphenazine hydrochoride, 6-Aminoflourescein and 3-7-diaminophenothiazin-5-ium chloride), 50% tetrafluoroborate, sodium nitrate, , LMW and HMW chitosan, were obtained from Sigma-Aldrich and Acros Organics and used as received. All reactions were stirred with a magnetic stirrer unless otherwise stated.

Materials Characterisation. Infrared spectra (IR) were recorded from the solid phases using a Bruker Alpha Platinum ATR FTIR spectrometer with vibrational frequencies given in cm^{-1}. The electronic absorption spectra were recorded using a Cary 100 UV-Vis scanning spectrophotometer. Spectrophotometric experiments to assess the photocatalytic and adsorption abilities of the materials were carried out using a Cary 50 UV-Vis spectrophotometer controlled at 20^{o}C by a single cell Peltier accessory, while Mercury and Xenon lamps were employed as the source of visible and UV lights, respectively. X-Ray diffraction (XRD) of the materials were recorded on Bruker D2-Phaser diffractometer using Cu Kα radiation, with a step size of θ = 0.01013°. To calculate the lattice spacings Bragg's law was used and Lorentzian fitting was used to measure the full width at half maximum (FWHM) of the diffraction peaks, and number of layers was calculated using the formula: $(N_L\text{-}1) \times d_{002} = {}^{k\lambda}/_{FWHM_{002} \times \cos(\theta_{002})}$, where λ is the power source wavelength, k is constant based on the shape of the crystallite, Scharer equation $D = K\lambda/\beta\cos\theta$, was used to determine the crystallize size of the materials. Brunauer-Emmett-Teller (BET) surface area measurements were performed using a Micromeritics TriStar 3000 instrument. The samples were degassed in N_2 at 110 °C for 3 h before analysis and N_2 adsorption and desorption isotherms were measured at 77 K.

Transmission electron microscopic (TEM) analysis was carried out using the FEI Titan Themis Cubed operated at 80 kV. Samples were prepared by dispersing the powders in IPA, sonicating and then drop casting onto holey carbon TEM grids. Bright field TEM images were collected on a Gatan Oneview 16Megapixel CMOS detector. TGA analysis was carried out on a TGA SDT Q600 V.2.09 build 20, under air condition with a heating rate of 5^{o}C/min from room temperature to 900^{o}C, to identify the purity of graphene, thermal property of graphene, its composites, and relative weight loss resulting from heat flow.

2.5.1 General procedure to fabricate graphene-dye systems. Method A.[20]

In brief, an appropriate amino compound (5.04 mmol) was dissolved in HBF_4 (7 mL; 50 % w/w H_2O) and stirred. Then, sodium nitrite (5.04 mmol, 0.35 g) in 2 mL of H_2O was added dropwise and the reaction was left stirring for 2 hours. A small volume of diethyl ether (5 mL) was added and the diazonium salt was collected by vacuum filtration. Graphene (50 mg) was suspended in EtOH (100 mL) and sonicated for 30 min. A solution of the diazonium salt (0.262 mmol) was added to the graphene suspension, and the mixture was illuminated with white LED light (2,000 lumen) for 2 hours under stirring. The resulting dark blue coloured solution was washed several times with distilled water and ethanol, centrifuged at 6000rpm until no colour was observed in the supernatant. The materials were dried in an oven dryer overnight at 50^{o}C and collected as black powder.

2.5.2 General procedure to fabricate graphene-dye systems. Method B.

Typically, 80 mg of an appropriate amino compound was dissolved in 100 mL of ethanol in a 250 mL conical flask. 8 mL of 50 % HBF_4 was added to the solution, followed by 40 mg of $NaNO_2$ at 0^{o}C and stirred for 40 minutes to generate the diazonium salt. 100 mg of graphene nanoplatelets suspended in EtOH were added directly (*in* situ) to the generated diazonium salt. The resulting mixture was illuminated with white light (LED >2,000 lm) for

two hours under stirring. The resultant dark blue coloured solution was washed several times with distilled water and ethanol and centrifuged at 6000rpm until no colour was observed in the supernatant. The materials were dried in an oven dryer overnight at 50^{o}C and collected as black powder.

2.6 Results and Discussion

Our group have previously reported a method for graphene modification with phenazine dyes, which can be carried out on both multi-layer graphene (nanoplatelets, ca. 10 layers)[20] and quasi free-standing (graphene/SiC(001))[28]. This method (Method A, Figure 2.3) is a two-step process and relies on the production of diazonium salt from the corresponding amine of the organic compound. Firstly, a stable diazonium salt is generated and isolated followed by a second step, which involves the photochemical reaction between graphene and the diazonium salt. Here, we demonstrate that this method provides access to a series of graphene-chromophore systems containing acridine, phenazine, hydroanthraquinone and thionine.

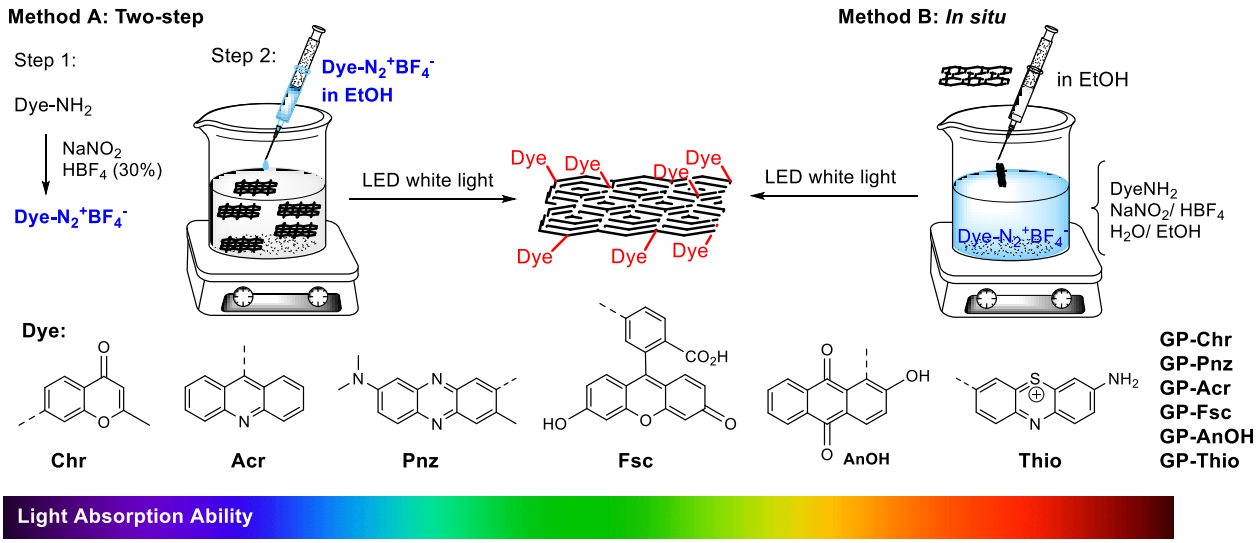

Figure 2.3: General strategies for fabricating graphene-dye composites: Method A (two-step procedure) and Method B (*in situ* one-pot).

However, this approach requires prior preparation, isolation and storage of the diazonium salt which may exhibit instability at room temperature, especially the aliphatic diazonium salts that lacks resonation and some para-aryl diazonium salts, which greatly limits the applicability of the method. Moreover, the tedious process of purification of the diazonium salt prior to the second step limits its overall efficiency. To overcome these issues, we have developed an alternative synthetic methodology (Method B, figure 2.3), which can be applied to a variety of different amines and requires no prior isolation of the corresponding diazonium salts. In Method B, the fabrication of graphene-chromophore system is carried out as one-pot procedure. Here, the diazonium salt is generated *in situ* avoiding unnecessary isolation by stirring $NaNO_2$ and the corresponding amine for 40 minutes at low temperature. Then, graphene nanoplatelets are added directly to the mixture; and illumination with white light initiates the reaction between graphene and the diazonium salt. Importantly, both methods require illumination with white light for modification of the graphene surface, including those chromophores which have no absorption in visible region. This observation further confirms our suggestion that hot electrons in graphene are responsible for the initial step of electron transfer from the occupied states of graphene to unoccupied states of diazonium salt, releasing nitrogen gas and generating a chromophore based radical.

2.6.1 Analysis by Fourier Transform Infrared Spectroscopy (FTIR)

Figure 2.4 (a-f) shows FTIR spectra between 4000 and 750 cm^{-1} for the series, which are notably different from unmodified GP as the GP spectrum is almost featureless. All materials; Yellow, Orange, blue, green, olive and violet representing GP-Chr, GP-Acr, GP-Acn, GP-Pnz, GP-Fsc and GP-Thio respectively, have enhanced and new bands between

1900-1500 cm^{-1} region corresponding to C=C, C=O (conjugated), C=N stretches. The fingerprint region (1500-750 cm^{-1}) shows a range of C-O (aromatic) and C–N (aromatic) stretches, N-H and O-H bending modes and a range of C=C and =C–H bending modes (out-of-plane), as well as the ring torsion bending vibrations.

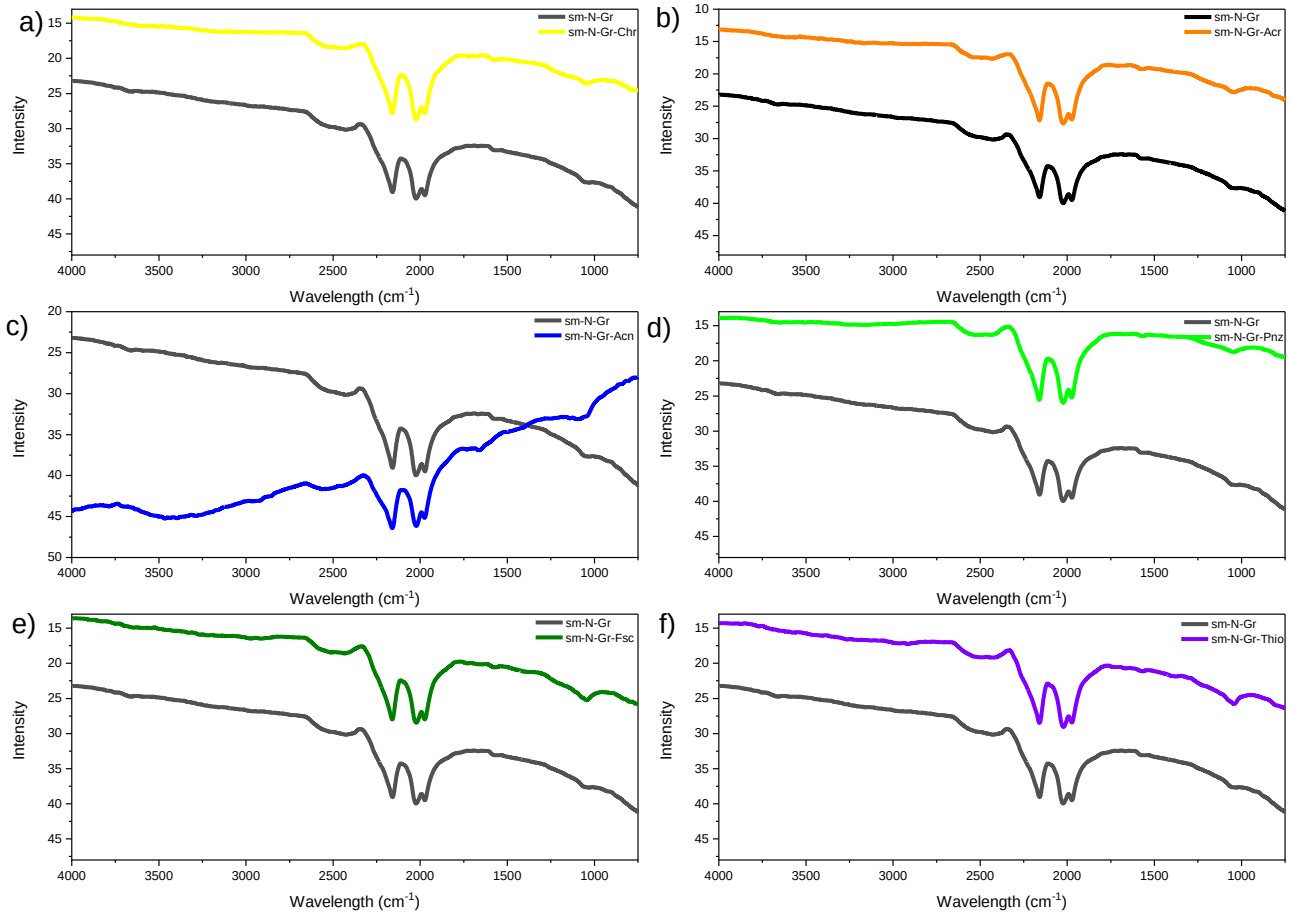

Figure 2.4: Normalised FTIR spectra (absorbance mode) of the graphene and graphene materials; a) The black spectra present in all the graphs represents pristine graphene, and yellow spectrum represents GP-Chr composite, b) Orange spectrum, represents GP-Acr composite, c) Blue spectrum represents GP-Acn composite, d) Green spectrum represents GP-Pnz composite, e) Olive spectrum, represents GP-Fsc composite and f) Violet spectrum represents, GP-Thio composite.

2.6.2 Analysis by UV-Visible Absorption Spectroscopy

Optical properties of the modified graphene samples were substantially altered compared to unmodified GP, which shows a typical absorption band at 270 nm. UV-vis spectra of the materials shown in

Figure 2.5, demonstrate that the modified materials containing a white light absorbing chromophore e.g. GP-Pnz (green, λ_{vis} 461 nm), GP-Acr (orange, λ_{vis} 403 nm, 428 nm), GP-Fsc (olive λ_{vis} 455 nm, 488 nm), GP-Thio (violet, λ_{vis} 601 nm, 652 nm) have additional bands in the visible region, which matches the optical behaviour of the chromophore itself. Also, GP-Chr (yellow) and GP-AnOH (blue) have significant broadening of the UV-band between 300-400 nm, which is attributed to π-π* transitions of the chromophores, which are efficient UV-absorbers. In addition, UV spectrum of GP-AnOH tails of into visible region, although no specific bands can be detected.

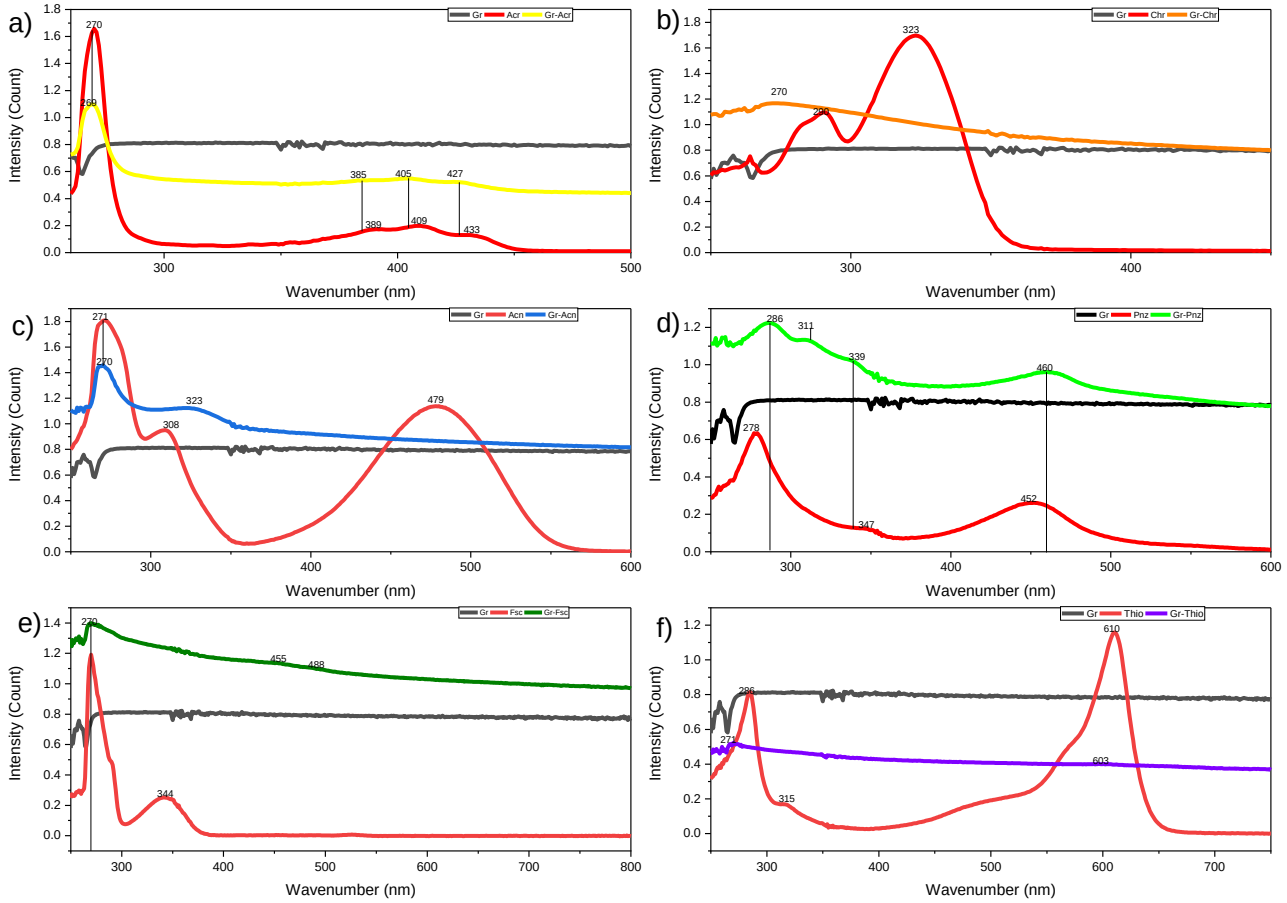

Figure 2.5: UV-Vis Absorption spectra of the organic chromophores, graphene and its composites; The black and red coloured spectra appeared in all the graphs (a-f) represents pristine graphene and dye chromophores respectively. a) GP-Chr (yellow), b) GP-Acr (orange), c) GP-Acn (blue), d) GP-Pnz (green), e) GP-Fsc (Olive), and f) GP-Thio (Violet).

2.6.3 Analysis by Fluorescence Spectroscopy

The emission spectra for the samples were collected at the excitation wavelength of 350nm. A single emission band is observed in the visible region for Gr-Ch, Gr-Acr, Gr-Acn, Gr-Pnz, and Gr-Thio at 437, 425, 420, 416, 425nm, respectively. However, Gr-Fsc showed two peaks at 425 and 512nm. The band at 512nm is likely due to fluorescein, which is a product of degradation of the corresponding diazonium salt.

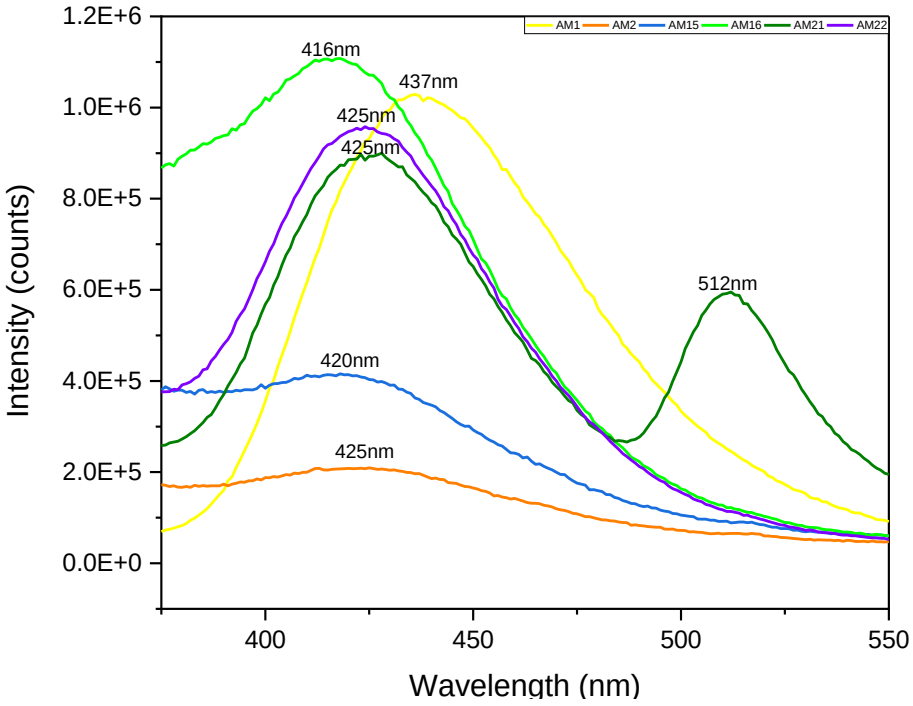

Figure 2.6: Fluorescence spectra of the graphene composites collected with the excitation wavelength of 350 nm. The coloured lines spectra representing GP-Chr (yellow), GP-Acr (orange), GP-Acn (blue), GP-Pnz (green), GP-Fsc (olive), GP-Thio (violet).

2.6.4 Analysis by Powder X-Ray Diffraction (PXRD)

Figure 2.7 shows XRD patterns recorded for non-modified and modified samples. The diffraction peaks at 26.8^{o} (002), 44.2^{o} (101) and 55.0^{o} (004) are typical for graphene nanoplatelets.

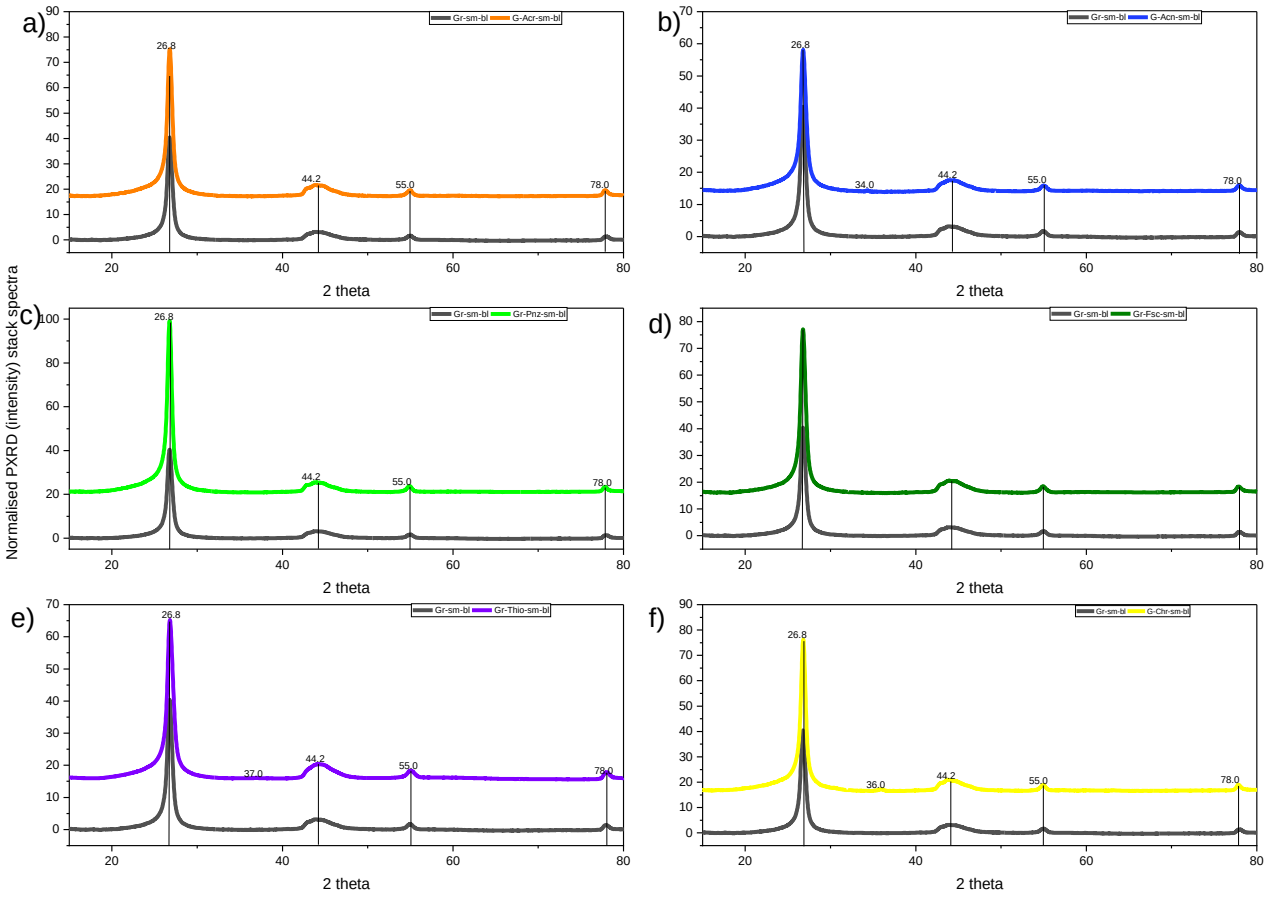

Figure 2.7: Normalised PXRD stack spectra (intensity count) of the graphene and its composites; a) The black spectra present in all the graphs represents pristine graphene, and orange spectrum represents GP-Acr composite, b) Blue spectrum, represents GP-Acn composite, c) Green spectrum represents GP-Pnz composite, d) Olive spectrum represents GP-Fsc composite, e) Violet spectrum, represents GP-Thio composite and f) Yellow spectrum represents, GP-Thio composite.

Additional peaks were observed in f-yellow; Gr-Chr (36.0^{o}), b-orange; Gr-Acn (34.0^{o}) and e-violet; Gr-Thio (37.0^{o}). Lorentz peak fitting of the (002) peak provided FWHM (°) and d_{002} (Å) data which are summarised in Table 2.1. No significant changes to the structure of the nano flakes were observed upon modification; the FWHM values for the modified samples increase by only 12-38 % as compared to the unmodified GPs and the d_{002}-spacings do not show any significant variation from the unmodified sample. This indicates that no residual chemical species is present in the interlayer space as d_{002} = 3.32-3.33Å is too small to contain entities as large as an epoxy group (1.25Å) or a water molecule (2.75Å).[26] This confirms that the chemical signatures observed in IR spectra are on the surface of

the GP. XRD data has also been employed to estimate the number of graphene layers produced by layer-by-layer stacking using the method reported by S. H. Huh[27]. With increasing average number of layers, the sharpness of the (002) peak more closely resembles that of the graphite lattice as shown in Table 2.1.

Table 2.1: Summary of XRD data of the (002) peak and BET data for GP and the modified samples.

	2 *Theta* (^{o})	FWHM (^{o})	d_{002} (Å)	SSA (m^2/g)	Relative decrease of SSA (%)	D(nm)
GP	26.77	0.615	3.33	430	0	164.15
GP-Chr	26.79	0.730	3.33	229	47	159.22
GP-Acr	26.78	0.745	3.33	301	30	155.17
GP-Pnz	26.75	0.694	3.33	152	65	164.81
GP-Fsc	26.78	0.729	3.33	271	37	158.58
GP-Can	26.79	0.790	3.33	224	48	147.13
GP-Thio	26.82	0.847	3.32	232	46	139.53

2.6.5 Analysis by Brunauer-Emmett-Teller (BET)

This analysis reveals a stark reduction in the specific surface area (SSA) of the modified GP samples as compared to original GP (430 m^2/g). The data summarised in Table 2.1, shows that the surface area has been reduced by 65% for GP-Pnz closely followed by GP-Acn, Gr-Chr and GP-Thio, when compared to unmodified GP. The apparent SSA reduction indicates successful modification of the graphene surface by chromophore moieties considering the changes in the crystallite sizes of the materials. Although, some change in SSA could be attributed to an increased aggregation of the modified platelets (compared to pure GP) partially restricting nitrogen access to the GP surface populated by chromophore units. Still, such an increase in aggregation reflects modification of the

surface. These results along with the analysis of XRD data for (002) peak, strongly suggest that the GP surface has been successfully functionalised by organic molecules. The crystallite size of the composites decreased from 3-15% compared to the unmodified graphene; GP-Chr (3%), GP-Acr (5%), GP-Acn (3%), GP-Fsc (10%) and GP-Thio (15%) may be due to defect. However, the crystallite size of GP-Pnz slightly increased by 0.4%, which corresponds with hignest reduction rate (65%) of the graphene surface area, probably due to high rate of functionalization

2.6.7 Analysis by Transmission Electron Microscopy (TEM)

To understand the arrangement of the molecules on the graphene surface TEM analysis of selected samples such as GP, GP-Pnz, GP-Fsc, GP-Chr and GP-Thio was performed. Figure 2.8 shows TEM bright field phase contrast images and their corresponding Fast Fourier Transformation (FFT) power spectra for graphene nanoplatelets modified with phenazine, chromone and fluorescein molecules, respectively. In all cases TEM shows a rather smooth surface (2.8 a-d), however the individual molecules cannot be resolved due to instrumental limitation. Important findings emerge by analysing the FFTs of the images, which are equivalent to electron diffraction patterns. Each FFT in Figure 2.8e-h, shows several sets of symmetrical spots relative to the central spot. Since FFT power spectra represent reciprocal space, larger distances from the central spot correspond to smaller distances in real space. For the GP-Pnz sample there are two sets of spots, denoted by blue and white circles that form two hexagonal patterns (Figure 2.8e). These two patterns are slightly rotated relative to each other corresponding to two different overlapping graphene nanoplatelets, which are randomly oriented on the imaging support. The other two sets of spots, denoted by green and red circles, form two rectangular patterns and correspond to two different domains of an attached phenazine layer. It is noted that the

patterns for the phenazine domains are rotated relative to each other by the same angle as for the graphene patterns.

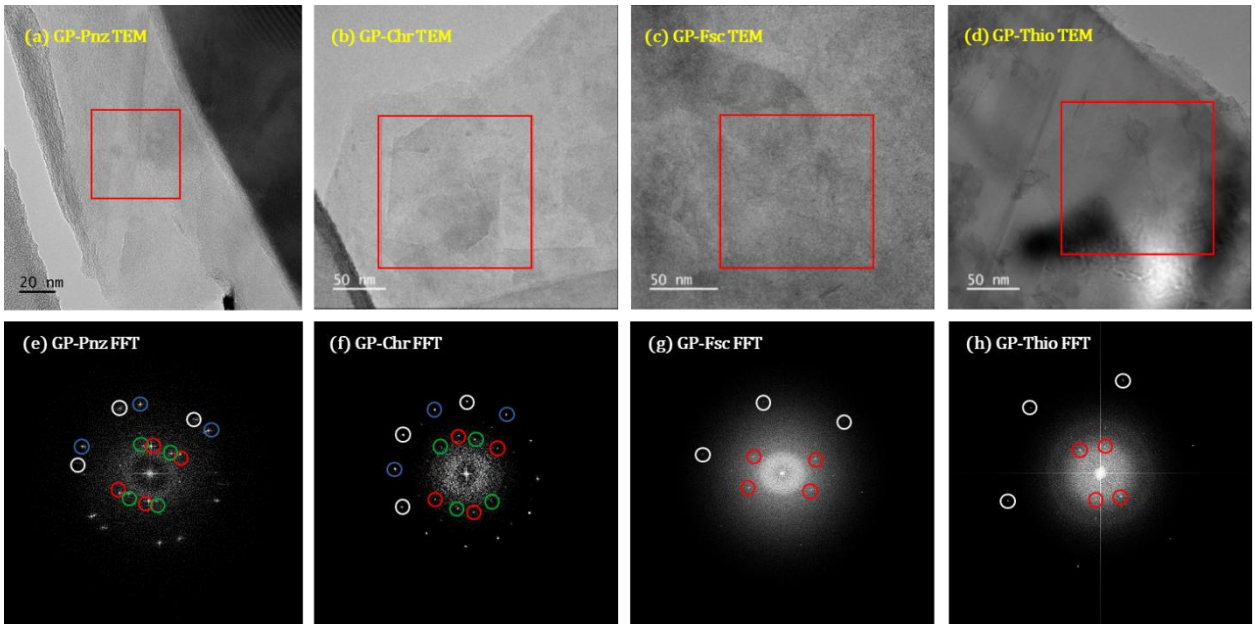

Figure 2.8: TEM images and their Fast Fourier Transformations (FFTs) for the samples: (a) GP-Pnz TEM image; (b) GP-Chr TEM image; (c) GP-Fsc TEM image; (d) GP-Thio TEM image; (e) GP-Pnz FFT image; (f) GP-Chr FFT image; (g) GP-Fsc FFT image; (h) GP-Thio FFT image. The areas used to calculate FFT images (e-g) are indicated by a red square in the corresponding TEM images (a-d).

Therefore, it is concluded that each graphene nanoplatelet is covered by a single well-ordered phenazine domain. Comparing the distances between individual spots from the phenazine domain and considering the graphene lattice parameter, the rectangular unit cell parameters of the phenazine layer are calculated to be 0.52 nm and 0.38 nm, in good agreement with a previous study of covalent modification of surface-supported graphene grown on cubic-SiC(001) by phenazine molecules.[25] The results therefore show that this modification method works well for the covalent attachment of phenazine molecules to graphene surfaces and the formation of ordered domains.

Similar results are observed for the FFT of the image of the GP-Chr sample (Figure 2.8f), where two rectangular patterns (denoted by green and red circles respectively), rotated relative to each other by the same angle as for the graphene patterns, represent two different domains of the attached chromone layer. Therefore, it is concluded that each graphene nanoplatelet is covered by a single well-ordered Chr-domain. The unit cell parameters of the chromone layer are calculated to be 0.48 nm and 0.30 nm. The similarity of the FFT patterns obtained for GP-Pnz and GP-Chr samples is unsurprising since the molecules both attach to the graphene surface via C-C bonding of the fused aromatic ring system (Scheme 2.1, represented by a dashed line). Therefore, Pnz and Chr chromophores are both standing up on the surface[25] resulting in a comparable molecular layer pattern on graphene.

For the GP-Fsc and GP-Thio samples (Figure 2.8g and h), there is one hexagonal pattern (spots denoted by white circles) that corresponds to a single graphene nanoplatelet. For both samples, one set of spots (denoted by red circles) forming an oblique unit cell, has been identified for the layer created by attached chromophore units. Hence, it is concluded that in each case graphene nanoplatelets are covered by a single well-ordered domain of the corresponding chromophore moieties. The calculated unit cell parameters are 0.63 nm and 0.32 nm for fluorescein layer and 0.91 nm and 0.44 nm for thionine layer.

Overall, the TEM/FFT results for the samples presented in Figure 2.8 provide strong evidence that the modification methods described in this work lead to formation of quite ordered domains of organic molecules bonded to the graphene surface. Due to defects of the graphene surface and non-uniform nature of nanoplatelets, some disordered regions have also been observed.

2.6.8 Thermogravimetric Analysis (TGA)

Like PXRD, TGA has been employed to identify the extent of functionalisation of graphene by various chromophoric groups. Graphene and functionalised graphene samples were exposed to a gradual temperature increase between 0-900^{o}C over a certain period of time and the mass loss has been recorded in percentages.

Figure 1.9 shows the thermal degradation for the individual dyes, modified and unmodified graphene, while figure 1.10 represents normalised TGA 1st derivatives of the composites and their respective starting dyes. Initial mass loss due to moisture and adsorbed air is observed between 0-42^{o}C for all graphene samples. A complete pyrolysis of unmodified graphene is achieved by 710^{o}C, which corresponds to 99.4% of the total mass loss. This total %mass loss can be used as a purity check of the material. The starting dyes have two key degradation regions between 170-370^{o}C and 370-620^{o}C, while the pyrolysis of the functionalised materials occurs within 570-820^{o}C range. The total %mass loss and the inflection temperatures of (T_i) for the graphene composites and their corresponding starting dyes is summarised in

Table 1.2. The total mass loss varies between 97.5% and 100% indicating a high purity of the materials in terms of graphitic content.

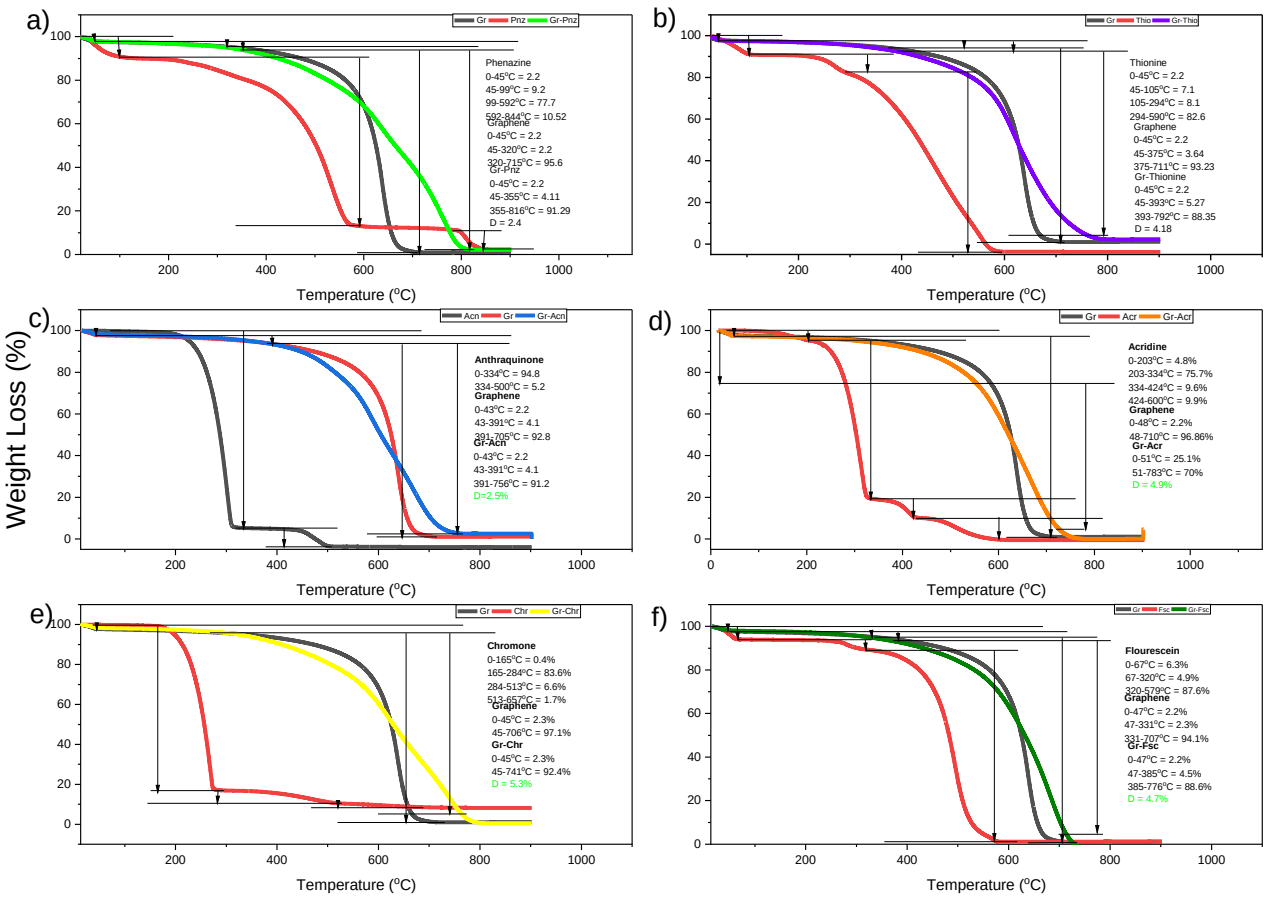

Figure 1.9: TGA thermograms for percentage mass loss of graphene, chromophores and the composites; The black and red coloured spectra appeared in all the graphs (a-f) represents pristine graphene and dye chromophores respectively. a) GP-Pnz (green), b) GP-Thio (violet), c) GP-Acn (blue), d) GP-Acr (Orange), e) GP-Chr (yellow) and f) GP-Fsc (olive).

Table 1.2: The total %mass loss and the inflection temperatures of (T_i) for the graphene composites and their corresponding starting dyes. (f=fast; s=slow process)

Gr-sample	T_i, ^oC	Total mass loss, %	Starting dye-NH_2	T_i, ^oC	Total mass loss, %
Graphene	637	99.4	-	-	-
Gr-Chr	620, 744	99.4	Chromone	269f, 462s	92.3
Gr-Acr	613, 670	100	Acridine	315f, 413s, 508s	99.8
Gr-Acn	590, 710	97.5	Anthraquinone	304f, 475s	100
Gr-Pnz	632, 764	97.6	Phenazine	302s, 533f, 809s	97.3
Gr-Fsc	595,721	99.7	Fluorescein	278s, 493f	98.8
Gr-Thio	620f, 737s	97.8	Thionine	268s, 456f, 555s	100

The inflection temperatures were attained from the first derivative analysis (Figure 3.10) and show distinct differences between starting materials and the modified graphene samples. After the initial loss of moisture and adsorbed air, the first derivative of unmodified graphene shows only one significant region with the inflection temperature of 637^{o}C.

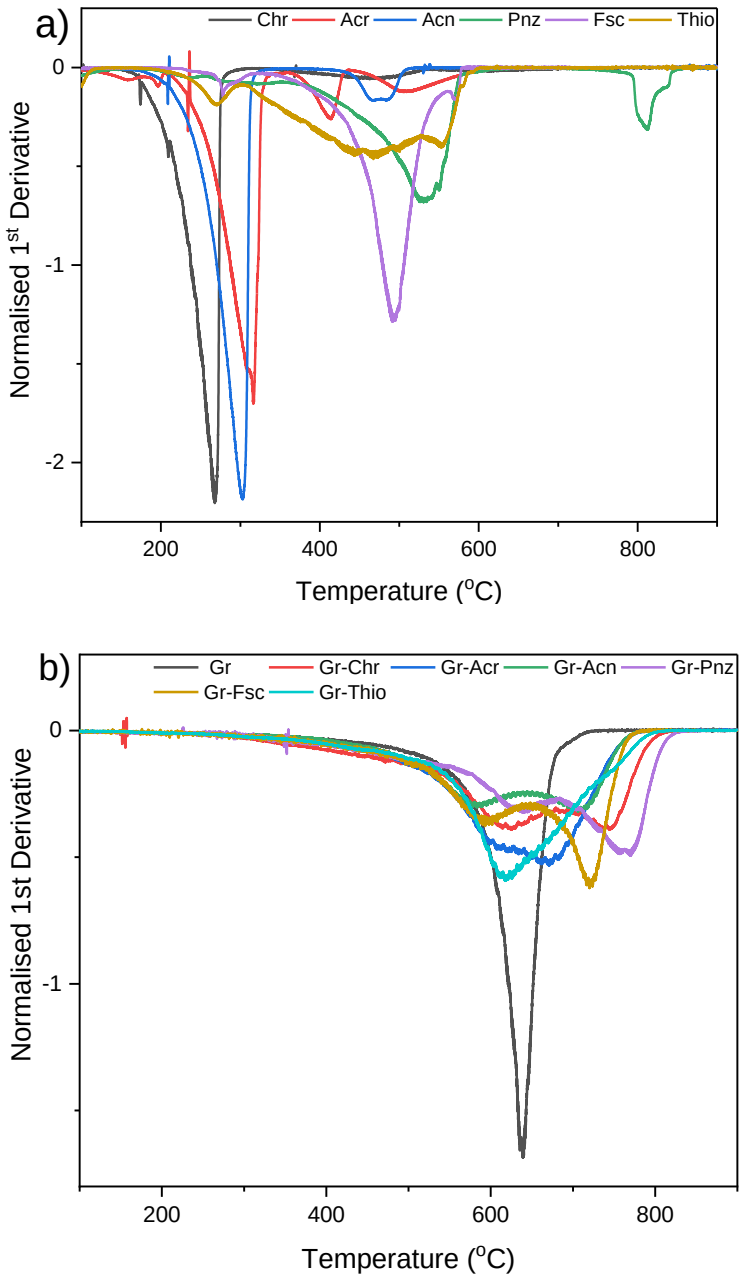

Figure 1.10: TGA 1st Derivatives for (a) starting dyes; Chr (black), Acr (red), Acn (blue), Pnz (green), Fsc (purple) and Thio (orange), (b) graphene (black) and graphene composites; Gr (black), Gr-Chr (red), Gr-Acr (blue), Gr-Acn (green), Gr-Pnz (purple), Gr-Fsc (orange) and Gr-Thio (cyan)

Initial amines of chromone, acridine and anthraquinone show a fast degradation process within 269-315 ^{o}C followed by a slow process at much high temperature (462-508^{o}C), while the fast process for phenazine, fluorescein and thionine occurs at a higher temperature range (493-555^{o}C).

The degradation pattern of the modified graphene samples prepared by radical method shows two key regions with the inflection temperatures ranges 590-632^{o}C and 670-764^{o}C. These high temperatures exclude the adsorption of the dyes by graphene surface. Both ranges show a comparable rate suggesting that the first range with the lowest (T_i) is likely due to the degradation of the defected graphene (due to radical functionalisation). While the second stage with higher temperature of graphene pyrolysis can be justified by an aggregation leading to a more graphite like materials.

2.7 Summary

Six different organic dyes with both UV and visible light absorption capabilities have been used to modify graphene nanoplatelets through radical functionalisation method (electron transfer) in one-pot reaction instead of previously reported 2-step method which was found to be more difficult and unapplicable to less stable diazonium salts. Samples were analysed using different characterisation methods to observe whether the dyes have been chemically (chemisorbed) or physically (physiosorbed) attached to the surface and in-between graphene layers. IR was used to identify differences in the functionality of the materials before and after functionalisation. UV-Vis absorption and fluorescence spectroscopy provided insight on optical properties of the samples. PXRD, TGA, and BET were used to observe the extent of graphene functionalisation. While TEM and FFT give

information about surface morphology of the samples and orientation of the organic molecules on the graphene surface.

2.8 Conclusion

The in-situ covalent radical functionalisation using simple and straight forward method was successful. FTIR analysis revealed enhanced and new bands in 1900-1500 cm^{-1} region corresponding to C=C, C=O conjugation and C=N stretches. Optical properties of all the samples demonstrated a significant improvement in the visible region of the electromagnetic spectrum between 400nm to 652nm compared to the original UV region (270nm) of graphene. Similarly, all samples revealed emission bands in the visible region from 416nm to 437nm with 350nm excitation. Substantial alterations were observed in the graphitic surface of the modified graphene using PXRD, BET and TGA analyses. FWHM data obtained by Lorentz peak fitting showed ca. 12-38% increase compared with unmodified graphene, this was supported by the SSA results of the BET analysis which showed a dramatic decrease in the surface area between 30-65%: Gr (0%), Gr-Chr (53%), Gr-Acr (30%), Gr-Acn-OH (43%), Gr-Pnz (65%), Gr-Fsc (37%) and Gr-Thio (46). TGA results showed two distinct regions in all the modified samples while graphene showed only one significant inflection point. In the first region, a lower temperature marked the oxidation initiation process of defected graphene, while higher temperature of pyrolysis can be explained by higher aggregation of graphene sheets leading to a graphite-like materials. TEM and FFT results provided significant information about changes on the surface morphology of the modified samples as well as the orientation of the organic molecules on it.

CHAPTER 3

Covalent and Non-covalent Functionalisation of Graphitic Surface by Chitosan: Two- and Three Component Systems

3.1 Abstract

Chitosan has many attractive properties such as biocompatibility, biodegradability, non-toxicity and the presence of functionality, a very reactive amino ($–NH_2$), secondary and primary hydroxy (–OH) groups in its backbone, makes chitosan an effective adsorbent material for the removal of wastewater pollutants. This chapter focuses on synthesising two component system containing graphene and chitosan, through ultrasonication and radical grafting and three component system, graphene with chitosan and chromophores, using one-pot and two-step radical grafting methods, respectively. Analysis of the surface properties (SEM, BET) and other characterisations (FTIR, UV, XRD, TGA) show successful modification of graphene surface.

3.2 Non-Covalent Functionalisation of Graphitic Surfaces

Non-covalent interactions primarily involve, van der Waals, electrostatic forces and hydrophobic that requires a physical adsorption of suitable molecules on the graphene surface. This can be achieved by polymer enfolding, adsorption of surfactants or small aromatic molecules, and interaction with porphyrins or biomolecules such as deoxyribonucleic acid (DNA) and peptides. Noncovalent functionalisation is a well-known technique for the surface modification of carbon-based nanomaterials. This technique has been previously employed extensively in the surface modification of the sp^2 networks of CNTs[68,99]. The non-covalent functionalisation is essential for the immobilisation of

proteins, enzymes, drugs and DNA, mostly as background of devices, which little alteration in the electronic characteristics of the π system can lead to a total change in the structure and properties of the system[56]. The advantage of non-covalent functionalisation is that it does not disrupt the extended π-conjugation on the graphene surface, unlike covalent functionalisation which creates defects on the graphene sheet. However, the fact that its bonding is not strong like covalent, makes it disadvantageous. Both graphene and GO can undergo π-π stacking and different schemes have been developed to form hybrid organic–graphene systems based on these interactions[35].

3.3 Materials and Methods

3.3.1 Two-Component System

One-pot radical transfer method: 80mg of low molecular weight (LMW) chitosan was added into a beaker containing 50mL of 1% AcOH/H_2O and stirred for 1hr for complete solubility followed with addition of 5mL HBF_4 and 5 min stirring. 40mg $NaNO_2$ was added at 0^oC and stirred for 30 minutes to obtain the chitosan salt. To this solution, 100mg graphene nanoplatelets was added and stirred under white light (LED; >2,500LM) illumination for 2hrs, followed by washing the hybrids with deionised water severally and dried under vacuum at 50^oC, 3mbar overnight.

Physical Mixture Method: 50mg of GNP was sonicated in 30mL DMF for 30 min. 30 mL of 1% acetic acid was added to the dispersion and further sonicated for 15 mins, followed by 100mg of Chitosan and sonicated for 1hr. The hybrid was centrifuged at 3500 rpm for 30 mins, then washed with deionised water and dried under vacuum at 50^oC, 3mbar overnight to remove the acetic acid from the hybrid.

3.3.2 Three-Component System

One-pot Radical Transfer Method: To synthesize a catalyst with multifunctional properties**,** 40mg each of dyes (chromone, acridine) were added separately into 50mL ethanol in a beaker and stirred for 15 min, to these solutions, 40mg chitosan dissolved in 50mL 1% AcOH/H_2O were added and continue to stir for 10 min. 8mL HBF_4 was introduced into these mixtures and stirred further for 5 min. The solution temperature was cooled to 0^oC, followed with 40mg $NaNO_2$ addition and 30 min stirring to obtain diazonium salts of dye and chitosan. 100mg graphene nanoplatelets was added to this mixture and stirred for 2 hours under white light (LED; >2,500LM) illumination for 2hrs, followed by washing the hybrids with deionised water severally and dried in an oven dryer at 50^oC, 3mbar overnight.

Two-step method: 80mg of aminobenzoic acid was dissolved in 100mL ethanol followed by adding 5mL HBF_4 and stirred for 5 minutes. 40mg $NaNO_2$ was added to the solution at 0^oC and 30 min stirring to obtain diazonium salt. 100mg graphene nanoparticles was added to the salt solution and stirred under white light (LED >2,000LM) for 2 hrs, followed by washing the hybrids with deionised water severally and dried under vacuum at 50^oC, 3 mbar overnight. Then, 100mg Gr-ArCOOH was dispersed in 50mL deionised water and sonicated for 5 min. 80mg chitosan dissolved in 50mL of 1% AcOH/H_2O was transferred to the dispersion and stirred for 3 hrs at 80^oC. The hybrid was washed several times with deionised water and dried in a vacuum at 50^oC, 3 mbar overnight.

3.4 Results and Discussion

3.4.1 Two-component system - Graphene-Chitosan

The two-component systems consisting of graphene and chitosan were synthesised according to the method described in Chapter 2 (covalent modification) and physical mixture method (non-covalent modification).

3.4.1.1 **Analysis by Fourier Transform Infrared Spectroscopy (FTIR) and** UV-Vis Absorption Spectroscopy

Figures 3.1 (a) summarise the changes in the samples prepared via two different synthetic procedures. The key features in chitosan show typical bands at 3360 (O-H), 2870 (C-H), 1640 (C=O), 1580 (N-H), 1422 (CH_2-OH), 1366 cm^{-1} and a broad one 1160-960 cm^{-1} (O-C-O) corresponding to the carbohydrate moiety.

Figure 3.1(b) represents 3 spectra: Graphene spectrum (Black) shows typical bands at 1559 cm^{-1} and 1973 cm^{-1} (C=C=C) of cyclic alkene, 1040 cm^{-1} (C=C=O), functional groups at the edges of basal plane in the nanoplatelets.

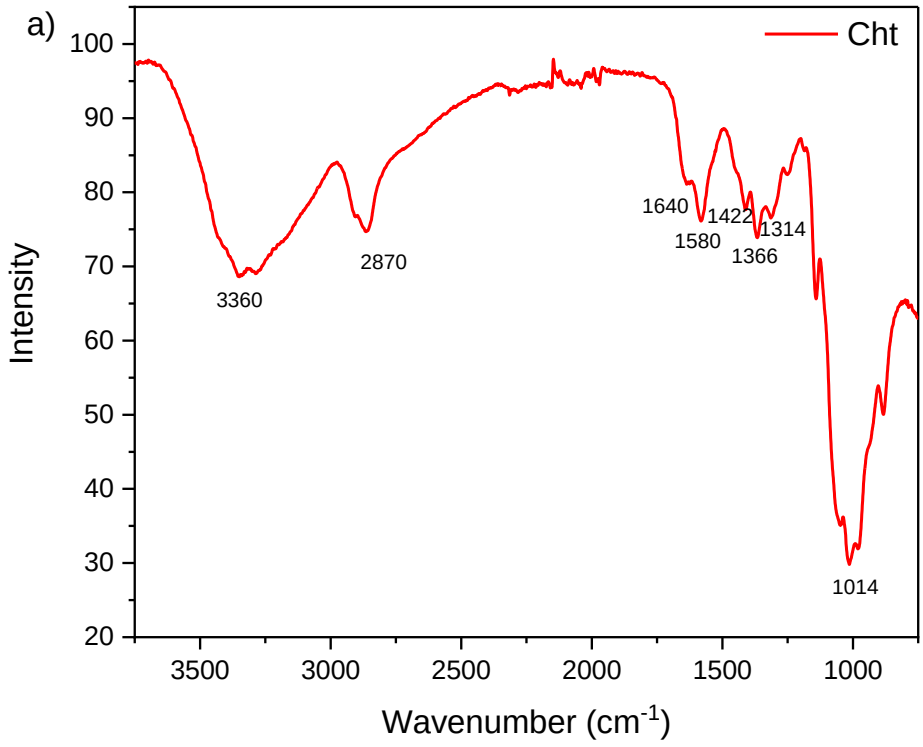

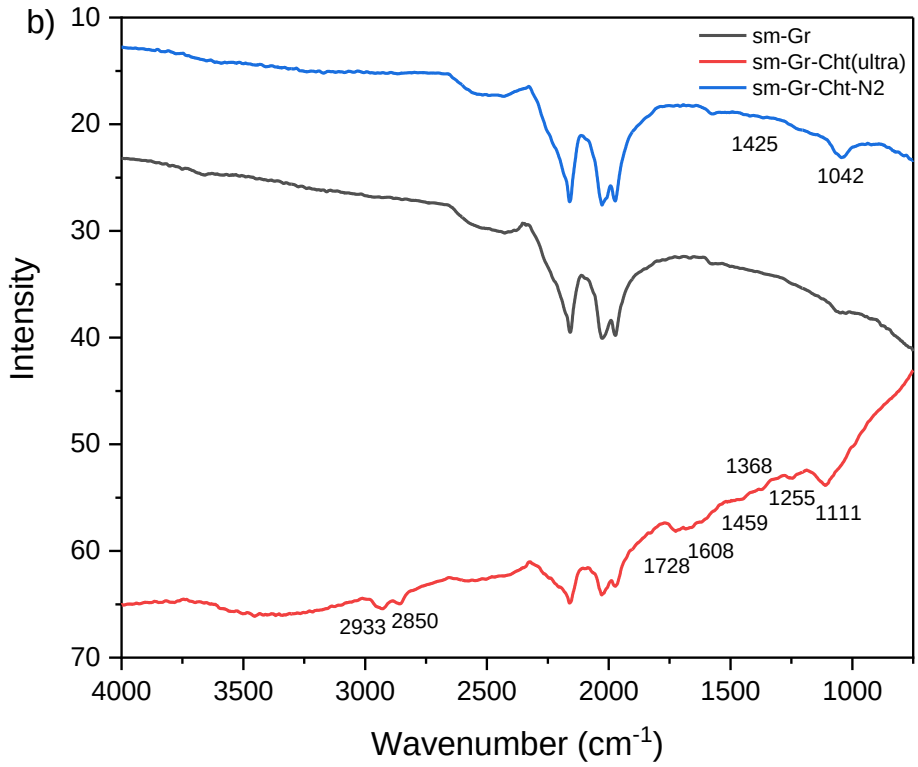

Figure 3.1: (a) FTIR spectra of chitosan. (b) FTIR spectra of graphene (Gr, black), Graphene-Chitosan physical mixture (Gr-Cht-PM, red) and Graphene-Chitosan covalent mixture (Gr-Cht-CM, blue)

Gr-Chitosan (blue) prepared via radical transfer method shows broad band at 1042 cm^{-1} due to sp^3-sp^3 (-C-C-) bonding from radical functionalisation of graphene by chitosan. Gr-Chitosan (Red) prepared by ultrasonication of graphene and chitosan mixture show more bands at 2933, 2850, 1608, 1368, 1255 and 1111 cm^{-1} suggesting higher concentration of carbohydrates in the sample.

UV-Vis absorption spectra of graphene and the functionalised graphene samples are shown in Figure 3.2 below. The absence of a defined absorption band but an increase in steep at 272 nm in the unmodified graphene used for this research was due to scattering of light by the platelets and their low dispersibility.

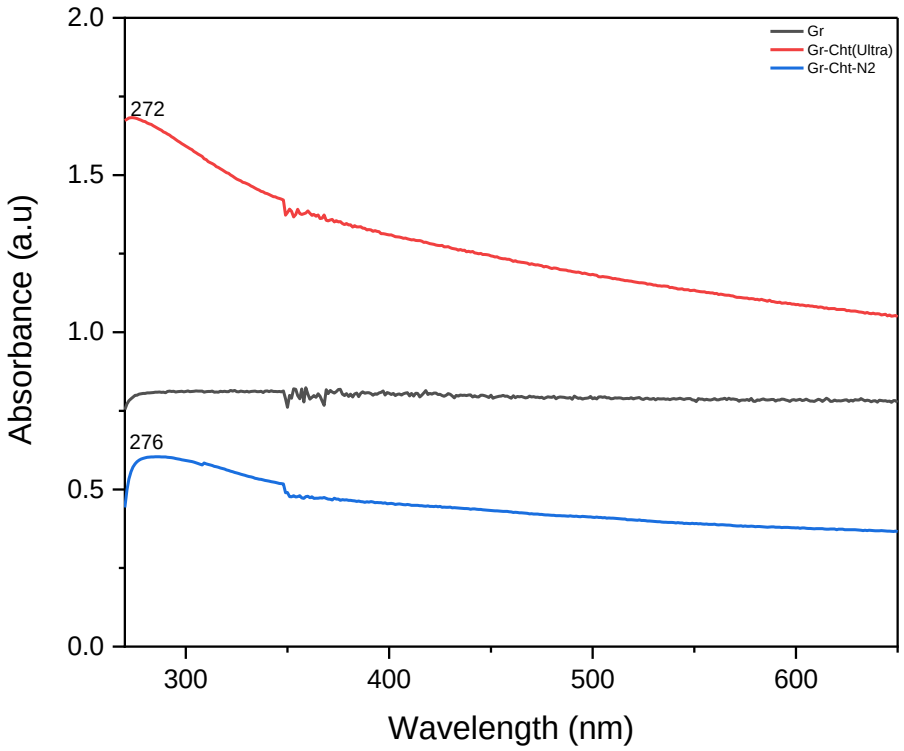

Figure 3.2: UV-Vis spectra of graphene (GP, black), Graphene-Chitosan physical mixture (GP-Cht-PM, red), Graphene-Chitosan covalent mixture (GP-Cht-CM, blue).

However, an absorption band was recorded at the same band position 272 nm for GP-Chit-PM (red). This band represents π-π transitions attributed to the graphitic surface as the work function of graphene and graphite are 4.42 eV and 4.7-4.8 eV, respectively. Clearly, the functionalisation leads to an increase in the dispersibility of the graphene platelets modified by ultrasonication (physical mixture method). In contrast, the spectrum of GP-Chit-CM resembles unmodified graphene platelets due to low modification degree, which is a disadvantage of the covalent modification.

3.4.1.2 Analysis by Powder X-Ray Diffraction (PXRD) and Scanning Electron Microscopy (SEM)

XRD patterns in

Figure 3.3 are presented for non-modified and modified samples showing diffraction peaks at 26.8^{o} (002), and 44.2^{o} (004), which are typical for graphitic materials. The green

spectrum represents XRD pattern of chitosan with diffraction peaks centred at 10.8^{o} (002), 20.40^{o} (110) and a broad shoulder between 30-40°. This peak (110) was observed at 21.0^{o} in red spectrum, signifying the presence of chitosan in the physical mixture.

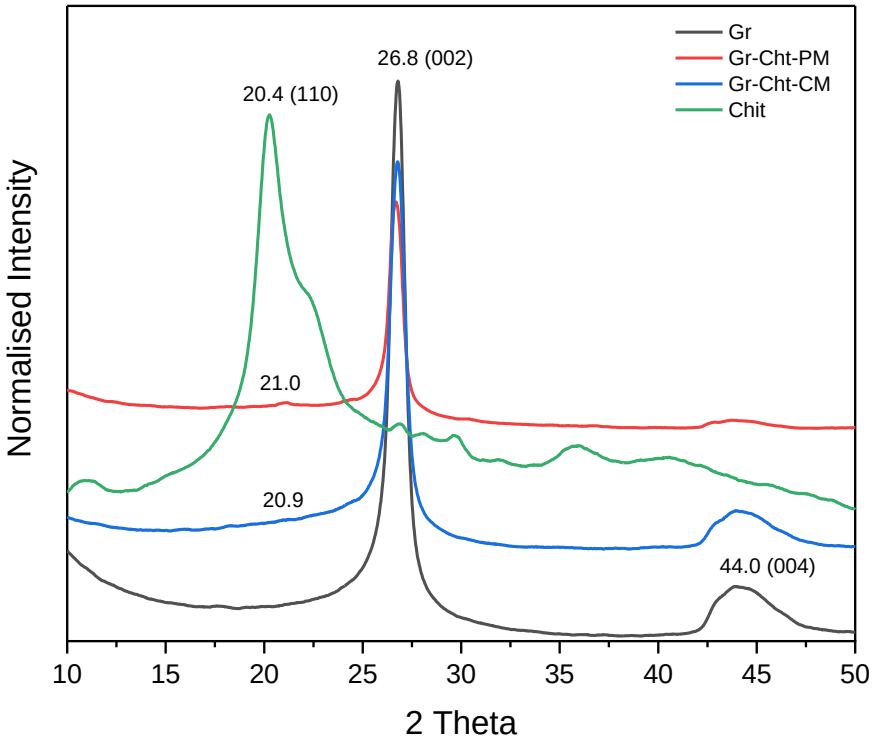

Figure 3.3: PXRD spectra of graphene (GP, black), Graphene-Chitosan physical mixture (GP-Cht-PM, red), Graphene-Chitosan covalent mixture (GP-Cht-CM, blue) and Chitosan (Chit, green).

A slight shift in strong band position, 20.30^{o} of chitosan to a very weak band 21.05^{o} in red was probably due ultrasonication of the mixture. Moreover, the crystallinity of graphene samples was observed to diminish in red due to amorphous nature of the chitosan present in the mixture. No additional peaks or much change were observed in the crystallinity of graphene in the spectra (blue) representing the modified graphene with chitosan by radical transfer.

This section describes the analysis of graphene and chitosan hybrids by scanning electron microscopy (SEM).

Figure 3.4 displays SEM images of untreated graphene nanoplatelets showing their fluffy structure due to amorphous carbon present.

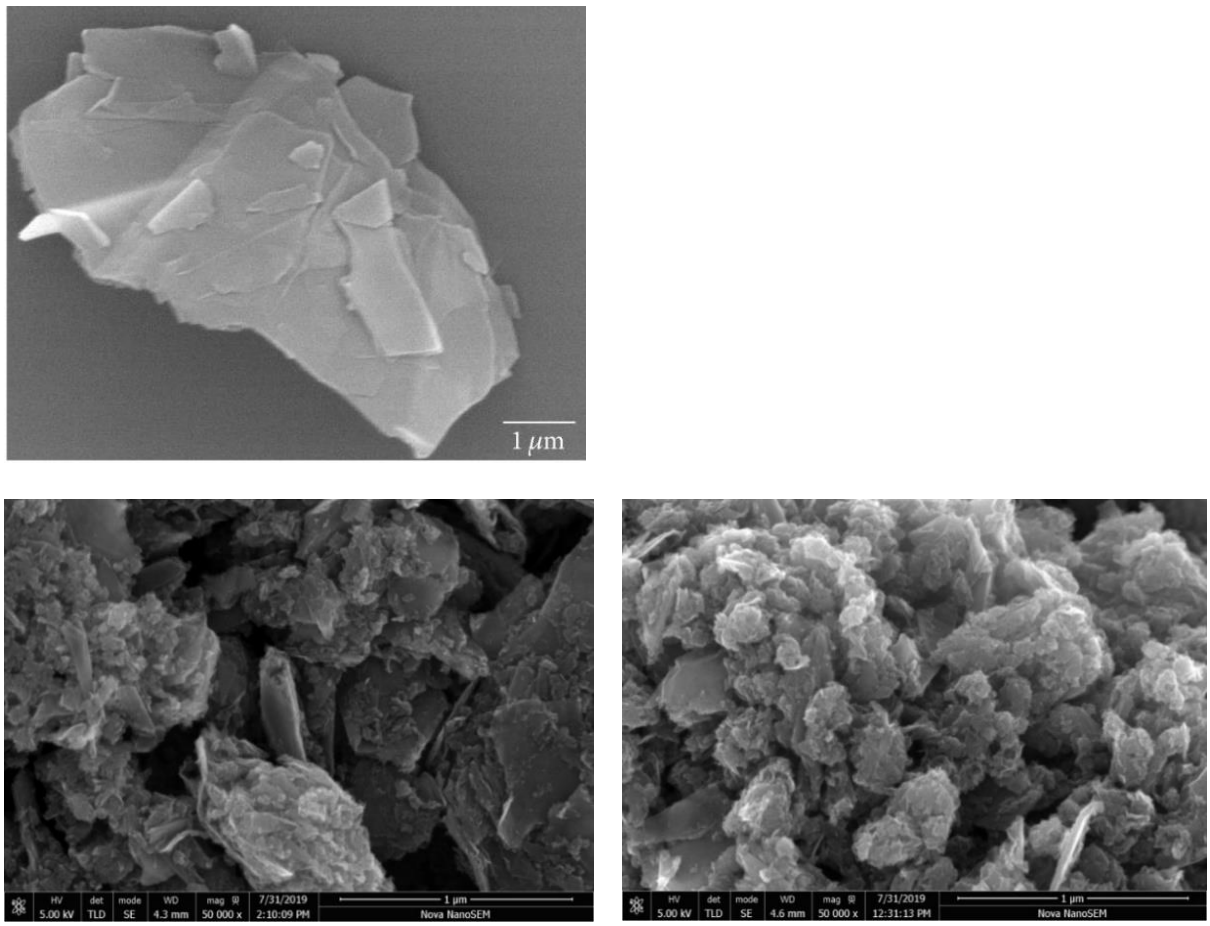

Figure 3.4: SEM Images of graphene samples: (top) graphene platelets (copied from Ref 245), (left) GP-Cht prepared by sonication, and (right) by radical chemistry.

The images for GP-Cht-PM (bottom-left) prepared by ultrasonication method showed grey clustered solids, which are partially covered by smaller clusters. (Bottom-right) show SEM images of GP-Cht functionalised by a radical method. The image displays a fused material (rock-like solid) with denser packing than that of the material prepared through a sonication route. The differences in packing and the flakes size can be a direct result of the covalent modification.

3.4.1.3 Thermogravimetric Analysis (TGA)

The thermal stability of graphene, freestanding and functionalised graphene-chitosan was tested by thermogravimetric analysis by exposing the samples to various temperatures up to 900^{o}C over certain period of time and the mass loss have been recorded in percentages.

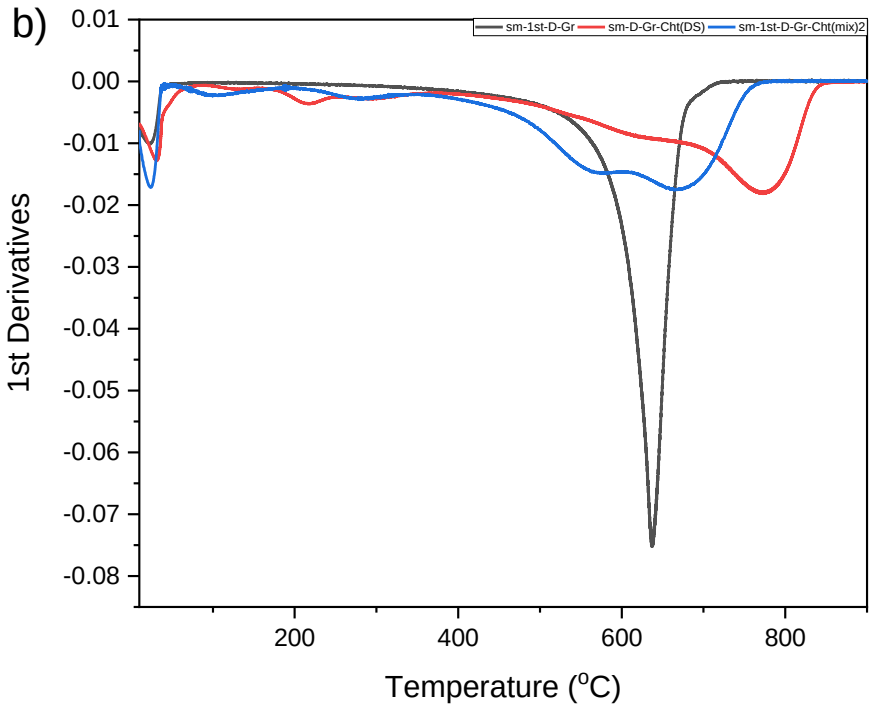

Figure 3.5 (left) represents TGA thermograms for graphene and modified graphene with chitosan. Normalised 1st derivatives of TGA for the composites and the respective graphene are shown in Figure 3.16 (left) in the appendix. A mass loss of 2.3% was observed in graphene (black) and the graphene composites between 0-42^{o}C due to removal of water. A complete pyrolysis is achieved by 710^{o}C for unmodified graphene. Initial loss due to moisture between 0-42^{o}C was also observed for both modified graphene samples. In the case of GP-Chit-PM, 5.7%, 6.0%, 51.4% and 33.3% losses were observed between 42-183^{o}C, 183-357^{o}C, 357-638^{o}C and 638-764^{o}C, respectively. While 5.7%, 3.1%, 11.3%, 21.9% and 56.6% mass loss occurred between 0-75^{o}C, 75-201^{o}C, 201-392^{o}C, 392-616^{o}C and 616-848^{o}C, respectively, for the modified graphene with chitosan via radical transfer (blue).

Figure 3.17 (right) in the appendix shows the first derivative analysis where three distinct regions of chitosan with the inflection temperatures of (T_i) of 275 °C, 475 °C and 597 °C can be observed. The first temperature is attributed to the main degradation of chitosan, while the consecutive steps relate to the carbonisation process[270-271].

After the initial loss of moisture and adsorbed air, the first derivative of unmodified graphene shows only one significant region with the inflection temperature of 637^{o}C. The degradation of the modified graphene prepared by physical mixture method (blue) has four regions with (T_i) of 100^{o}C, 274^{o}C, 574^{o}C and 667^{o}C, which can be attributed to a volatile residual, weakly bound chitosan, carbonisation of chitosan and pyrolysis of graphene itself, respectively. For the graphene-chitosan prepared by radical transfer method (red), the following inflection temperatures were recorded: 216^{o}C, 626^{o}C, and 772^{o}C. Lowest (T_i) is likely the initial degradation of chitosan functionalities followed by its carbonisation and finally pyrolysis of graphene. A higher temperature of graphene pyrolysis can be justified by a high degree of aggregation due to a lower presence of chitosan as opposed to the physical mixture. This aligns well with the observations found in UV-vis spectroscopic analysis, whereas graphene physical mixture has a better dispersibility.

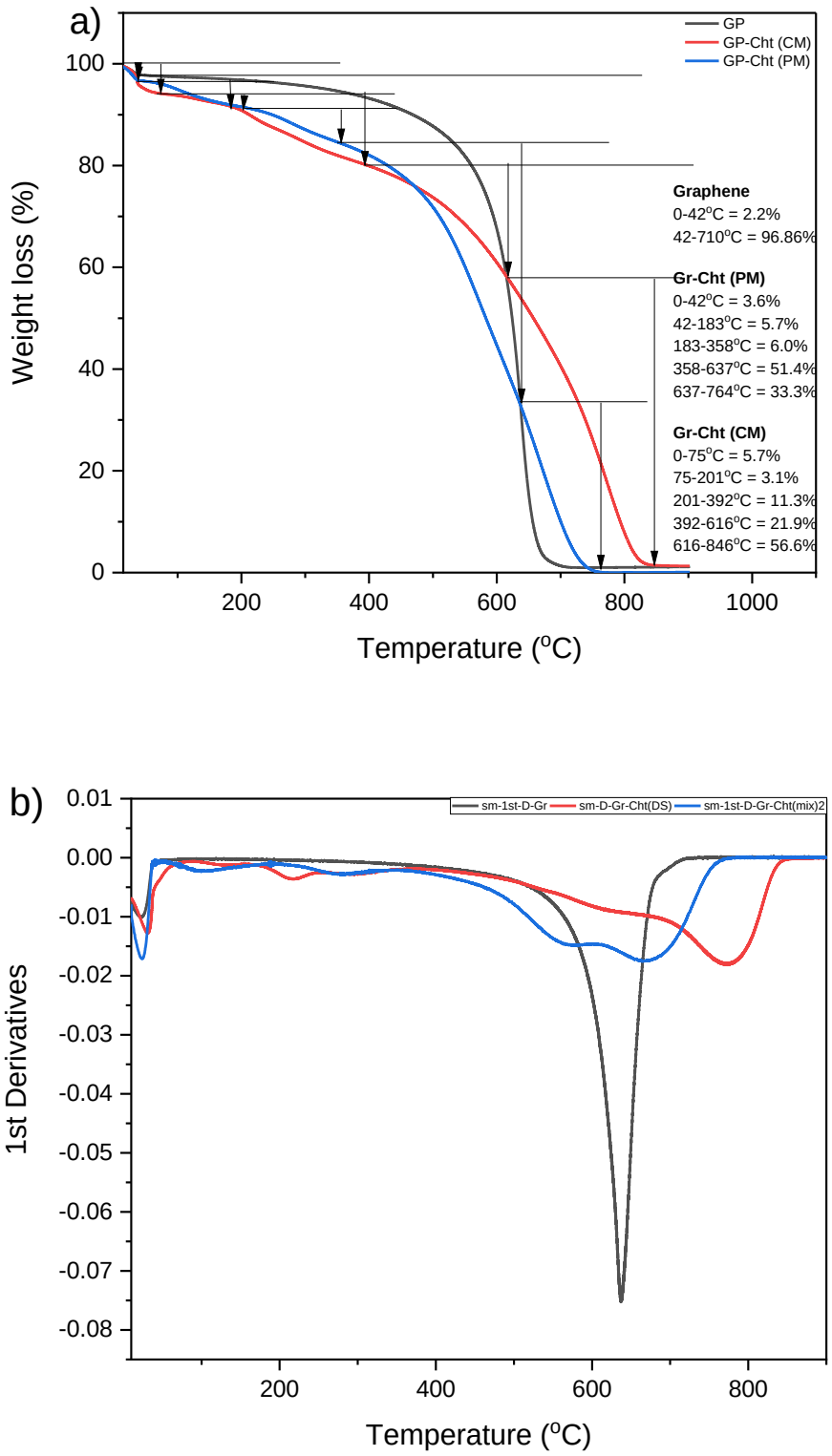

Figure 3.5: (a) Weight loss (%) against temperature and (b) normalized 1st derivatives thermogravimetric analysis of graphene (black), GP-Cht composite prepared by physical mixture (blue) and GP-Cht composite prepared by diazonium chemistry (red)

The Table 3.1 below provided a summary of the thermogravimetric analysis and BET values to understand the degree of surface modification. This data shows the thermal activity of the samples in the two key regions of the greatest change of the weight loss with the inflection temperatures above 550^{o}C corresponding to the pyrolysis of graphene matrix.

Table 3.1: Summary of BET data of two-component system and TGA values recorded at two key regions with inflection temperatures T_1 and T_2.

Sample	**SSA (m^2/g)**	**T_1 (^{o}C)**	**Weight loss (%) at T_1**	**T_2 (^{o}C)**	**Weight loss (%) at T_2**
Graphene	430.16			637	96.9
GP-Cht (PM)	287.68	637	66.7	764	33.3
GP-Cht (CM)	167.50	616	42	84	56.6
GP-ArCOOH	373.21	605	34.9	788	65

These two temperatures can represent two distinct stages of the pyrolysis:

low T_1 – temperature and associated weight loss can be attributed to the defected graphene sheets, for examples, containing sp^3-hybridised C-atoms due to covalent modification. Also, for chitosan samples, this region can be associated with final decomposition of this polymer. Thus, this region indicates possible modification of graphene through covalent and non-covalent means. Here, the degradation of the modified graphene samples occurred between the low temperature (T_1) ranges (0-637^{o}C) and the weight losses were recorded as follows: GP-Cht (PM) 66.7%, GP-Cht (CM) 42%, GP-ArCOOH 34.9%. GP-Cht (CM) recorded highest weight loss due to presence of physiosorbed chitosan on the graphene surface. Lower weight loss values of 34.9% and 42% for GP-ArCOOH and GP-Cht (CM) respectively, confirms the covalent modification of the graphene surface.

high T_2 – temperature and associated weight loss can be attributed to aggregation of graphene sheets; thus, forming more graphite like composites requiring higher temperature to degrade[115, 204].

3.4.2 Three-component system: Graphene-Chitosan-Chromophore

The construction of the three components system has been achieved in two different ways, *in-situ* and *two-step* procedure as described in the experimental section (3.5.2). The *in-situ* method is similar to two-component method described in chapter 1, except that, two different radical salts (dye, polymer) were introduced here. The hybrids were characterised using the standard set of techniques.

3.4.2.1 **Analysis by Fourier Transform Infrared Spectroscopy (FTIR) and** UV-Vis Absorption Spectroscopy

Figure 3.6, graphene spectrum (Black) shows typical bands at 1559 cm^{-1} and 1973 cm^{-1} (C=C=C) of cyclic alkene, 1040 cm^{-1} (C=C=O), functional groups at the edges of basal plane in the nanoplatelets. All spectra (Red, blue and green): Gr-Chr-Cht, Gr-Acr-Cht, Gr-Gnn-Cht respectively showed broad bands between 1032-1052 cm^{-1} due to sp^3-sp^3 (-C-C-) bonding from radical functionalisation of graphene by chromophores and chitosan. This is

similar to the pattern observed in the two-component GP-Cht-CM (blue spectra,

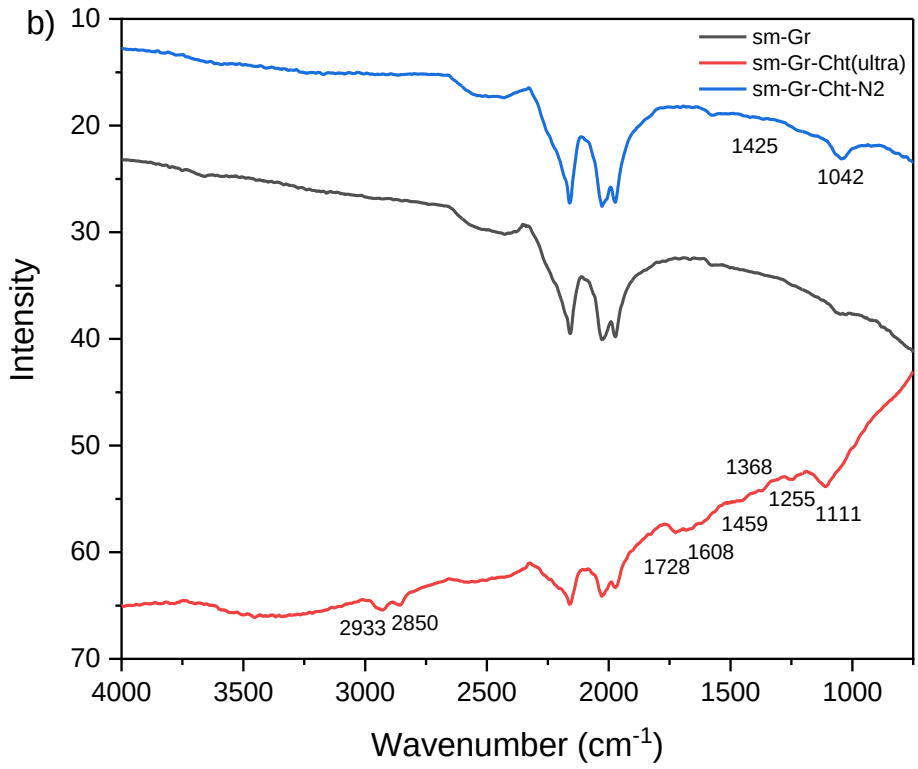

Figure 3.1) and GP-chromophores (

Figure 2.4 in chapter 2). Additional peaks were observed between 1700-1720 cm^{-1} for GP-Gnn-Cht and GP-Chr-Cht respectively, probably due to keto group of chromone, other peaks were identified between 1233-1236cm^{-1} for GP-Acr-Cht and GP-Gnn-Cht due to C-N stretching absorption of 3^{o} amine in acridine and guanine molecules, 756cm^{-1} for GP-Gnn-Cht due 2^{o} amine in the guanine molecule.

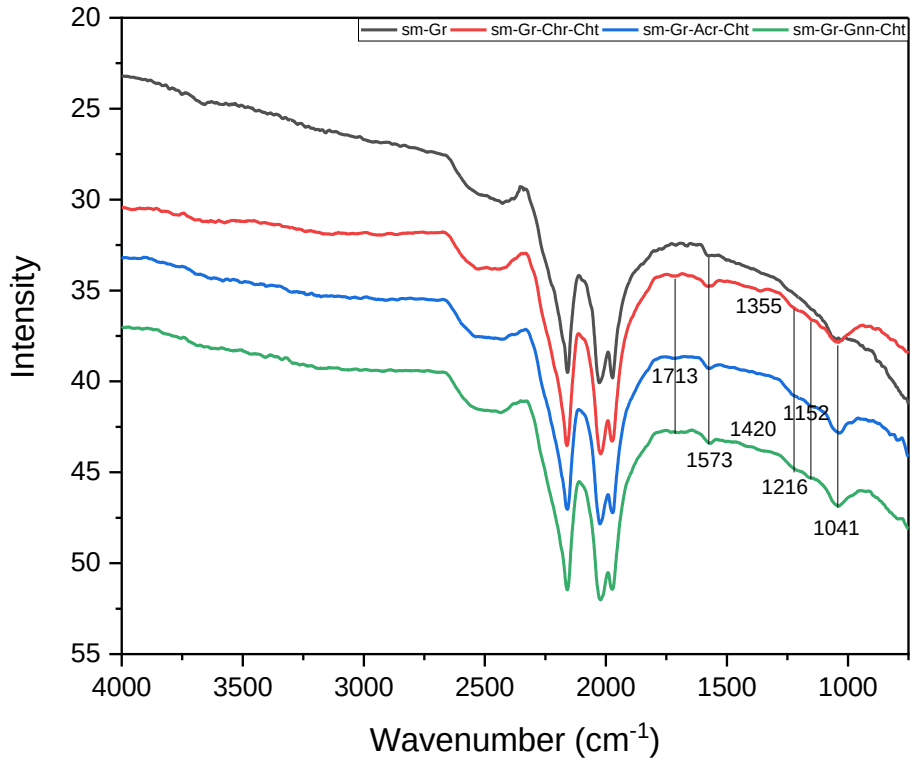

Figure 3.6: FTIR analysis of Graphene (black), Gr-Chr-Cht (red), , Gr-Acr-Cht (blue) and Gr-Gnn-Cht (green)

Similar to

Figure 2.5 in chapter 2, the optical properties of the modified graphene samples have significantly changed compared with unmodified graphene with typical absorption band at 270 nm.

Figure 3.7 shows UV-Vis absorption spectra of the modified graphene in three component systems;GP-Chr-Cht (red), GP-Acr-Cht (blue) and Gr-Gnn-Cht (green). Blue shift (hipsochromic shift) was observed at 385, 405 and 428nm in the GP-Acr-Cht from 389, 409 and 432nm (figure 2.5b) in the dye respectively, signifying functionalization of the dye and polymer. A blue shift was seen in the GP-Chr-Cht at 271 and 306nm from 291 and 323nm (figure 2.5a) in the dye spectrum with broadening of shoulder between 300-400nm as seen in the GP-Chr in

Figure 2.5 in chapter 2, attributed to π-π* transitions of the chromophores, which are efficient UV-absorbers. A disappearance of band at 319nm was observed in the GP-Gnn-Cht compared with its corresponding dye (see appendix; figure 3.18) confirming radical functionalisation of the graphene.

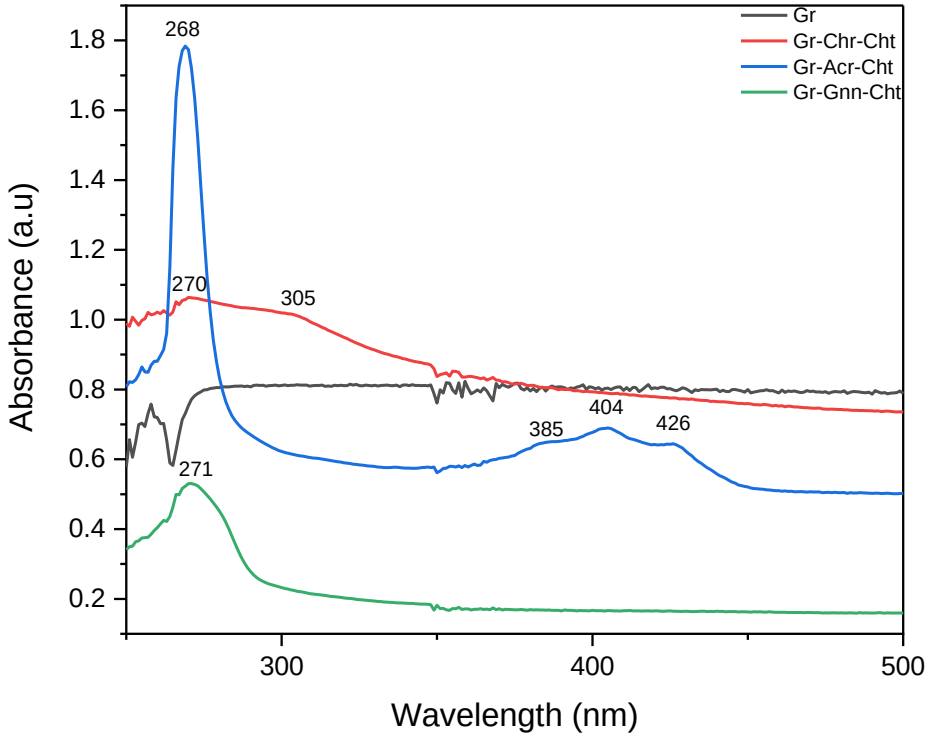

Figure 3.7: UV-Vis absorption spectroscopic analysis of Gr, Chr, Gr-Chr-Cht, Gr, Acr, Gr-Acr-Cht (top) and Gr, Gnn, Gr-Gnn-Cht (bottom)

3.4.2.2 Analysis by Powder X-Ray Diffraction (PXRD) and Scanning Electron Microscopy (SEM)

XRD patterns of un-modified graphene and chitosan, respectively, are shown in Figure 3.8 with diffraction peaks at 26.8^{o} (002), 44.2^{o} (004), and 10.8^{o} (002), 20.40^{o} (110) with a broad shoulder between 30-40^{o}. Characteristic peaks of chitosan (weak) were observed at 18.3^{o} for GP-Chr-Cht (blue), 9.7^{o} and 19.1^{o} for GP-Acr-Cht (green) and 18.5^{o} for GP-Gnn-Cht (purple) confirming presence of chitosan in the hybrid. Only one additional peak at 9.5^{o} in GP-Gnn-Cht was observed, probably due to presence of guanine (chromophore).

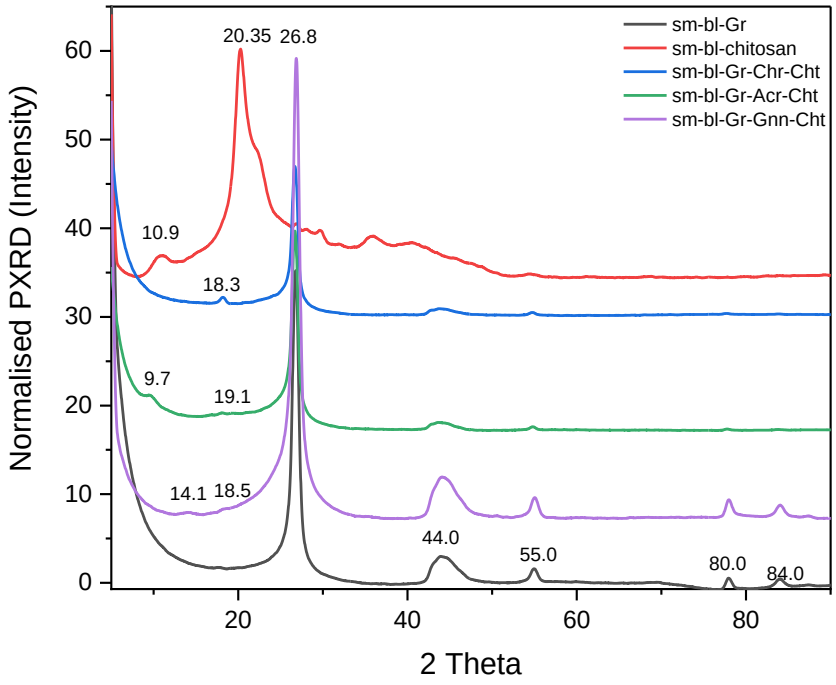

Figure 3.8: PXRD spectra of chitosan (red), graphene (black), Gr-Chr-Cht (blue), Gr-Acr-Cht (green) and Gr-Gnn-Cht (violet) composites

Figure 3.9 (left) displays SEM images of Gr-Chr-Cht prepared by one-pot method, it shows a dense packing of the material comparing to a fluffier graphene (Figure 3.4). The flakes of graphene are visible and evenly covered by chitosan. This may be due to the covalent interaction of the two reacting components on the graphene surface, and/or may be due to interfacial reaction between the anionic chromone and cationic chitosan.

Figure 3.9 (right) shows SEM images of Gr-Acr-Cht produced in one-pot reaction with a lump like solid structure. The images show similarity with Gr-Chr-Cht samples (Figure 3.9 left) regarding a distribution of the solid material covering graphene flakes. Figure 3.9 (bottom) shows a lump-like structure of the material with a denser packing than the pristine graphene. The graphene flakes are visible, but they are smaller compared to those of Gr-Chr- Cht and Gr-Acr-Cht. The image shows less distribution of smaller solid particles covering the flakes. This may be due to a repulsive force between the positively

charged chitosan and guanine molecules.

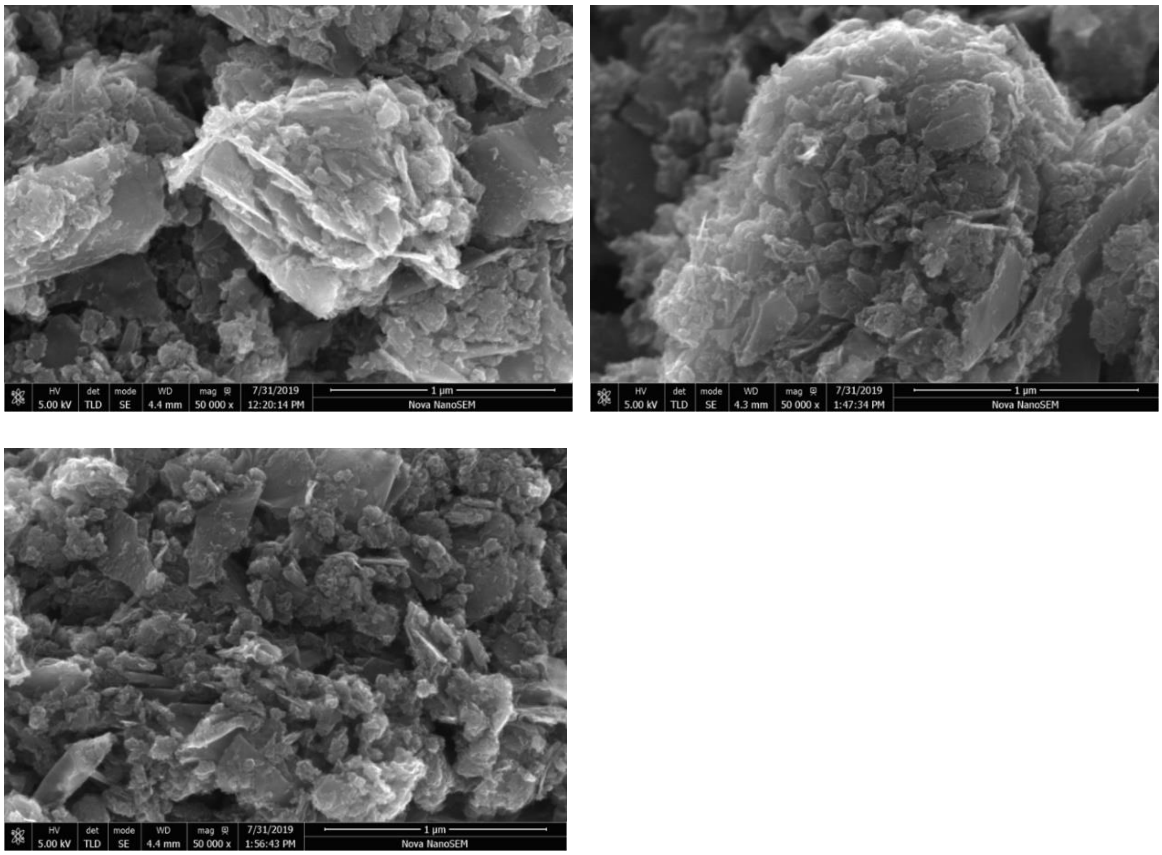

Figure 3.9: SEM Images of (top left) GP-Chr-Cht, (top right) GP-Acr-Cht and (bottom) GP-Gnn-Cht prepared by radical chemistry

3.4.2.3 Thermogravimetric Analysis (TGA)

Figure 3.10 (left) represents TGA thermograms for graphene and modified graphene in three component system. Figure 3.10 (right) displays normalized 1st derivatives of TGA for the composites and the respective graphene. In both modified and unmodified graphene samples, the initial loss of 2-5.5% is due to a loss of moisture between 0-48^{o}C. A complete pyrolysis is achieved by 637^{o}C for unmodified graphene. In the GP-Chr-Cht, a mass loss of 4.9%, 33.9% and 60.5% have been recorded between 0-42^{o}C, 42-612^{o}C, 612-800^{o}C, respectively. GP-Acr-Cht has a mass loss of 5.5%, 63.9%, 10% and 20.1% between 0-

91°C, 91-594°C, 594-646°C and 646-800°C, respectively. While 5.5% and 92.6% mass loss were observed between 0-91°C and 91-663°C for GP-Gnn-Cht sample.

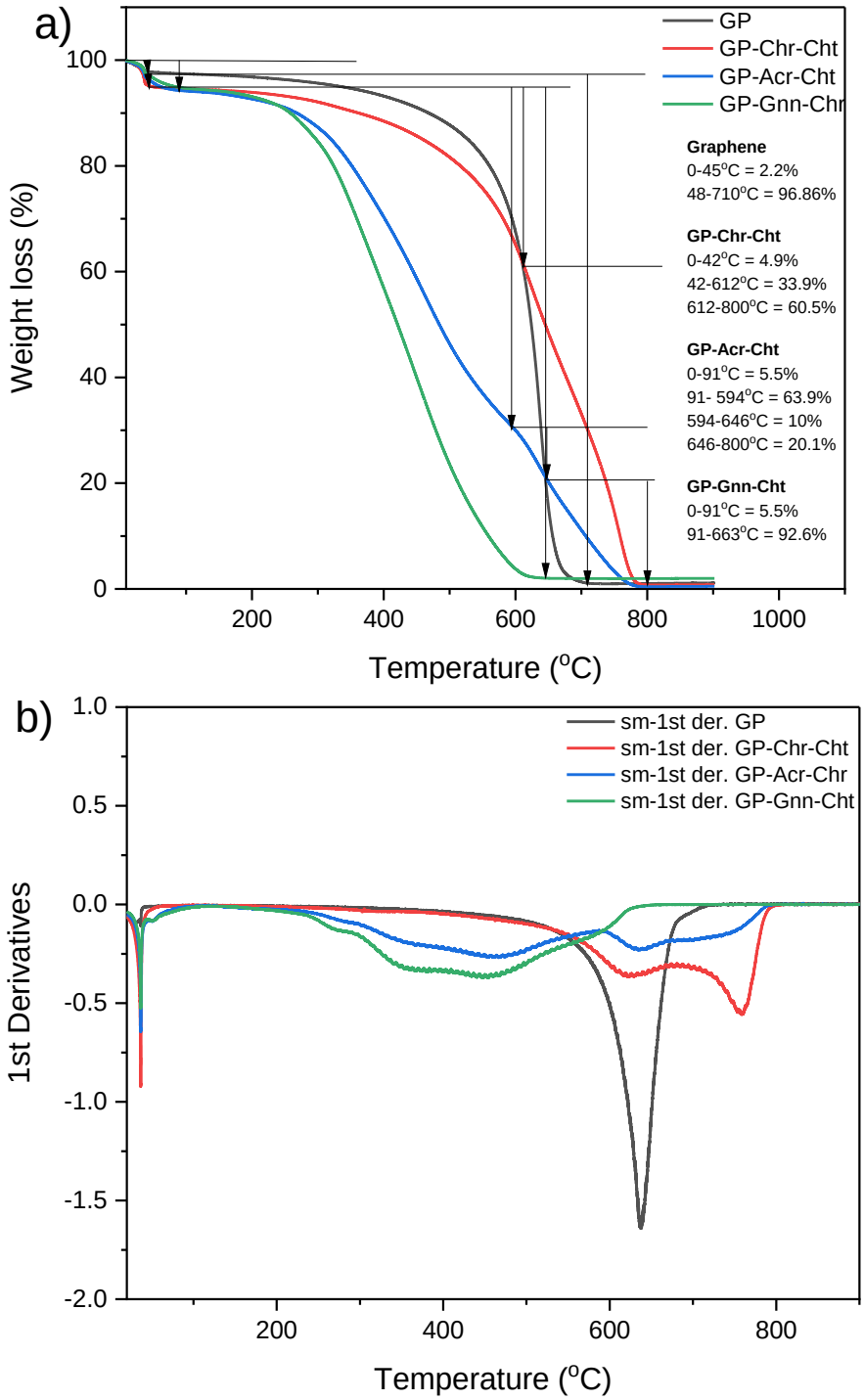

Figure 3.10: (a) Weight loss (%) against temperature and (b) normalized 1st derivatives thermogravimetric analysis of graphene (black), GP-Chr-Cht composite (red), GP-Acr-Cht composite (blue) and GP-Gnn-Cht (green)

After the initial loss of moisture and adsorbed air between 0-50^{o}C, the first derivative of unmodified graphene shows only one significant region with the inflection temperature of 637^{o}C. The degradation pattern of the two modified graphene GP-Chr-Cht (red) and GP-Acr-Cht (blue) prepared by radical functionalisation is similar. Three-component systems have two key regions at (T_i) 637 ^{o}C (both samples), which is similar to graphene. The second peak is observed at 738 ^{o}C for GP-Chr-Cht and 758 ^{o}C for GP-Acr-Cht; they can be attributed to further pyrolysis of graphene stacks and organic residue. GP-Gnn-Cht (green) has a peak at (T_i) 270 ^{o}C, 350 ^{o}C and 456 ^{o}C and shoulder at (T_i) 587^{o}C. This can indicate that the modification led to a high number of the defected graphene sheets, which degrade at lower temperature than graphene itself; additionally, an increased dispersibility due to synergistic effect of both chitosan and guanine prevents agglomeration of graphene sheets into larger stacks (graphite), which also lowers the overall temperature of degradation. Table 3.2 provides the summary of the TGA and BET results.

Table 3.2: Summary of BET data of two-component system and TGA values recorded at two key temperatures (T_1 and T_2) regions.

Sample	**SSA (m^2/g)**	**T_1 (^{o}C)**	**Weight loss (%) at T_1**	**T_2 (^{o}C)**	**Weight loss (%) at T_2**
Graphene	430.16	-	-	710	96.86
GP-Chr-Cht	135.66	612	38.8	800	60.5
GP-Acr-Cht	148.11	646	79.4	800	20.1
GP-Gnn-Cht	188.18	-	-	663	98.1
GP-ArCO-NHCht	230.01	630	58.1	726	41.0

3.4.3 Three-component system: Graphene-Linker-Chitosan (Gr-ArCO-Cht)

An alternative method for chitosan attachment to the graphene surface through condensation (amidation and esterification) reaction was studied. Here, two step method was developed: (1) the incorporation of the linker bearing carboxylic group by radical chemistry and (2) amidation, and esterification reactions between $-NH_2$ and -OH groups of chitosan and carboxylic acid of graphene. (Figure 3.11). This method was designed to replace the use of GO which is expensive.

The reactivity order of the three functional groups contained in the chitosan are as follows: $-NH_2$ > secondary OH > primary OH. Therefore, two types of reactions might be expected to happen: amidation and esterification reactions to yield graphene-benzamyl-chitosan or graphene-benzoyl-chitosan or both.

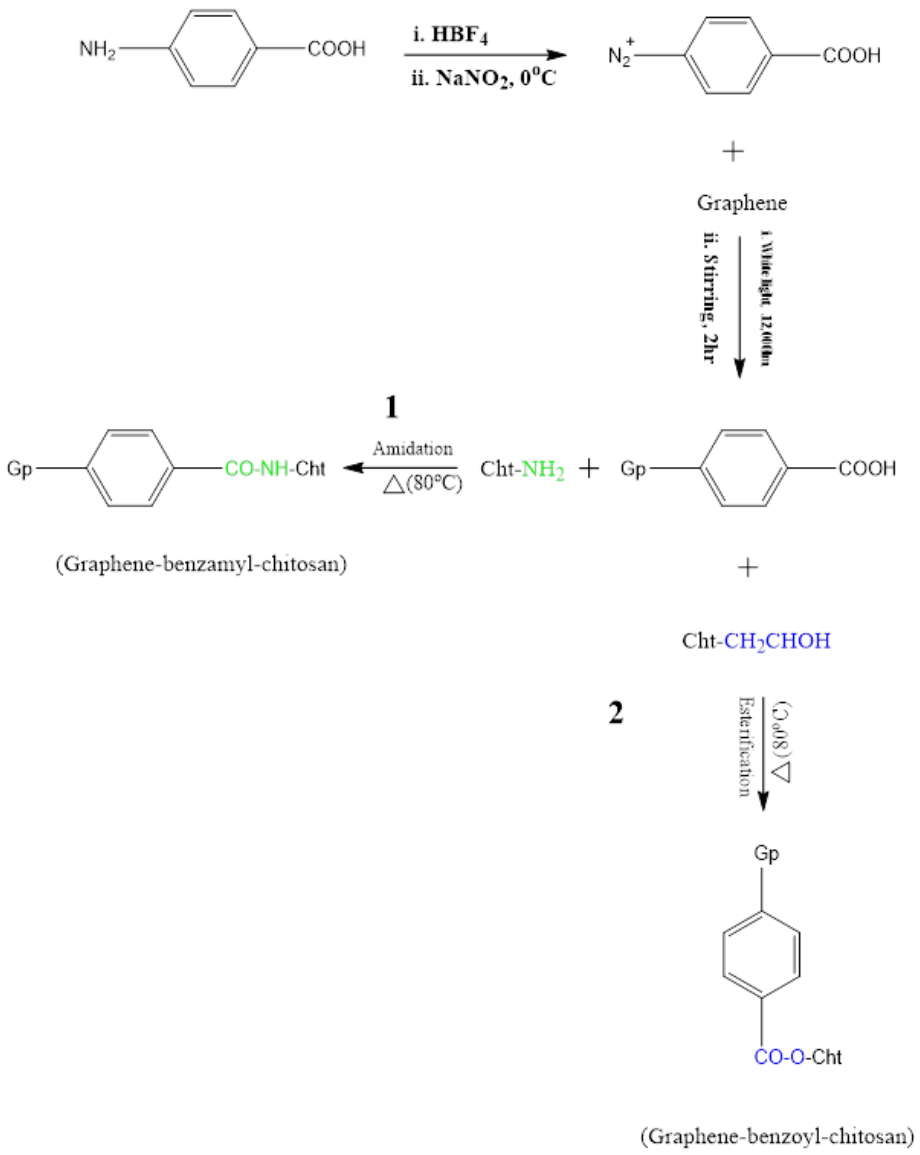

Figure 3.11: Preparation of graphene-benzamyl-chitosan and graphene-benzoyl-chitosan material via two step approach

3.4.3.1 Analysis by Fourier Transform Infrared Spectroscopy (FTIR) and UV-Vis Absorption Spectroscopy

Figure 3.12 represents the spectra of pristine graphene (black) and modified graphene with aryl carboxylic acid (red). A band at 1669cm^{-1} (C-O bending in acid) was observed in the modified graphene, which is stronger peak than in the unmodified graphene. Key peaks indicating successful modification between the linker and chitosan include: 1170cm^{-1} as C-O stretching in ester and 3638cm^{-1} as O-H and N-H stretching. Also, characteristic peaks (weak) of chitosan were observed at 1670cm^{-1} (N-H bending in amine), 1424cm^{-1}

(O-H bending in alcohol and C-H bending in alkane), and 1097 cm^{-1} (C-O stretching of primary alcohol). These bands can also indicate a post-modification product: 1670cm^{-1} as C=O stretching of primary amide, indicating the presence of both bending and stretching vibrations C=O due to amide group presence.

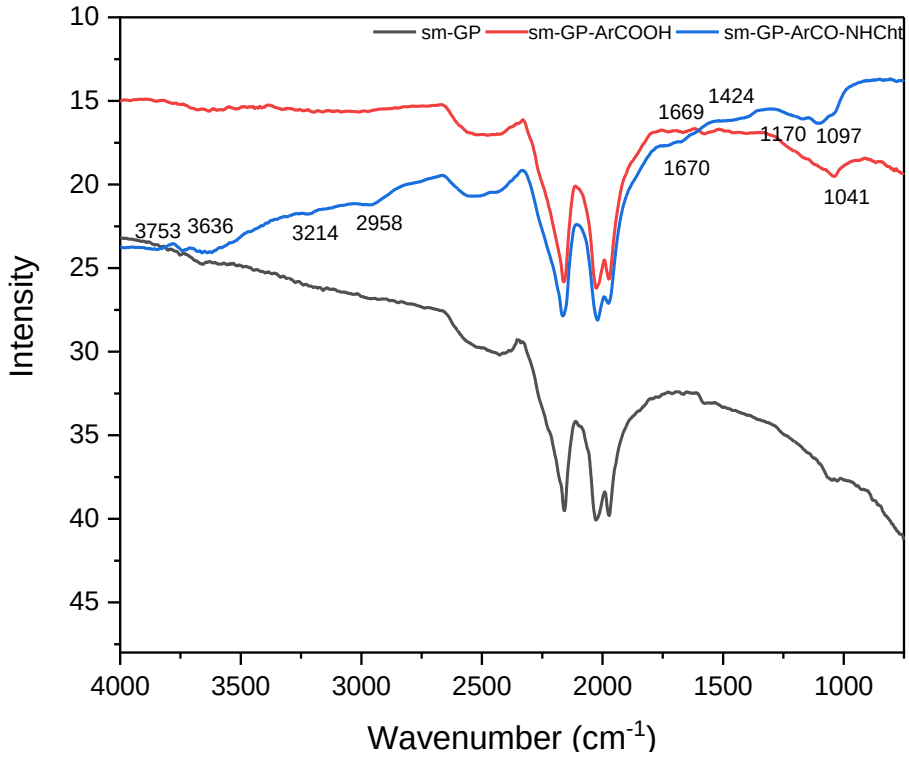

Figure 3.12: FTIR spectra of pristine graphene (black), GP-ArCOOH (red) and GP-ArCO-NHCht (blue).

Optical properties of the GP, GP-ArCOOH and GP-ArCO-NHCht are summarised in Figure 3.13. UV-Vis spectra show significant improvement in the modified graphene with stronger absorption bands at 270 nm compared to unmodified graphene, confirming functionalisation. A high background absorption was observed in the red spectra (GP-ArCOOH) which is likely due to scattering of light by the large chunks of graphene platelets due to low dispersibility, while a lower absorption background was observed in the blue spectra due a stabilisation caused by the chitosan incorporation. A new

absorption band (weak) was observed at 340 nm of the blue spectra probably due to the introduction of chitosan.

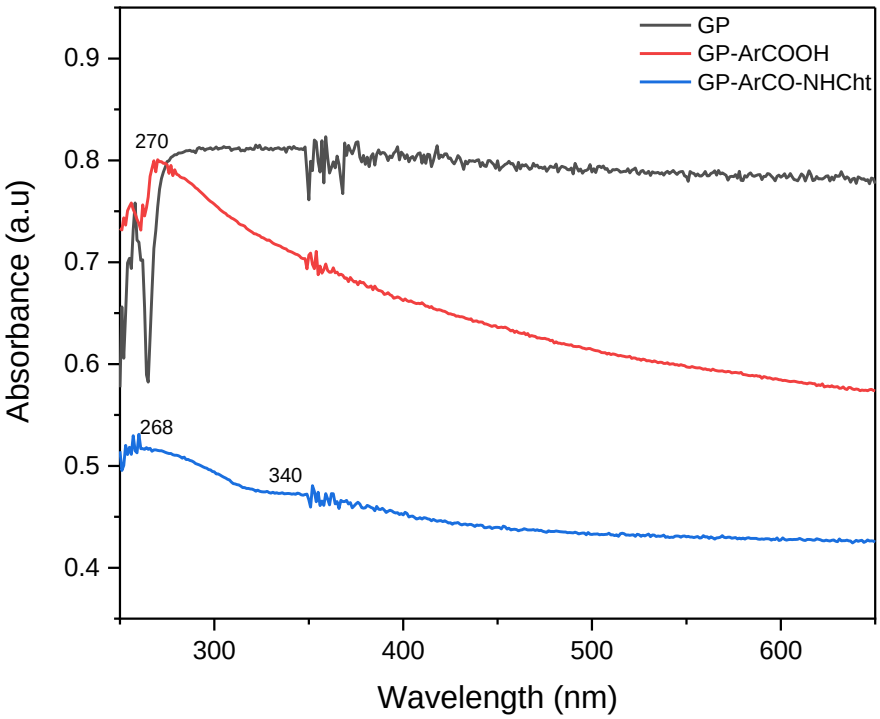

Figure 3.13: UV-Vis spectra of pristine graphene (black), GP-ArCOOH (red) and GP-ArCO-NHCht (blue)

3.4.3.2 Analysis by Powder X-Ray Diffraction (PXRD) and Scanning Electron Microscopy (SEM)

Figure 3.14 below represents the XRD spectra of pristine graphene (black) and the modified graphene with benzoic acid by electron transfer (red). Additional peaks were observed at 18.3^{o} and 87.4^{o} in the modified graphene, a characteristic of the benzoic acid. A characteristic peak of chitosan was observed at 21.21^{o} in the blue spectra, representing GP-ArCO-NHCht.

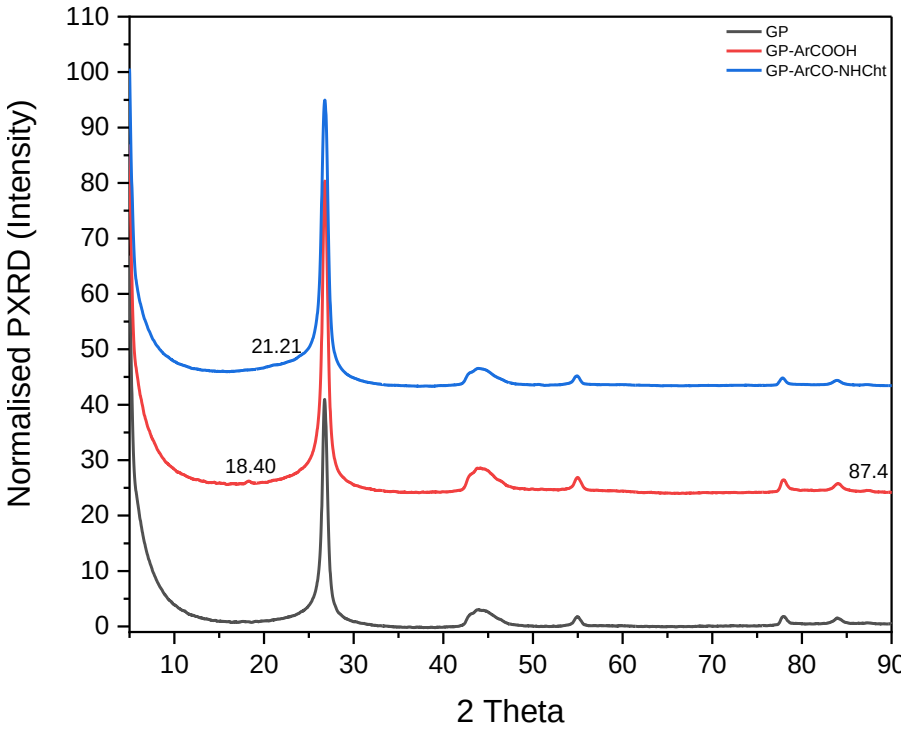

Figure 3.14: PXRD spectra of pristine graphene (black), GP-ArCOOH (red) and GP-ArCO-NHCht (blue)

Figure 3.15 show SEM images of the modified graphene with ArCOOH (left) and GP-ArCO-NHCht (right). The images indicate no visual changes in the material upon modification with chitosan.

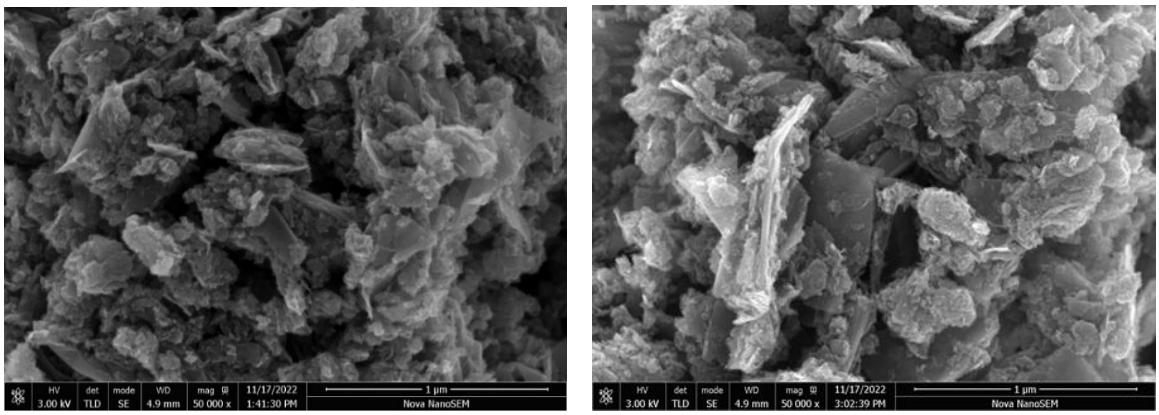

Figure 3.15: SEM images of GP-ArCOOH (left) and GP-ArCO-NHCht (right).

3.4.2.3 Thermogravimetric Analysis (TGA)

Figure 3.16 (left) represents TGA thermograms for graphene and modified graphene in two and three component system via covalent bonding and through a linking group.

Figure 3.16 (right) is normalized 1st derivatives of TGA for the composites and the respective graphene. Like other samples, the initial weight loss of 2-5% due to moisture between 0-48^{o}C was observed for modified graphene samples. A complete pyrolysis is achieved by 710^{o}C for unmodified graphene. A mass loss of 4.9%, 30%, 39.3% and 25.7% have been recorded between 0-45^{o}C, 45-605^{o}C, 605-727^{o}C and 727-788^{o}C respectively for the GP-ArCOOH. In GP-ArCO-Cht sample, the mass loss of 2.2%, 10.6%, 45.3% and 41.0% was recorded for 0-45^{o}C, 45-377^{o}C, 377-630^{o}C and 630-726^{o}C respective regions.

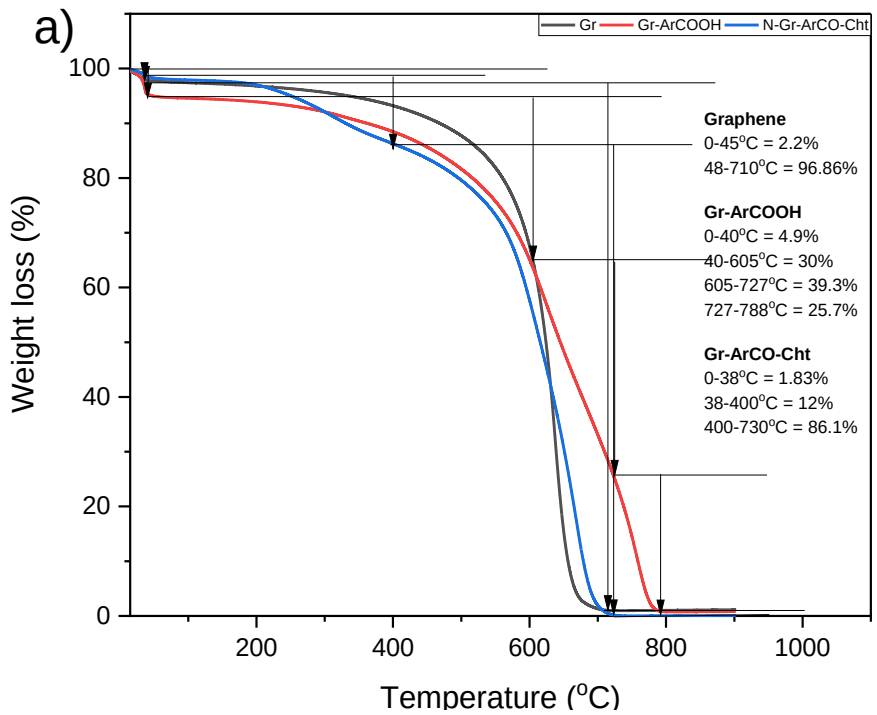

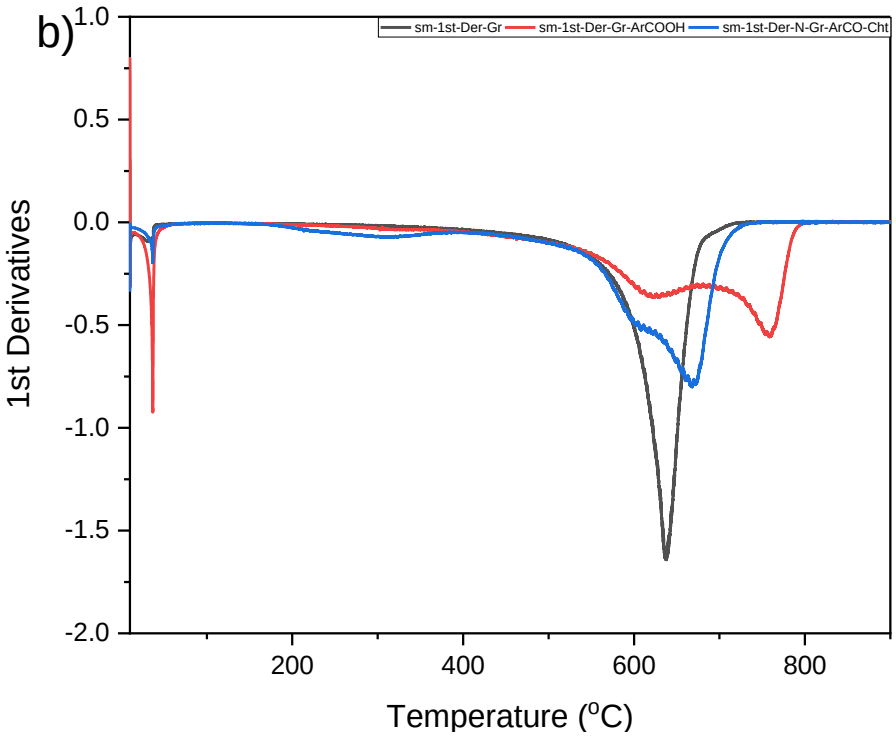

Figure 3.16: (a) Weight loss (%) against temperature and (b) normalized 1st derivatives thermogravimetric analysis of graphene (black), Gr-ArCOOH composite (red), Gr-ArCO-cht composite (blue)

Further analysis based on the 1st derivative of TGA shows only one significant region for graphene with the inflection temperature of 637°C. The degradation of the modified graphene GP-ArCOOH (red) has two significant temperatures: (T_i) 610°C (due to defected graphene) and (T_i) 760°C (due to aggregated graphene). Similarly, GP-ArCO-NHCht (blue) prepared in a two-step process reveals a broad peak at (T_i) 303°C due to chitosan, a peak at (T_i) 603°C due to residual chitosan and defected graphene and a peak at (T_i) 668°C (aggregated graphene). A slight shift towards lower temperature from 610°C in GP-ArCOOH to 603°C for the pyrolysis of GP-ArCO-NHCht is likely due to the overlap between the processes of carbonisation of chitosan and pyrolysis of graphene, which occur in the similar temperature range. A lower temperature of the final stage (668°C) as opposed to 760°C in GP-ArCOOH is due to an improved dispersibility of graphene platelets and a reduced aggregation leading to smaller stacks. This is also confirmed in

directly by UV-Vis spectroscopy where a low background absorption is recorded indicating better dispersibility of the material in the solution.

3.5 Summary

Polymer (chitosan) and three different organic chromophores (acridine, chromone and guanine) have been used to modify graphitic surface. The chitosan was used in two and three component system in one pot and two-step methods. The in-situ method was done through physical mixture (ultrasonication) of graphene and chitosan, and covalent radical functionalisation of graphene with chitosan and graphene with chitosan and dyes. The two-step method involved covalent functionalisation of graphene with ArCOOH followed by dispersing chitosan into the solution of Gr-ArCOOH and heated to 80^{o}C for 3hrs under stirring. FTIR was used to identify differences in the functionality of the materials before and after functionalisation. UV-Vis absorption and fluorescence spectroscopy analyses provided details about optical properties of the samples. PXRD, TGA, and BET were used to observe the extent of graphene functionalisation.

3.6 Conclusions

Two and three component systems were successfully synthesised via *in-situ* method of covalent radical functionalisation and non-covalent reaction method with graphene to enhance the adsorption capabilities of both graphene and chitosan as composite in two component system and also create multifunctionality in three component system leverage on the adsorption properties of graphene and chitosan and light harvesting property of the dyes. Different functionalization methods have been designed to create a simple and most effective catalysts for the removal of organic waste. FTIR analysis of all samples modified using radical functionalisation show enhanced signals corresponding to the product formation. Other additional characteristic peaks of chitosan and linking groups in both

covalent and non-covalent reaction products have been identified. Optical properties of the samples demonstrated a change in their absorption capacity and improved solution stability as a result of chitosan incorporation. All samples revealed shift towards UV region, only GP-Acr- Cht has absorption in visible region of the spectrum at 405 and 428 nm.

Important changes were detected in the graphitic surface of the modified graphene using PXRD, BET and TGA analysis. In the case of three component systems, PXRD analysis shows additional peaks between 9-22^{o} due to chitosan and chromophore molecules. BET results support the substantial alteration of the graphitic surface as the values differ between the samples indicating a various degree of modification within the new products with the three-component systems having lower values. The decreasing order of BET surface is as follows: GP-ArCOOH > GP-Cht (PM) > GP-Cht (CM) > GP-Gnn-Cht > GP-Acr-Cht > GP-Chr-Cht. The TGA analysis of the two and three component system shows a substantial alteration in the modified samples. Results show the complete pyrolysis of unmodified graphene at 637^{o}C. All modified samples except GP-Gnn-Cht, have two key regions of the greatest change of the weight loss with the inflection temperatures above 550^{o}C corresponding to the pyrolysis of graphene matrix. The low temperature region can be associated with the weight loss attributed to the defected graphene, which contains sp_3-hybridised carbon defects due to covalent modification. The high temperature region is associated with the pyrolysis of aggregated graphene sheets as seen in graphite. The results in GP-Gnn-Cht sample indicate a substantial number of graphene layers have been successfully functionalised by one-pot radical covalent method producing larger number of defected graphene lowering the temperature of pyrolysis. Additionally, a better dispersibility is achieved preventing aggregation of graphene sheets in a stack.

Covalent modification of GO with chitosan have been reported by researchers, but to the best of our knowledge, no work was reported on the covalent radical functionalisation of chitosan on graphene.

CHAPTER 4

4.0 Physisorption and Photocatalytic Study

4.1 Abstract

Scarcity of clean and safe drinking water due to industrial and environmental pollution is a major source of concern, and its adverse effects on human health and aquatic life cannot be overemphasised. Dye industries are part of the major contributors to water pollution globally, and some of the dyestuffs which are being channelled directly to the water sources untreated, are carcinogenic, toxic and non-biodegradable. These contaminants affect the quality of water by changing these parameters: chemical oxygen demand (COD), biochemical oxygen demand (BOD), pH, colour and salinity. Hence, the need to develop a green, cost-effective and efficient technology that has the capability of removing dyestuff from wastewater.

This chapter aims at evaluating traditional and advance methods such as adsorption, photodegradation respectively to study the dye removal using three model dyes: Methylene Blue (MB) as a cationic dye, Methyl Orange (MO) as a basic dye and Rhodamine B (RhB) as a photostable cationic dye.

Objectives of this research are to determine the optimal mass concentration of the catalysts and the dye models, and to conduct adsorption-desorption (physisorption) experiment, kinetics studies of the catalysts using the three model dyes under dark and light illumination for 120 min and neutral condition. And finally to conduct mechanistic study of the photodegradation process.

4.2 Heterogeneous Photocatalysis

Catalysts are substances used to accelerate the kinetics of a chemical reaction by a physical, chemical or biological means. Catalysis refers to the process of accelerating the chemical reaction by the catalyst. Photocatalysis is a branch of catalysis, and a process by which light (photo) ignites a chemical reaction. To degrade organic pollutants efficiently (including toxic compounds with low biodegradability) under ambient conditions, photon, rather than thermal energy is best source of renewable energy to be employed [2, 30]. The main supply of energy on the surface of the Earth, which by far, is larger than any source of energy is solar energy (about 25,000 – 75,000/hectare/day) [41]. Solar energy is a form of renewable energy that has not been widely utilized for human consumption [30, 41]. Utilization of sunlight to initiate chemical reaction of organic pollutants requires a photochemical system through which the energy enters by the absorption of light with a certain wavelength of one of the components; organic species and the photocatalyst [2].

Heterogeneous photocatalysis has become an interesting area of research in the past decades due its applicability in various media, i.e, gas phase, aqueous solution and pure organic liquid phase [29], and their great applications in areas, including water and air treatments, cancer therapy, heat transfer and heat dissipation, anticorrosion, solar chemicals production to name a few [3, 30]. Photocatalytic degradation is an important advanced oxidation process (AOP) technology that can degrade organic pollutants [29, 37, 42]. It is a sophisticated method for the mineralization of highly stable organic compounds such as pesticides, phenolic wastes, dyes, pigments and some inorganic pollutants which are difficult to degrade [37]. Photon energy activates the catalyst through absorption of light of a specific wavelength by the material [2]. A resulted electron–hole pair can promote a formation of the reactive oxygen species (ROS) in the aerated system or directly interact with an organic substrate[2, 43 ,44] in the (photo)-chemical processes to create or degrade

specific compounds [3]. Processes involved in heterogeneous (photo)catalysis can be broken down into five stages: (1) transfer of reactants from mobile phase (liquid or gas) to the surface, (2) adsorption of at least one reactant by the surface, (3) photoreaction in the adsorbed phase, (4) desorption of the products from the surface, (5) removal of the products from the interface region[2,3,29].

Unlike other conventional methods of water and air purifications that utilize e.g. chlorine and its derivatives, ozone, hydrogen peroxide, perozone, potassium permanganate, Fenton's reagents, chemical oxidations which may yield toxic side- products and be expensive [45, 46]. In contrast, the photocatalytic products such as CO_2, H_2O and NH_3 were proved to be non-toxic and cost effective [37]. However, despite the efficiency of some photocatalysts, the kinetics for their photochemical reaction is influenced by some physical parameters, including mass of the catalyst, temperature, pH, wavelength, initial concentration, aeration.

4.3 Examples of Multicomponent Heterogeneous Photocatalytic Systems

Rajamanickam and Shanthi [85] reported the degradation of 4-nitrophenol by ZnO assisted photocatalysis in aqueous dispersion under solar light irradiation. Adsorption of the organic pollutant on ZnO at pH 5, was found to be favourable by the Langmuir approach. However, a steady increase in the initial concentration of the catalyst decreased the degradation rate, while enhanced degradation was only achieved at optimum concentrations of the oxidants such as H_2O_2, $K_2S_20_3$ and $KBrO_3$. Raizada *et al* [46] reported a successful grafting of ZnO-activated carbon (ZnO-AC) and ZnO-brick grain particle (ZnO-BGC) photocatalysts and tested to have superior photocatalytic activity on Malachite Green (MG) and Congo Red (CR) due to improved adsorption capability. Rate of decolorization was higher during simultaneous adsorption and photoactivity process. ZnO-

AC/A+P process, was found to be most efficient for the photodegradation of MG and CR. Dariani *et al* [86] reported the photodegradation activity of nano TiO_2 of various particle sizes on MB in aqueous solution under UV illumination. UV Irradiated amorphous TiO_2 (UVA/TiO_2) activity was found to be technically feasible under adequate and proper experimental conditions. Degradation of up to 90% was achieved in 1 hour with 10nm TiO_2 nanoparticles. Lin *et al* [87] reported the fabrication of ZnO-SnO nanocomposites using simple coprecipitation method. The composite was formed by co-precipitation method. The composite was found to exhibit a superior photocatalytic property than the corresponding ZnO. Results showed 40% of the full degradation of MB and oxidizing the remaining 60% to smaller molecular weight compounds such as malonic and propionic acids. The efficiency of the composite was proven to be high after several treatments. Tammina *et al* [88] made a first ever report on the ascorbic acid mediated synthesis of SnO_2 nanoparticles with three different sizes and their catalytic activity on MB dye. All three nano catalysts vary in particle sizes and band gap energies and have shown promising photocatalytic activity under UV irradiation, although they exhibited varied degradation rates. Khatee *et al* [47] reported on the influence of chemical structure of organic dyes on the photocatalytic degradation efficiency of TiO_2 nanoparticles. Results showed that the photodegradation rate of monoazo dyes is higher than those with anthraquinone structure. Chloro and methyl groups in the dyes slightly decrease efficiency, while nitro group in the dye enhances photodegradation efficiency. The presence of multiple sulfonic groups slows down the process, while hydroxy groups intensify the resonance of electrons in the molecule and increase photodegradation rate. Similarly, side groups such as alkyls decrease the solubility of the molecules in the aqueous media and the degradation process is not favoured.

4.4 Physisorption and Chemisorption

Adsorption plays a key role in heterogeneous (photo)catalysis as it is an essential step of the interaction between the catalyst and the reactant. There are two adsorption processes, which are based on weak (physisorption) and strong (chemisorption) interactions between the components.

Physisorption can be referred as the physical adhesion or adsorption of a substance (adsorbate) on the surface of a material (adsorbent) through van der Waal's forces, which are weak electrostatic interactions e.g. dipole-dipole, induced dipole-dipole and London forces. Typical energy gain for these interaction lies 3-10 kcal/mol.

In contrast, chemisorption is defined by strong electronic interactions between the adsorbate and adsorbent leading to the formation of chemical bonding. Energies of chemisorption lie within 20-100 kcal/mol. There are two types of chemisorption, namely, *molecular adsorption* (adsorbate remains intact) and *dissociation adsorption* (one or more bonds in adsorbate break upon adsorption).

Fractional coverage (q) is a definition to describe the extend of surface coverage, and is expressed as follows:

$$\theta = \frac{number\ of\ adsorption\ sites\ occupied}{number\ of\ adsorption\ sites\ available} \quad or \quad \theta = \frac{V}{V_{\infty}}$$

Fractional coverage can also be calculated based on adsorbate adsorbed, where *V* is the volume of adsorbate and *V* is the volume corresponding to adsorbate's complete monolayer.

4.5 Models of Adsorption and Adsorption Isotherms

To study properties of adsorbent (surface), semi-empirical *adsorption isotherm* is usually employed. It describes the variation of *fractional coverage* with pressure, when considering interaction of molecules with the surface in gas phase. *Adsorption isotherm model* is based on the following assumptions:

- the surface is considered homogeneous (or binding is to only one type of reactive site)
- all reactive sites are energetically equivalent, and the energy of adsorption is the same across the surface
- adsorption is limited to monolayer coverage (only one molecule per site)
- there is no interaction between adsorbed molecules meaning the adsorption is independent from adjacent occupied sites.

These assumptions form the basis of the **Langmuir Isotherm**. However, co-adsorption can take place, when initially adsorbed molecular layer can act as a new surface (adsorbent). In this case, adsorption isotherm will not level up but will continue to rise indefinitely. **Brunauer-Emmett-Teller (BET) Isotherm** is most popular model, which deals with multilayer adsorption. Here, the surface is covered by randomised reactive sites, which are empty or occupied with mono or multilayer adsorbed molecules.

4.6 Adsorption Kinetics to Study Dye Removal

The adsorption capacity (q_t) or loading of adsorbate (dye) on the adsorbent (surface) is calculated as follows:

$$q_t = \frac{V(C_0 - C_t)}{m} \quad or \quad q_t = \frac{(C_0 - C_t)}{C_s}$$

Where V is the solution volume (L), C_0 is the initial adsorbate concentration (M or mg per L), C_t is the dye concentration in the solution at any given time (t) (M or mg per L), and m is the adsorbent mass (g). Alternatively, C_s is the concentration of adsorbent (*g per L*).

Langmuir isotherm is assumed being a reversible process between surface (adsorbent) and molecules (adsorbate) [260].Thus typically, the adsorption kinetics is studied through either the pseudo-first order [89] or pseudo-second order [90] equations as they can fit a wide range of adsorption systems.

The varied reaction order of adsorption proposed by Liu and Shen [261] can be expressed as follows:

$$\frac{dq_t}{dt} = k_1(q_e - q_t) + k_2(q_e - q_t)^2$$

$$k_1 = [k_a(C_0 - q_{max}X) + 2k_a k_d(C_0 - q_{max}X) + k_d^2]^{\frac{1}{2}} \quad and \quad k_2 = k_1 q_{max} X$$

where q_{max} is the maximum adsorption capacity of the adsorbent, k_a and k_d are the corresponding adsorption and desorption rate constants and X is the adsorbent dosage.

In the case of $q_e = k_1/k_2$, first order kinetics can be used to describe the process, if this condition cannot be met, second order rate expression is considered.

Pseudo-First-Order Kinetics equations can be expressed as follows:

$$\frac{dC}{dt} = -k_1 C_t \quad or \quad C_t = C_0 e^{-k_1 t}$$

Number of molecules adsorbed (q_t) at any given time (t) is calculated as follows:

$$q_t = q_e(1 - e^{-k_1 t}), \ where \ \ q_e = \frac{V(C_0 - C_e)}{m}$$

where V is the volume of dye solution, C_0 is the initial dye concentration, C_t is the dye concentration in the solution at a given time (t), and m is the adsorbent mass, k_1 is a rate

constant and q_e is the amount of dye adsorbed at equilibrium.

Pseudo-second-order kinetics is described through the following equations:

$$\frac{dC}{dt} = -k_1 {C_t}^2 \quad or \quad \frac{1}{C_t} - \frac{1}{C_0} = k_1 t$$

Thus, the number of molecules adsorbed (q_t) at any given time (t) is calculated as follows:

$$q_t = q_e \left(\frac{C_0 k_1 t}{1 + C_0 t}\right) = \frac{q_e k_2 t}{1 + q_e k_2 t} \qquad and \qquad \frac{dq_t}{dt} = k_2 (q_e - q_t)^2$$

Although these are popular and well-studied models, which can fit a variety of adsorbent-adsorbate systems, they have some implications and pitfalls. [260]

4.7 Organic Dyes as Colorants

Unlike most organic compounds, dyes possess colour because they absorb light in Theory of colour and its chemical constituents dated back to 1868 by Graebe and Liebermanm who stated that colour was associated with unsaturation because, all known dyes decolourised on reduction. In 1876, Witt expanded this postulation by stating that all coloured organic compounds must possess a group which is responsible for imparting colour i.e. chromophores. This theory plays a significant role in the synthesis of organic dyes that resulted in the discovery of thousands of them and the promising ones been manufactured. This discovery had opened the door for many other theories to emerge, but none of them had explained how colour generates in organic compounds. The discovery of the interaction between electromagnetic radiation in the UV and visible regions with organic compounds provides an explanation about colour formation in organic compounds. When photon is absorbed by the ground state of the compound its energy is causing one or more electrons promoted to the next available orbital called the excited state through a transition between the two energy states[103-105].

4.7.1 Dyes as Model Systems to Study Environmental Pollution

Colorants are considered robust organic pollutants that are difficult to degrade. Therefore, they are employed as environmental models to study appropriate removal methods through kinetics of their degradability. Most common and challenging contaminants include basic, cationic and photostable dyes. The strategy to remove such chemicals can include both adsorption, which is based on appropriate electrostatic interactions (based on their charge) and mineralisation process e.g. (photo)catalysis. In this chapter, methylene blue (MB), methyl orange (MO) and rhodamine B were chosen as model compounds as they represent dyes that can also be mineralise through photocatalysis [29].

Methylene Blue. Methylene blue (MB, Figure 4.1) or methyl thioninium chloride is an aromatic heterocyclic dye[215,216] with a molecular weight of 319.85 g mol^{-1} [218, 219], molecular formula, $C_{16}H_{18}N_3ClS$ and IUPAC name [3,7-bis(dimethylamino) phenothiazin-5-ium chloride] [212, 221,223].

Figure 4.1: The model and structure methylene blue (MB) copied from Ref. (214)

It is a blue cationic and primary thiazine dye which absorbs light in both visible and ultraviolet regions with the wavelength of maximum absorption (λ_{max}) at 664 nm and 292 nm[213,216,243], respectively. It is classified under polymethine dye with an amino auxochrome

unit and is a positively charged compound. It consists of three mesomeric structures with positive charge on either nitrogen atom (amine group) or on sulphur atom. The reduced forms of MB, leuco-methylene blue (λ_{max} 256 nm and 322 nm) and MBH_2^+ (λ_{max} 232 nm) are colourless and stable in aqueous solution [216]. MB is blue in oxidized state [220] and transformed to leuco / colourless forms by reducing agents.

It was first synthesised by a German chemist Heinrich Caro in 1876 and used for the treatment malaria. This opened door for its application in medical, biological and pharmaceutical areas. It's a readily soluble in water and other organic solvents such as methanol, 2-propanol, ethanol, acetone and ethyl acetate, and can be used as a redox indicator. Methylene blue is a versatile compound which has wide range of applications[225] in textiles, paper, food, medical, chemical, pharmaceutical and aquacultural sectors etc. The commercial demand of MB is enormous, as all these important industries hugely rely on it increasing the rate of its production. It is considered one of the most popular clothing colourants[226] and the most common dye in the textile industry[227]. However, the carcinogenic nature of MB vis a vis it's non-biodegradability in water is a source of concern.

MB is often employed in photodegradation and adsorption studies as model compound. The spectrophotometric analysis provides key information including the form of the dye and its stability in the medium. The absorption spectrum of the MB shows the most intense absorption peak at around 664 nm associated with an MB monomer, with a shoulder peak at about 612 nm attributed to MB dimer. An additional two bands appear in the ultraviolet region with peaks around 292 nm and 245 nm associated with substituted benzene rings which gradually decrease as the photodegradation reaction proceeds[212].

Toxicity of Methylene Blue. MB discharged into water bodies above a certain concentration is harmful to human health due to its substantial toxicity [212, 228-229] and significant threat for water aesthetic. The *no-observed-adverse-effect level* (NOAEL) for the MB in rats was found to be 25 mg kg^{-1}, [238]. MB is toxic, carcinogenic, non-biodegradable and can cause a serious threat to human health and destructive effects on the environment[212-231]. Several health complications such as respiratory distress, mental, abdominal, blindness, and digestive disorders, cyanosis, shock, gastritis, jaundice, methemoglobinemia, nausea, diarrhoea, vomiting, tissue necrosis, and increased heart rate have been attributed to MB[232-237]. Presence of MB in water sources, even at low concentration, decreases light transmittance due to high molar absorption coefficient (~8.4 × 10^4 mol^{-1} cm^{-1} at 664 nm), decreases oxygen solubility, affects the photosynthetic activity of aquatic life, thus affects the food supply chain of the microorganisms and decreases the diversity and aesthetics of the biological community[239-240].

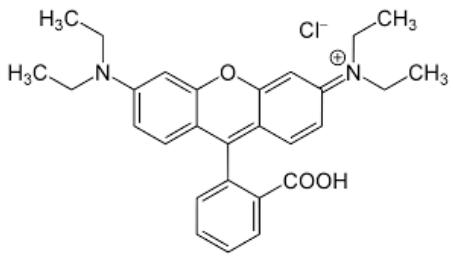

Figure 4.2: The model and structure Rhodamine B (RhB) copied from Ref. (262)

Rhodamine B. Rhodamine B (RhB, Figure 4.2) ($C_{28}H_{31}N_2O_3Cl$), mol. wt. 479[264], IUPAC name (9-(2-Carboxyphenyl)-6-(diethylamino)-N,N-diethyl-3H-xanthen-3-iminium chloride)[262-265] is known to be a brilliant pink synthetic azo-dye which has been broadly used in various industries such as cosmetics, foods, paints, textiles and leather [262] It's a highly water-soluble basic dye of the xanthene class[263] and has been extensively used for fluorescent labelling and food colouring due to its fastness, low cost, and stability. [265]

Toxicity of Rhodamine B. RhB has potential toxic effects and is an allergen affecting the human respiratory system, skin, and brain[264]. Both dermatological and toxicological investigations shows that long term exposure of Rhodamine B may cause several potential disorders in human beings such as cancer, birth deficiency, and irritation to eyes and skin[262]. The carcinogenicity, reproductive and developmental toxicity, neurotoxicity and chronic toxicity towards humans and animals have been experimentally proven.[263]

4.8 Materials and Methods

4.8.1 Preparation of the Stock Solutions of Dyes (pollutants) and Hybrids

Model Dyes: The stock solution of Methylene blue (M 319.85, 9.48×10^{-4} M) was prepared by dissolving 0.91 mg of the dye in 3 mL of deionised water. The stock solution of Methyl Orange (M 327.3, 9.37×10^{-4} M) was prepared by dissolving 0.92 mg of the dye in 3 mL of deionised water. The stock solution of Rhodamine B (M 479.02, 9.78×10^{-4} M) was prepared by dissolving 1.40 mg of the dye in 3 mL of deionised water.

Hybrids: Stock solutions of graphene and hybrids were prepared by dispersing 1 mg of a sample in a vial containing 1 mL of distilled water. The resulted dispersions were sonicated for 3 min to homogenise the hybrids in the solution.

4.8.2 Spectrophotometric Experiments

All spectrophotometric experiments to assess the photocatalytic and adsorption abilities of the materials were carried out using a Cary 50 UV-Vis spectrophotometer controlled at 20^{o}C by a single cell Peltier accessory, while mercury and xenon lamps were employed as the source of visible and UV light sources. Illumination of the samples was carried by Xenon lamp with adjustable radiation flux (0-150W). The spectral range of the lamp was

regulated by using appropriate cut-off optical filters for visible light. The electronic absorption spectra were recorded using a either Cary 50 or Carry 100 UV-vis scanning spectrophotometer.

4.8.3 Spectrophotometric Study of Dye Photostability

Two kinetic experiments were conducted under visible light with different irradiation times of 30 min and 120 min to determine the photostability of the dyes. The 30 min kinetics tests were carried out under basic, neutral and acidic conditions with 5 min intervals between scans; the 120 min kinetics tests were done under neutral conditions with 20 min intervals between scans. Figure 4.7 (a-c) in the appendix and Figure 4.5 (a) shows the plot of the aqueous solutions of 10% trifluoroacetic acid (TFA) and 1M NaOH prepared for acidic and basic conditions, respectively for the 30 min kinetics.

In brief, 3 quartz cuvettes containing 3 mL of distilled water were labelled A, B and N, indicating acidic, basic or neutral pH. And pH of the solutions was adjusted by adding 6 µL of 10 % TFA (acidic pH) and 15 µL of 1M NaOH (basic pH). Then, 0.05 mL of the stock solution of an appropriate dye was added into each quartz cuvette of an appropriate pH to ensure that optical transmission falls within acceptable range (0.7-1.0 Abs a.u.). The resulted dye solution was scanned immediately before being illuminated with visible light (using 420 nm cut-off filter) using tungsten lamp (75W). For the 120 min kinetics test, to a cuvette containing 3 mL water 0.05 mL of the stock solution of an appropriate dye was added, stirred and scanned the first minute before irradiating with visible light.

4.8.4 Preparation of Standardisation curve

Appropriate stock solutions of MB, MO and RhB were used for this experiment. A baseline scan of plastic cuvette containing 3 mL of distilled water was recorded in a UV-vis

spectrophotometer. This was followed by the addition of 10 µL of an appropriate dye and subsequent recording of the UV-vis spectrum; the 10 µL addition steps followed by a scan were repeated up until the total added dye volume reached 100 µL.

4.8.5 Determination of Optimal Loading of the Hybrids using MB as Dye Model

A range of aliquots of the hybrid stock solution (0.05, 0.075, 0.100, 0.125, 0.150, 0.175, 0.200 mL) was added into cuvettes containing 3 mL of distilled water. 20 min dark reaction was performed for all the samples using MB dye starting with the base line scan, followed by the addition of 30µL dye with continuous stirring and recording UV-vis spectrum at 5 min intervals. A uniform concentration of 0.1 mg/mL has been selected as optimal loadings for all the samples throughout the experiments.

4.8.6 Initial Catalyst Loading

0.100 µg/µL of each sample was added to cuvette containing 3 mL distilled water, followed by sequential addition of 10-100 µL MB, RhB, MO with continuous stirring to attain equilibrium. UV-Vis scan was recorded after addition of each 10 µL dyes in the sample.

4.8.7 Kinetic Study

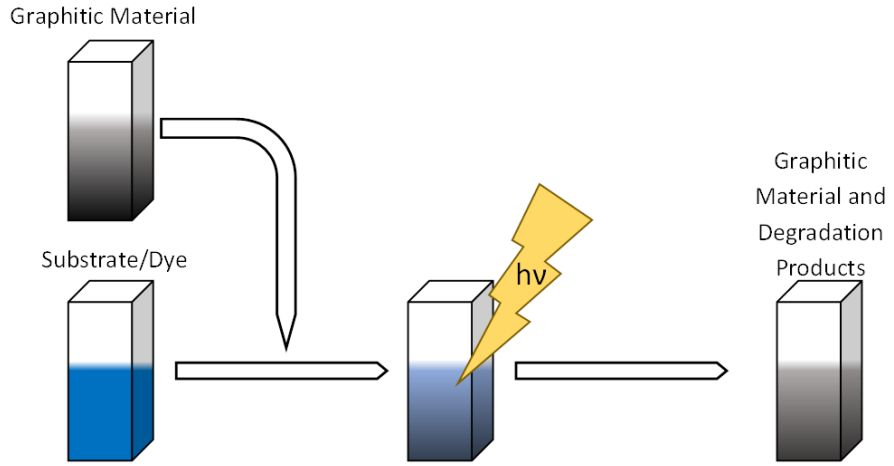

Figure 4.3: Illustration of (photo)degradation of dye models

Light and dark experiments (photoactivity and adsorption). Figure 4.3 illustrates a set-up used in this study to assess the removal of organic pollutants. Typically, 0.03 mL of a dye stock solution was added into a quartz cuvette containing 3 mL of distilled water to ensure that optical transmission falls within acceptable range (0.7-1.0 Abs a.u.) prior adding graphene materials. The solution was stirred to achieve homogeneity, and a UV-vis absorption spectrum was recorded and used as 0 min value (A_0). To the quartz cuvettes containing 0.1 mL of the appropriate catalyst (stock 1 mg/mL) in 3 mL of water, 0.05 mL of a dye stock solution was added and stirred for 1 min prior the first scan. A kinetics experiment was carried out for 120 min, by recording UV-vis spectra at 1 min, 20 min, 40 min, 60 min, 80 min, 100 min and 120 min. Dye removal efficiency was determined by plotting a graph of %RE against time (minute) using the formula below. The experiments were performed in triplicate and the mean values are reported.

$$\%Dye\ Removal = ((C_o - C) / C_o) \times 100$$

Where A_0 and A_t are the absorbances at 664 nm at t_0 = 0 min, and at various time points t = 1 min, 20 min, 40 min, 60 min, 80 min, 100 min and 120 min.

Desorption Study. After both the light and dark experiments, desorption study was conducted to determine the amount of physiosorbed dyes on the adsorbent. In addition to dilution factor (DF) was experimentally determined for MB.

Dilution Experiment. Deionized water (3 mL) was added to a cuvette to record a baseline. Then, 0.05 mL of MB (stock 0.08 mM) was added followed by a scan in the visible region 400-750 nm, and the absorbance of 0.84 a.u *(A_{MB})* was recorded at λ_{max} 665 nm. 1 mL of EtOH, a good desorbing agent, was added to the cuvette containing the MB

solution and stirred for up to 5 minutes. Absorbance of 0.71 a.u *($A_{MB+EtOH}$)* was recorded. The difference between the initial A_{MB} and final *($A_{MB+EtOH}$)* absorbance was referred to as the dilution factor *($DF = A_{MB} - A_{MB+EtOH}$)*. The difference of 0.13 equates to 15 % of dye loss. Thus, for each desorption experiment, 0.13 or 15% was considered as the dilution value, and the desorption values were corrected, accordingly.

Desorption Experiments. To a cuvette containing an appropriate sample from the dye removal study, 1 mL of EtOH was added. The solution was stirred for 5 min, and the absorbance ($A_{Desorbed\ Dye}$) was recorded. The desorption values were then corrected, accordingly with the dilution factor *DF* and total values were calculated: Total desorbed Dye = $A_{Desorbed\ Dye}$ + *DF*

4.9 Results and Discussion

To understand the behaviour of the hybrid materials and assess their efficiency as potential absorbent for the dye removal, the spectrophotometric studies have been carried using methylene blue (MB), methyl orange (MO) and rhodamine B (RhB) as the model compounds.

Outcomes of such experiments are influenced by many factors including intrinsic properties of dyes and hybrid as well as experimental settings such light exposure (light flux and duration), concentration range, pH and time. Firstly, light transmittance through solution depends on the material's optical properties (e.g. molar absorptivity co-efficient), its concentration (Beer-Lambert Law) and dispersibility (undesirable scattering by particles). Secondly, the adsorbent/ photocatalyst active surface determines the rate of adsorption-desorption, and finally, photostability of the dyes on their own can lead to over or underestimation of the results. Thus, it is essential to determine an optimal concentration of dyes and optimal loading of the adsorbent within the optimal window of transmission (T = 20-60%) [265] prior conducting kinetics experiments.

4.9.1 Determination of Optimal Concentrations of the Model Dyes: Standardisation Curve

To identify accurate concentrations of the model dyes for further dye removal experiments, the standardization curves of MB, RhB and MO have been established. Stock solutions with the following concentrations were prepared for MB (9.48×10^{-4} M, recording at λ_{max} 664 nm), MO (9.37×10^{-4} M, recording at λ_{max} 464 nm), and RhB (9.74×10^{-4} M recording at λ_{max} 553 nm) and the absorption values at λ_{max} for every 10 µL addition of the dye stock solution were recorded. A calibration curve of absorbance against the dye added volume and concentrations are displayed in Figure 4.4. The experimental data for RhB, MB and

MO can be linearly fitted; and high regression coefficient values (R^2 = 0.999, 0.997 and 0.999, respectively) indicate a very good fit for all dyes even at high absorbances. This translates that the molar absorptivity is constant over the concentrations and therefore, the concentrations of all dyes can be determined with a good precision.

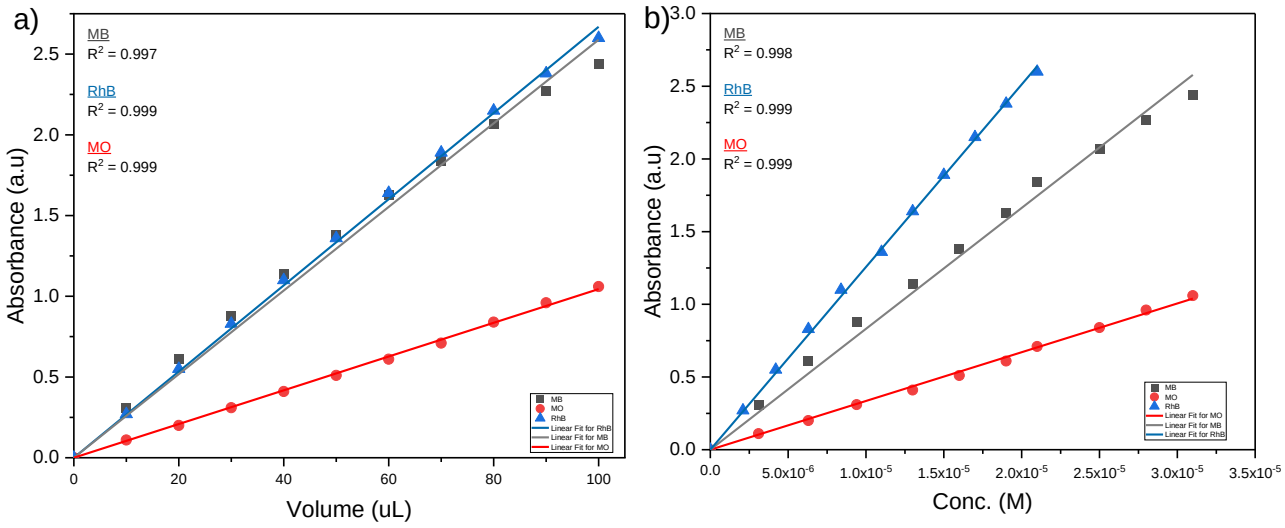

Figure 4.4: (a) Standardisation curves prepared by adding 0.01 mL of the corresponding dye stock solution (MB, MO, RhB; 9.44 × 10^{-4} M); (b) Standardisation curves of RhB, MB and MO presented as a function of the dye concentration (M)

Experimentally found molar absorptivity co-efficient, e (M cm)$^{-1}$, for the maximum wavelength of visible light absorption in water are displayed in the Table 4.1.

Table 4.1: Summary of experimental molar absorptivity co-efficient (e), optimal concentrations (OC), and the transmittance (T) of dye solution at OC.

	RhB, l_{max} 553 nm	**MB, l_{max} 664 nm**	**MO, l_{max} 464 nm**
e, M^{-1} cm^{-1} in water	125,609 ± 602	83,150 ± 1260	33,536 ± 293
OC range, M	1.24 × 10^{-5}	1.54 × 10^{-5}	2.43 × 10^{-5}
%T (A) at OC		20% (0.72) – 60% (0.22)	

A wide variation in the molar absorptivity values for the dyes, indicates that MO colour

intensity is the weakest, while even miniscule amount of RhB can produce coloured solutions. Based on these observations, it was decided to use the following optimal concentration range 10-50µL based on the solution transmittance for the initial studies to determine the photostability of dyes. (Table 4.1).

4.9.2 Photostability of the Model Dyes Under Different Illumination and pH Conditions

Dyes are prone to (photo)-degradation under sunlight, which comprises of ca. 3-5 % of UV, 42-43 % visible and 52-55 % of IR components. Thus, the visible light will have a greater impact on the potential self-degradation. Moreover, the dye's stability can be affected by the pH of a medium, they are in. To establish working conditions and minimise potential errors that can arise due to self-degradation accelerated by light intensity (flux) and pH, the photostability studies have been carried on MB at optimal concentration of 1.54×10^{-5} M.

Previous studies show that MB in wastewater is relatively stable to solar radiation[241], with about 8 % of degradation after 10 hr under irradiation[242]. Figure 4.5 (a) and Figure 4.11(a-c) in the appendix summarises self-degradation of MB in acidic, neutral and basic pH under irradiation with visible light for 30 minutes. Under visible light radiation, MB shows up to 20 % of self-degradation (or bleaching) under basic condition, while 4% of colour removal was observed in both acidic and neutral conditions after 30 minutes irradiation. The difference in the colour removal rate under basic pH could be due to the conversation of MB (coloured) into its leuco form (colourless); however, this process is slowly reversible.

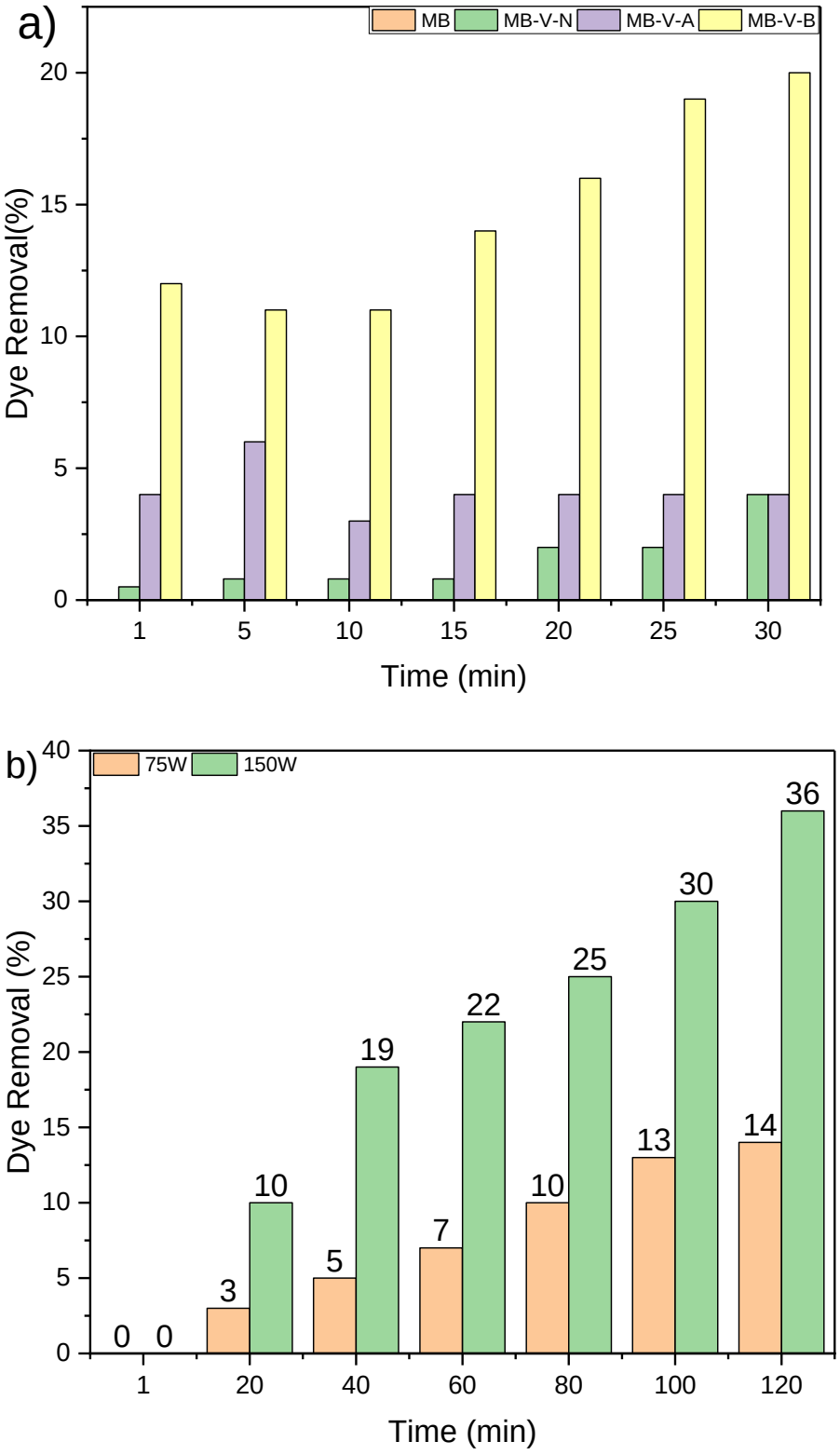

Figure 4.5: (a) Photostability of MB under visible light, in neutral, basic, and acidic pH illuminated by Xenon lamp @75W for 30 min, (b) Self-degradation (photolysis) of MB under neutral and 75W and 150W visible illumination for 120 min.

It has been shown that both acidic and neutral conditions yield lower degradation than under basic pH. Acidic pH shows most stability, this highly due to protonation and stabilisation of MB preventing further degradation. Therefore, further study was conducted under only neutral pH with different visible light intensities; 75W and 150W at longer exposure time of 2hr. As shown in the plot of % of dye remaining against time (min) in Figure 4.5 (b), 15% and 36% of decolouration were observed under 75W and 150W, respectively. Hence, neutral and 75W visible conditions have been adopted for this research.

4.9.3 Determination of Optimal Mass Loading of Graphene-Based Materials

In initial stages of heterogeneous reactions such as adsorption or photocatalysis, the rate of the process is directly proportionate to the mass of the adsorbent or photocatalyst; however, as the reaction time progresses, the process becomes independent of the adsorbent (photocatalyst) mass. Second potential pitfall is that excess of the catalyst leads to a decrease of the light transmission through the medium, which in turn reduces the photon uptake by the photocatalyst (screening effect). Excess of the freely dispersed catalyst can also lead to unwished aggregation, which greatly reduces adsorption capacity of the material. Thus, optimal mass of the adsorbent must be chosen to maximise reaction rate and to avoid unnecessary excess or lack of catalyst.

4.9.4 Optimal Loadings of the Catalysts Using MB as the Dye Standard

Both graphene and its composites have adsorption capacity primarily due to a relatively large surface. It is therefore important to examine the loading capacity of each catalyst, to identify the most suitable concentration for the spectrophotometric analysis, MB was used as a model dye due to a relative easiness of detection of its signal in the red region of the visible spectrum. A stock solution of 1mg/mL of catalysts was used to prepare a range of

concentrations (0.0164, 0.0244, 0.0323, 0.0400, 0.0476, 0.0551 and 0.0625 g/L) equivalent to 0.05, 0.075, 0.100, 0.125, 0.150, 0.175- and 0.200-mL of the respective stock solution of catalysts. These were added in to different cuvette containing a solution of 3 mL DI water and 0.05mL MB. UV-vis absorption spectra of MB were recorded at 5 min intervals during 20 min experiment; the absorption intensity at 650 nm against the volume of catalyst added were plotted and shown in

Figure 4.6.

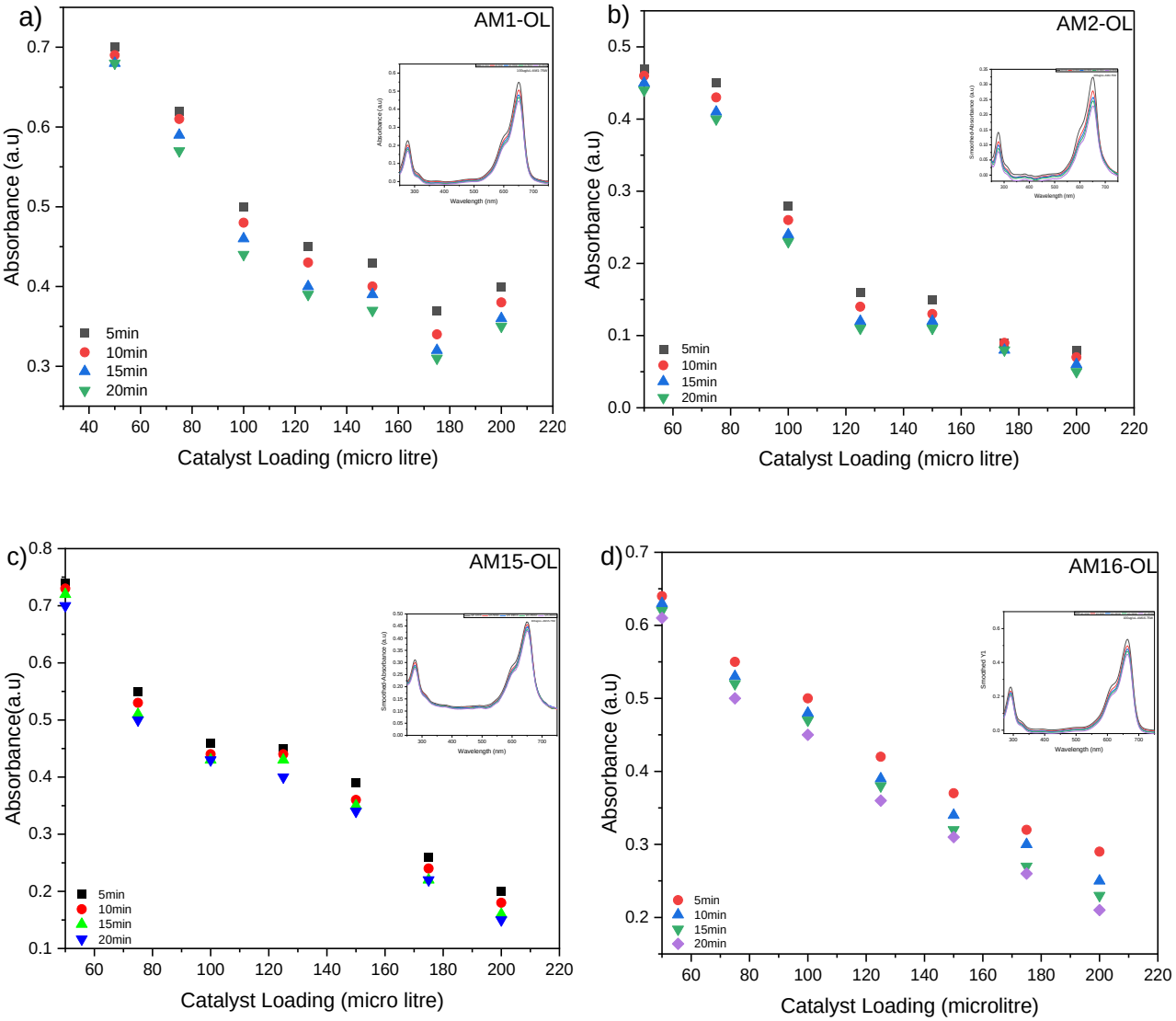

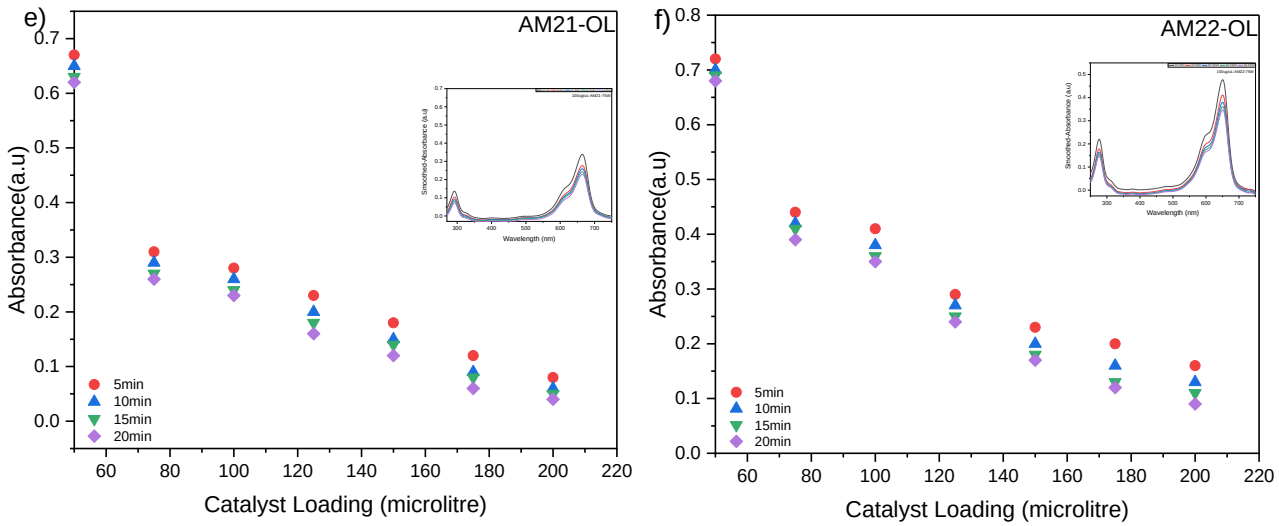

Figure 4.6: (a-f) Plots of MB absorption intensity at 650 nm against the volume of added catalyst stock solution (50 - 200µL or 0.05 - 0.2 mL) for 20 min at time interval of 5 min: a) GP-Chr (AM1), b) GP-Acr (AM2), c) GP-Acn (AM15), d) GP-Pnz (AM16), e) GP-Fsc (AM21), f) GP-Thio (AM22).

Table 4.2: Calculated q(t) values in mg/g for the range of concentrations (g/L) of the hybrid materials recorded at 5 min, 10 min, 15 min and 20 min for the MB adsorption.

	GP-Chr (AM1), 229 m^2/g				**GP-Acr (AM2) 301 m^2/g**			
g/L	**q(5)**	**q(10)**	**q(15)**	**q(20)**	**q(5)**	**q(10)**	**q(15)**	**q(20)**
0.0164	2.35	4.69	7.04	7.04	9.39	11.73	14.08	16.43
0.0244	14.19	15.77	18.93	22.08	9.46	12.62	15.77	17.35
0.0323	25.04	27.43	29.81	32.20	27.43	29.81	32.20	33.39
0.0400	25.00	26.93	29.81	30.77	33.66	35.58	37.50	38.47
0.0476	22.62	25.04	25.85	27.47	29.08	30.70	31.50	32.31
0.0551	23.73	25.82	27.22	27.92	29.31	29.31	30.01	30.01
0.0625	19.08	20.31	21.54	22.16	26.47	27.08	27.70	28.31
Median				27.47				30.01
	GP-Acn (AM15) 224 m^2/g				**GP-Pnz (AM16) 152 m^2/g**			
0.0164	2.35	4.69	7.04	11.73	7.04	9.39	11.73	14.08
0.0244	31.54	34.70	37.85	39.43	18.93	22.08	23.66	26.81
10.0323	34.58	36.97	38.16	38.16	20.27	22.66	23.85	26.23
0.0400	28.85	29.81	30.77	33.66	24.04	26.93	27.89	29.81
0.0476	29.08	31.50	32.31	33.12	24.23	26.66	28.27	29.08
0.0551	34.20	35.59	36.99	36.99	24.43	25.82	27.92	28.61
0.0625	33.85	35.08	36.31	36.93	23.39	25.85	27.08	28.31
Median				36.93				28.31

	GP-Fsc (AM21) 271 m^2/g				GP-Thio (AM22) 232 m^2/g			
0.0164	7.04	11.73	16.43	18.77	4.69	9.39	11.73	14.08
0.0244	61.51	64.66	67.82	69.39	47.31	50.47	52.05	55.20
0.0323	50.08	52.47	54.85	56.05	39.35	42.93	45.31	46.51
0.0400	45.20	48.08	50.01	51.93	43.27	45.20	47.12	48.08
0.0476	42.01	44.43	45.24	46.85	41.20	43.62	45.24	46.04
0.0551	40.48	42.57	43.27	44.67	37.69	40.48	42.57	43.27
0.0625	38.16	39.39	40.01	40.62	35.70	37.54	38.77	40.01
Median				46.85				46.04

The adsorption capacity (q_t) or loading of adsorbate (dye) on the adsorbent surface was calculated using the following equation:

$$q_t = \frac{(C_0 - C_t)}{C_s} = \frac{(A_0 - A_t)}{\varepsilon\, l\, C_s}$$

Where C_o and C_t can be devised from Lambert-Beer Law (l=1cm, e in L/mg cm), and C_s is the concentration of catalysts in g/L.

As expected, MB adsorption on GP-Chr (AM1) increases with increasing the catalyst loading; and the concentration range between 0.075-0.15 mL of added catalyst falls within the transparency window of 0.2-0.7 (Abs) (

Figure 4.6). The adsorption capacity q(t) of GP-Chr (AM1) at 20 min varies between 7.0-32.2 mg/g signifying a moderate adsorption of the catalyst with the maximum adsorption capacities of 32.2 mg/g and 30.8 mg/g at 0.323 g/L and 0.4 g/L of the catalyst loading, respectively. (Table 4.2)

Adsorption capacity of GP-Acr (AM2) was found to be slightly better than that of GP-Chr (AM1) with the q(t) range between 16.4-38.5 mg/g at 20 min. There is a rapid increase in MB adsorption indicated by a drop in the MB intensity at 650 nm at 0.1 mL and 0.125 mL corresponding to 0.323 g/L and 0.4 g/L of the catalyst loading. The data in Figure 4.3(b)

shows stagnation to absorb MB efficiently for higher loadings pointing at the limited capacity of the material. Although 0.4 g/L (0.125 mL) of the catalyst loading has the highest q(t) of 38.5 mg/g, only 0.05-0.1 mL corresponding to 0.0165-0.0323 g/L of catalyst loadings fall within the transparency window.

There is an improvement in the adsorption capacity for GP-Acn (AM15); a drop in the intensity of MB absorption at 650 nm is rapid for the two data points at 0.75 mL and 0.1 mL giving q(t) values of 39.4 mg/g and 38.2 mg/g, respectively. However, the adsorption capacity reduces for 0.125-0.15 mL of the catalyst, which is evident by a decrease in q(t) values. Noteworthy, the adsorption capacity recovers at higher catalysts loadings (0.055 g/L and 0.063 g/L) to 36.99 mg/g and 36.93 mg/g, respectively. However, it is still lower than that at lower concentration. This unexpected increase could be due to a secondary adsorption at the surface of the catalyst.

The performance of GP-Pnz (AM16) is comparable to GP-Chr (AM1) and GP-Acr (AM2); although it shows higher adsorption capacity than GP-Chr (AM1) reaching 28.1 mg/g and 28.8 mg/g, it requires a higher catalyst loading of 0.4 g/L and 0.476 g/L, respectively.

A massive improvement in the adsorption capacity was observed in both GP-Fsc (AM21) and GP-Thio (AM22). Both materials show best q(t) values at lower concentrations (0.075 mL and 0.1 mL) which slowly decrease with the increase of the catalysts loading; these catalysts concentrations are within the optical window for optimal measurements. For both materials, best q(t) values are obtained at 0.075 mL (0.024 g/L) and are 69.4 mg/g for GP-Fsc (AM21) and 55.2 mg/g for GP-Thio (AM22).

To rate overall performance of the materials, ‘median’ value can be used instead of ‘average’ or ‘maximum’ value as the former represents the middle of the data distribution separating the higher half from the lower half values of the data set.

The data in Table 4.2 shows that the optimal catalysts loading varies between the samples and is in the range of 0.0244-0.0476 g/L. Taking into the account the accurate transmission window, it was decided to take 0.0323 g/L as the final optimal concentration for all materials.

4.9.5 Adjusting the Optimal Concentration of MB, RhB and MO Dyes for the Optimised Catalyst Loading

It is important to identify a suitable concentration of the system (catalyst and dye) acceptable within the transparency window, which affects attainable accuracy of the photometric experiment. Light transmission/ absorption of dyes is altered by the large loadings of graphene sheets dispersion resulting to deviation from Beer-Lambert law. Similarly, a very low concentration of catalyst in relation to dye concentration can affect the adsorption rate of dye on the catalyst surface; therefore, it is necessary to identify a suitable mass loading for individual catalysts. Factors responsible for the extent of dye adsorption on the catalysts includes a) π-π interaction between graphene and functional groups on its surface and the dye molecules (adsorbate), b) surface area of the catalysts, and c) other electrostatic interactions (including potential ionic interactions) between the adsorbate and the catalysts.

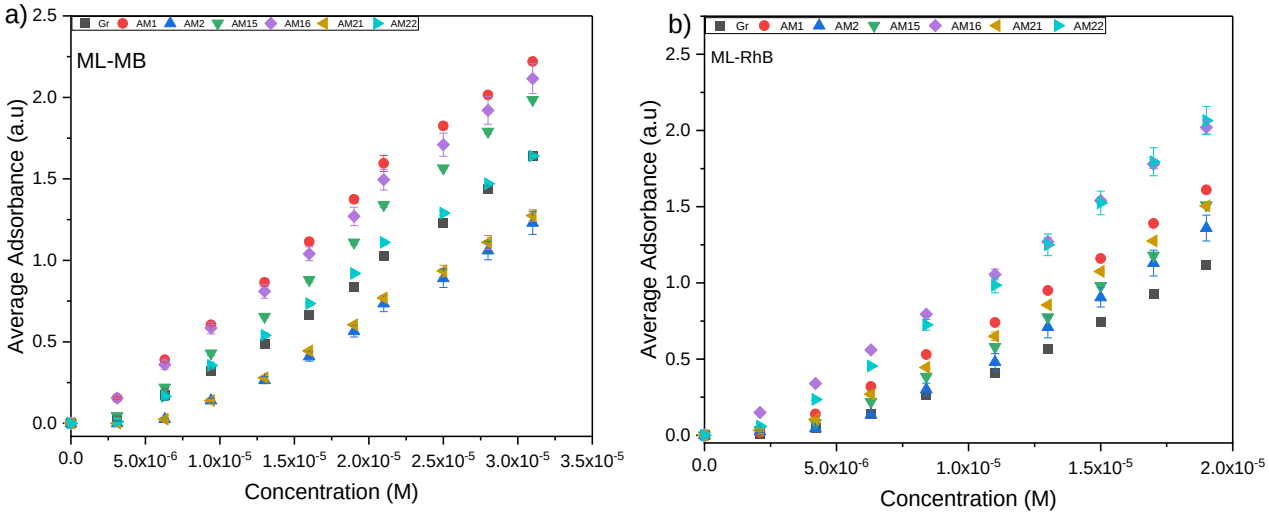

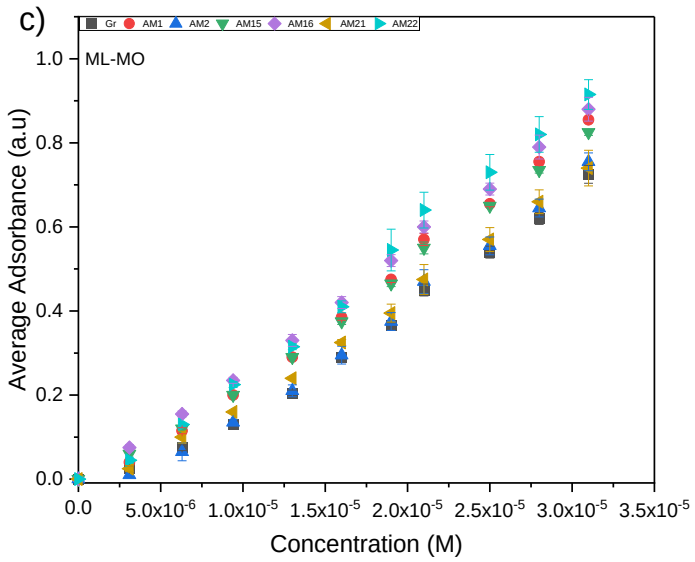

Figure 4.7: Average adsorption intensities of the adsorbates: (a) Mass loading of Methylene blue (MB),(b) Mass loading of Rhodamine B (RhB) and (c) Mass loading of Methyl Orange (MO), 0.01-0.1mL against constant concentration (0.0323 g/L) of the catalyst

Figure 4.7 shows plots of average light absorption of adsorbate: MB (intensity at l_{max} 664 nm), RhB (intensity at l_{max} 554 nm) and MO (intensity at l_{max} 450 nm) against their loadings in the presence of the individual catalysts (constant concentration of 0.0323 g/L): GP, GP-Chr, GP-Acr, GP-Acn, GP-Pnz, GP-Fsc and GP-Thio. ML-MB series shows the range of the suitable concentrations (yellow band). However, Figure 4.11 in the appendix shows UV-vis spectra of various catalysts with MB, where a red shift from 664 nm (monomer) is observed. This is explained in literature[243] by showing that the formation of MB dimer begins in the concentration range between 1×10^{-5} and 1×10^{-4} M and matches the concentrations where dimer begins to form in all ML-MB samples (>$3.1x10^{-5}$ M).

Similarly, Figure 4.12 in the appendix shows UV-vis spectra of various catalysts on RhB. A strong absorption peak at 553 nm which is characteristic of the π-π* electronic transition of the RhB dye monomer was observed, while the shoulder peak at 515 nm is attributed to the RhB dimers[244] in ML-RhB series. The concentration range for the dimer formation starts at 1.55×10^{-5} M.

4.9.6 Kinetics Study

Kinetics studies have been carried using the following conditions in all kinetics experiments: the concentration of the catalysts was 0.0323 g/L; the stock concentrations of dyes (adsorbents) were 9.48 x 10^{-4} M for MB, 9.37 x 10^{-4} M for MO and 9.74 x 10^{-4} M for RhB. The adsorption study was carried out under neutral pH in the dark; UV-vis absorption spectra were recorded every 20 min during 120 min experiment. The photochemical activity study (light reaction) was carried out under the illumination with white light produced by xenon lamp (75W, optical cut-off filter >420nm) under neutral pH during 120 min experiments. Similarly, the UV-vis absorption spectra were recorded every 20 min.

4.9.7 Adsorption Study of the Dye Models

The results of the adsorption experiments carried out in the dark to determine physisorption capacity of the catalysts are summarised in the

Figure 4.8. It is important to note for further discussion that MB and RhB are cationic dyes, while MO is a basic dye. Therefore, it is expected that the trend in the adsorption capacity of the individual catalysts toward MB and RhB can be similar.

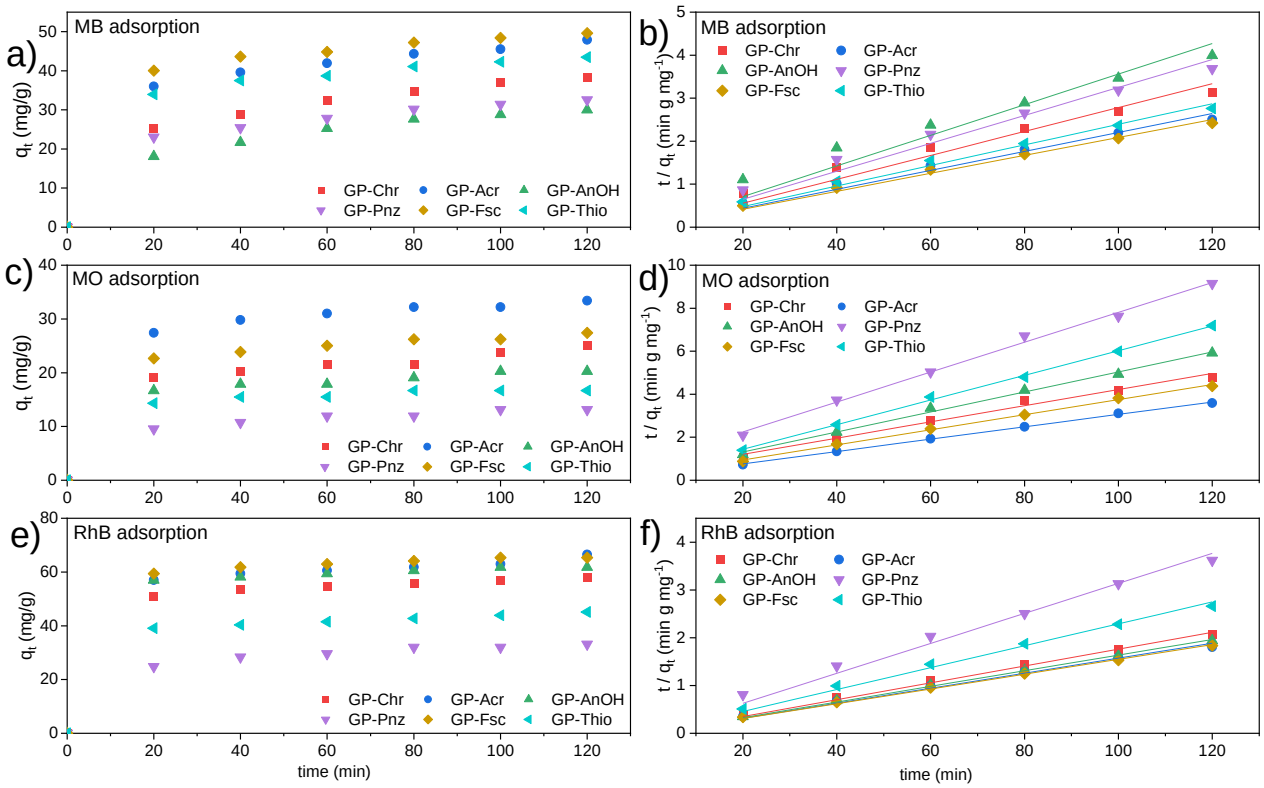

Figure 4.8: a,c and e right) are summary of adsorption capabilities of MB, MO and RhB dyes for GP modified samples (0.0323 g/L) studied by spectrophotometric method monitoring absorbance decreases at 464 nm (MO), 664 nm (MB) and 553 nm (RhB) over 120 min. (b, d and f left) are linear adjustment of pseudo-second order kinetic model.(a-f) colours represents the following composites; GP-Chr (red), GP-Acr (blue), GP-AcnOH (green), GP-Pnz (purple), GP-Fsc (orange) and GP-Thio (cyan).

The adsorption capacity of MB in

Figure 4.8 (a) is highest for GP-Fsc (49.6 mg/g), GP-Acr (47.9 mg/g) and GP-Thio (43.5 mg/g). They are trailed by GP-Chr (38.3 mg/g), which is followed by GP-Pnz and GP-Acn with a relatively similar adsorption rate of 32.6 mg/g and 30.0 mg/g, respectively. These results for the first three materials are very encouraging; especially when the loading can be improved by optimising the concentration of the catalysts (Table 4.2). They are in line with other examples from the literature for MB adsorption: zeolites (47.3, 22.0, and 5.6 mg/g), mesoporous activated carbon/zeolite composites (15.49, 47.95 mg/g), activated carbon from biomass waste, chitosan-zeolites [267-269].

Lower adsorption capacity of Gr-Chr could be due to i) mild electrostatic interactions between OH and C=O groups of the methyl chromone and nitrogen and sulphur containing groups of the MB (0.638 and -32*mV*) and ii) poor π-π interaction between GP-Chr and MB due to the presence of bulky Me groups in both. Although the surface area in GP-Pnz is smaller than that of GP-Acn, however, its adsorption capacity is higher because of the preferential π-π stacking between phenazine `molecules and MB. Higher adsorption capacity of GP-Acr compared to other catalysts is due to i) good π-π interaction between the hybrid and MB and ii) great electrostatic attraction between the two opposite charges of Gr-Acr and MB (0.68 and -3.0 *mV*) with relatively close charge strength.

Figure 4.8 (b) shows a plot of average adsorption capacity of RhB for the series. Overall performance of the materials against RhB is better. A similar adsorption pattern to one observed for MB, is evident for GP-Fsc (63.35 mg/g) and GP-Acr (63.00 mg/g), which is closely followed by GP-Acn (61.77 mg/g). Other materials also show higher adsorption capacity with GP-Chr, GP-Thio and GP-Pnz being 58.19 mg/g, 45.08 mg/g and 33.15 mg/g, respectively.

Figure 4.8 (c) shows kinetic plots of MO adsorption by various catalysts revealing much weaker adsorption of MO. GP-Acr (33.50 mg/g) and GP-Fsc (24.75 mg/g) which is closely followed by GP-Chr (21.40 mg/g). Other materials; GP-Acn, GP-Thio and GP-Pnz shows lower adsorption capacity with plateau graphs at16.19 mg/g, 14.79 mg/g and 9.97 mg/g, respectively. The structure of MO is not flat and therefore not favourable for efficient electrostatic interactions such as π-π stacking. Figure 4.8 (b, d and f) represents the linear

fittings of the catalysts adsorption of MB, RhB and MO respectively, all showing great fittings (R^2 > 0.99) using pseudo-second order kinetics

Figure 4.9 summarises the total dye removal of the three model dyes. The removal of RhB is the most efficient with all the catalysts used followed by MB and MO. Modified graphene with acridine dye (GP-Acr) manifested the highest removal capacity for all three dyes among the series showing MB – 85%, RhB – 99% and MO – 45%. It was closely followed by GP-Fsc removing MB – 83%, RhB – 90% and MO – 40%. The materials based on oxygen containing chromophore (GP-Acn and GP-Chr) demonstrated similar activity for MB between 50-60%, RhB – 80-90% and MO between 30-35%. Total removal employing GP-Thio was 58% for MB, which is similar to GP-Chr, RhB – 70% and MO – 25%. GP-Pnz was the least effective one only removing MB – 40%, RhB – 58% and MO – 23%.

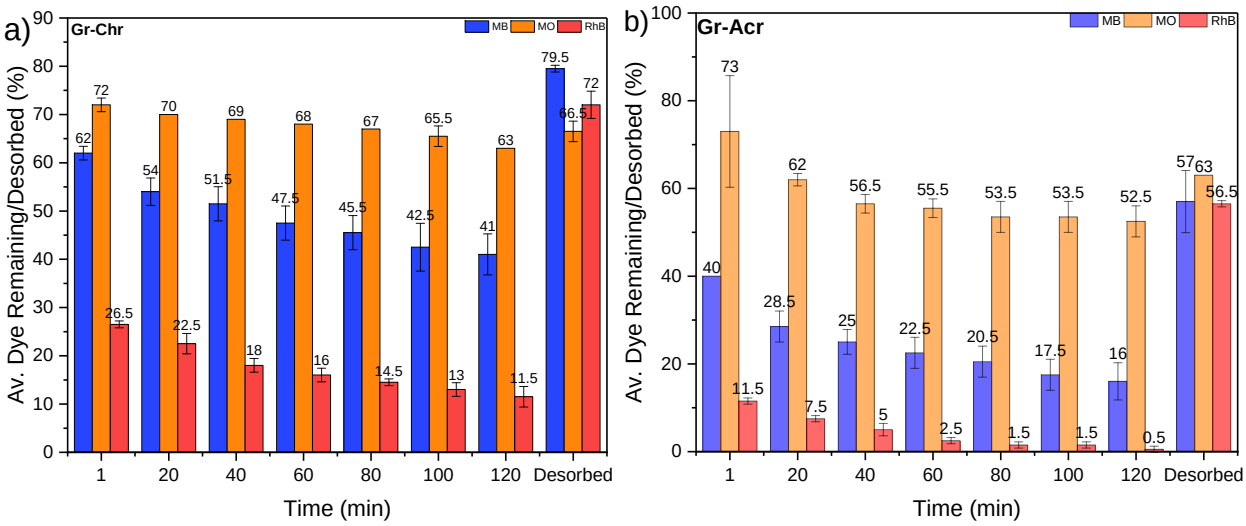

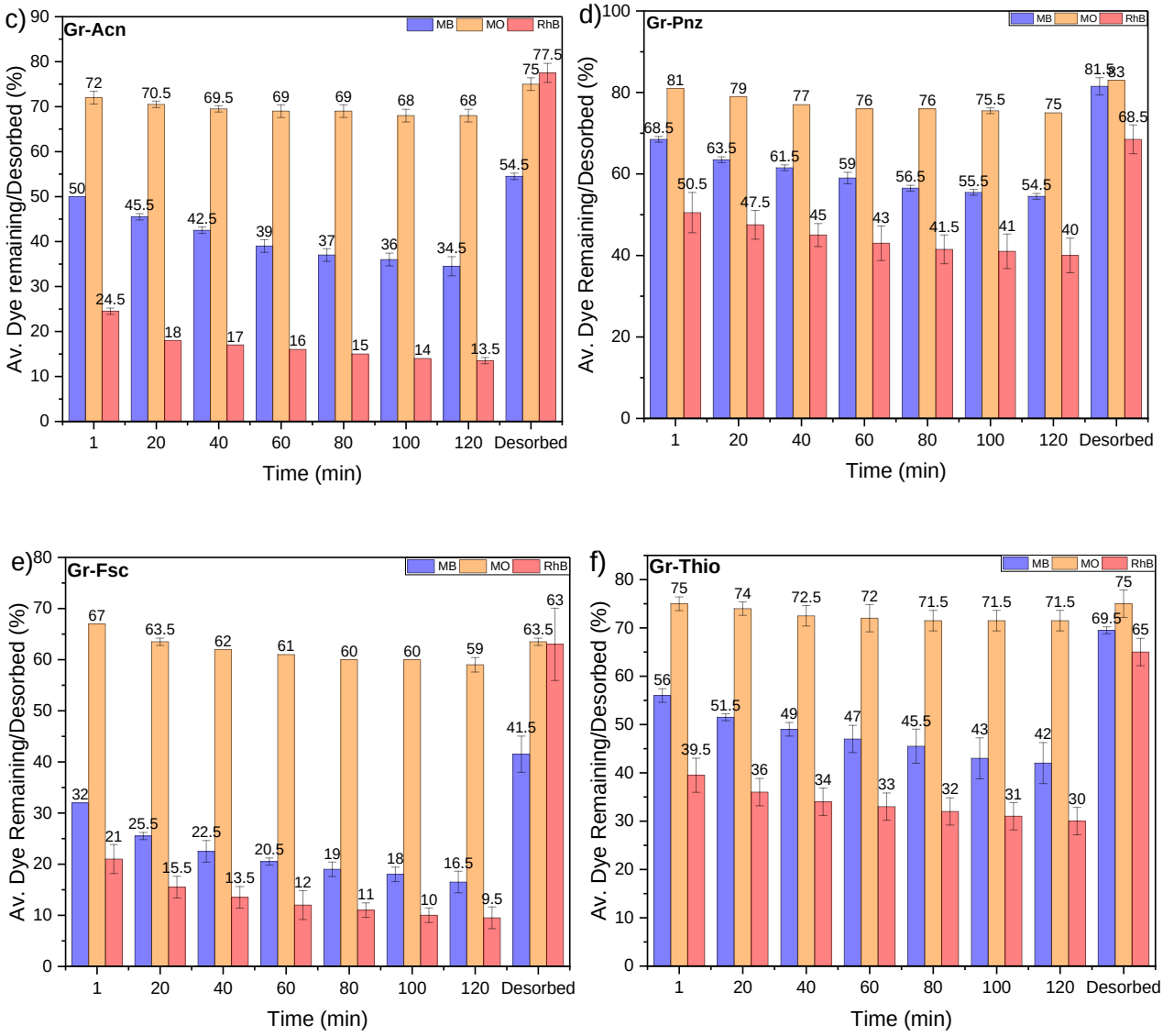

Figure 4.9: (a-f) Average dye removal calculated for MB (blue), MO (orange) and RhB (red) monitored over 120 min in the dark in the presence of the catalyst (0.0323 g/L). and desorption of the dye upon addition of EtOH (D-Dyes). Graphs (a-f) represents dark activities of; a) GP-Chr, b) GP-Acr, c) GP-Acn, d) GP-Pnz, e) GP-Fsc, f) GP-Thio.

4.9.8 Photodegradation of Model Dyes: MO, RhB and MB

Since all the catalysts manifested the capacity to adsorb the different types of dye models used under dark, atmospheric and neutral conditions. It is imperative to conduct an experiment under the same condition and in the presence of white light to check whether or not, the modified catalysts possess photoactivity and to what degree. GP-Acr, GP-Fsc,

GP-Pnz and GP-Thio all have a pronounced band in the visible spectrum, which originates from the chromophore moiety (

Figure 2.5 in Chapter 2). Thus, they may have potential photocatalytic activity under visible light illumination, which can assist in overall dye removal.

Figure 4.10 (a-g) summarises the dye removal for the graphene-based composites. As with the adsorption experiments (dark reaction), the overall removal of MO under light is the lowest, while RhB is highest. The individual percentage removal of the dyes, has GP-Fsc with the highest (99%) removal with MB, followed by GP-Acn, GP-Acr and GP (unmodified), with (85-91%), Gr-Thio and GP-Pnz (75-77%), while GP-Chr has the lowest removal rate (50%). GP-Acr manifest highest removal rate of (100%) with RhB, followed by GP with (99%), GP-Fsc with (95%) and GP-Chr, GP-Acn with (85%), GP-Thio with (79%) and GP-Pnz with the lowest (58%). MO with the least adsorption rate, has (33-51%) percentage removal with GP-Thio, GP-Chr, GP-Acr and GP. GP-Fsc and GP-Acn with (29-31%) and GP-Pnz with (15%).

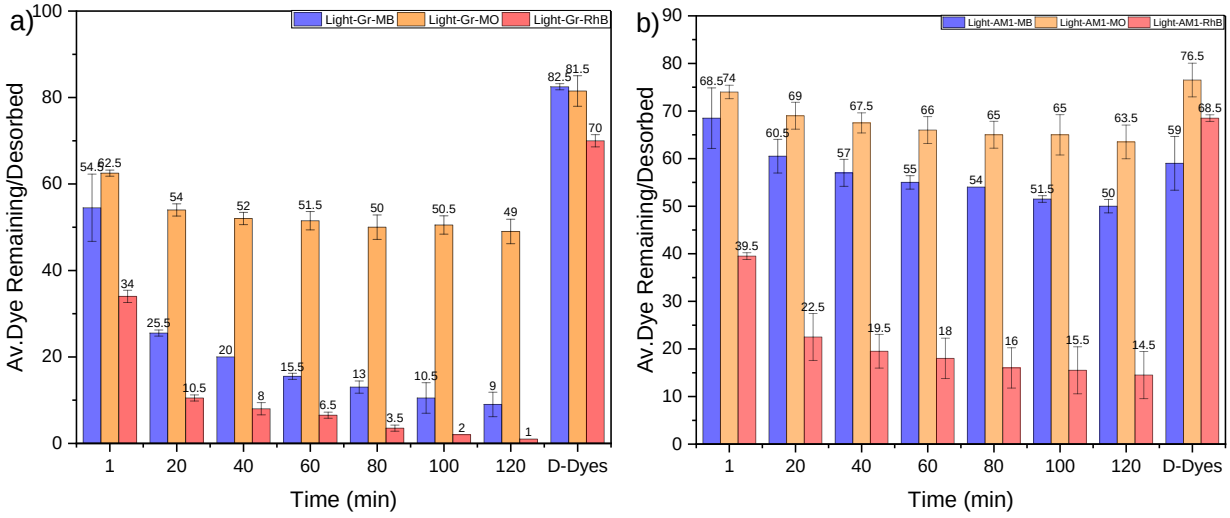

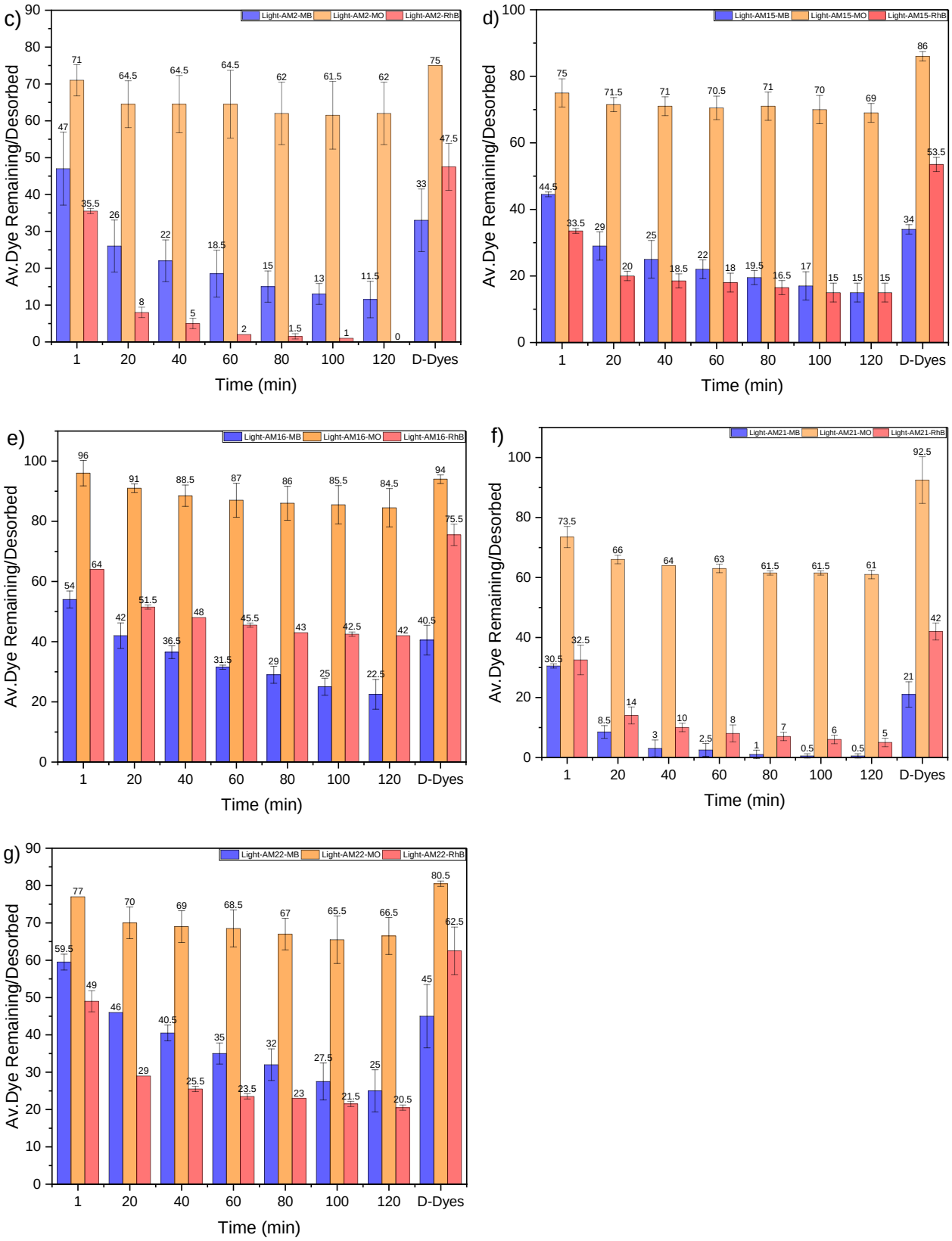

Figure 4.10: Photoinduced removal of MB (blue), MO (orange) and RhB (red) by the composites monitored during 120 min under white light illumination. Plots of average remaining dye against time; and desorption of the dye upon addition of EtOH (D-Dyes). Graphs (a-g) represents Light activities of; a) GP, b) GP-Chr, c) GP-Acr, d) GP-Acn, e) GP-Pnz, f) GP-Fsc, g) GP-Thio.

To better understand the mechanism of dye-removal, desorption experiments were carried out at the end of 120 min runs adding EtOH and leaving the mixture to stir for 5 min prior the scan. The data was corrected by the dilution factor and average values were calculated (column labelled: D-Dyes). (Figure 4.10, Table 2.1) Adding EtOH to the mixture of graphene and MB revealed that 71% of MB can be desorbed confirming that graphene has no noticeable ability to trap the contaminants.

Table 4.3: Summary of MB removal-desorption studies for GP and the modified samples under light (L) and dark (D) conditions.

	Adsorbed (%) L / D	Desorbed (%) L / D	Trapped (%) L / D
MB			
GP	92 / 76	83 / 71	9 / 5
GP-Chr	50 / 77	59 / 44	0 / 33
GP-Acr	88 / 94	33 / 43	55 / 51
GP-Can	85 / 85	34 / 48	51 /37
GP-Pnz	77 / 41	41 /70	36 / 0
GP-Fsc	99 / 99	21 / 24	78 / 75
GP-Thio	75 / 50	45 / 59	30 / 0
RhB			
GP	99/100	70/63	29/37
GP-Chr	85/88	69/72	16/16
GP-Acr	100/99	48/57	52/42
GP-Can	85/86	54/78	31/8
GP-Pnz	58/60	76/69	0/0
GP-Fsc	95/90	42/63	53/27
GP-Thio	79/70	63/65	16/5

MO			
GP	51/47	82/60	0/0
GP-Chr	36/37	64/63	0/0
GP-Acr	38/47	72/63	0/0
GP-Can	31/32	86/75	0/0
GP-Pnz	15/25	94/83	0/0
GP-Fsc	29/41	93/64	0/0
GP-Thio	33/28	81/75	0/0

These removal-desorption results are influenced by multiple factors, and the mechanism of removal involves electrostatic interactions between the surface units and the dye molecules. Binding of molecules on surfaces is influenced by the dipole moments of the surface and adsorbent, which can be permanent, induced or fluctuating.[29] It is likely that the orientation of the dye (adsorbent) on the surface of graphene is influenced by pi-pi stacking; thus, a larger surface area should be a rate determining factor at the start. The surface area decreases in the following order Graphene > GP-Acr > GP-Fsc > GP-Thio > GP-Chr > GP-Can > GP-Pnz, but it cannot account alone for the activity observed.

The low MO removal can be attributed to unfavourable electrostatic interactions (mainly repulsion) between MO and the functionalities on the graphene surface. This shows that pi-pi interactions between aromatic system of MO and graphene hybrids are not sufficient to successfully remove the dye. In contrast the removal of MB and RhB are mostly successful with a few exceptions. The low dye removal efficiencies of GP-Pnz and GP-Thio manifest from a lower surface area, but also to the presence of similar functional groups (-NR_2), which can cause electrostatic repulsion. The presence of a -CO_2H group

on GP-Fsc allows efficient binding of cationic dyes leading to the formation of GP-Fsc*MB or GP-Fsc*RhB salt, which can explain both the good adsorption and retention abilities. Although GP-Acn and GP-Chr have a surface area almost twice as small as unmodified graphene, they can bind the cationic dyes through the presence of >C=O functional groups. Similar retention rates of these two hybrids confirm this hypothesis. GP-Acr has the largest surface area of hybrids, and the presence of an imine function (-N=) allows favourable dipole interactions with MB and RhB, and it performs much better than unmodified graphene in terms of dye removal.

4.10 Summary

1mg/mL and 0.3mg/mL stock solutions of the catalysts and dye models; MB, MO and RhB (9.48×10^{-4} M, 9.37×10^{-4} M, 9.78×10^{-4} M) have been prepared. Spectroscopic study to determine the photostability of the MB dye was carried out under visible light illuminations at 75W for 30 min initially and later at extended time for 120 min under 75W and 150W, illuminations. Removals of 4% was observed under 75W illumination and 30 min, while 12% and 36% respectively have been recorded under 75W and 150W illuminations respectively for 120 min. Optimal concentration for all the catalysts was observed to be 0.0323g/L, while 4.97×10^{-3}g/L, 7.97×10^{-3}g/L and 4.62×10^{-3}g/L optimal concentrations of the dye models; MB, MO and RhB have been identified and recorded. Kinetics studies of both dark and light conditions were carried out under neutral and 120 min conditions for all the catalysts. Adsorption experiments were carried out on all the catalysts using the three model dyes and their capacities were recorded. And finally, kinetics studies were also conducted under both dark and light conditions for 120 min with all the catalysts using the three model dyes. Desorption study was done using ethanol to differentiate between physisorption and photoactivity of the materials.

4.11 Conclusions

Adsorption studies revealed that most graphene-chromophore hybrids can successfully remove MB and RhB from aqueous media and have superior performance to that of unmodified graphene.

The best results have been achieved for RhB removal, which is consistent with the conclusions described for the adsorption experiments: GP-Acr > GP > GP-Fsc > GP-Chr ~ GP-Acn > GP-Thio > GP-Pnz, followed by the removal of cationic dye MB in the following order: GP-Fsc > GP-Acr > GP-Acn > GP-Thio ~ GP-Pnz > GP-Chr.

The photocatalytic efficiency of the dye removal was studied on the samples which contain visible light chromophores (GP-Acr, GP-Fsc, GP-Pnz and GP-Thio) under visible light illumination, and the following order of increasing efficiency was observed: GP-Fsc ~ GP-Acr > GP-Chr > GP-Thio > GP-Acn > GP-Pnz, which is similar to what was observed for the adsorption studies. The photodegradation performance/efficiency was calculated by taking differences of the trapped dyes after adding EtOH (desorption) in all experiments under both dark and light conditions. The following order was observed in all the dyes; GP-Pnz > GP-Thio > GP-Acn > GP-Acr > GP-Fsc for MB. The synergistic effect of adsorption and light-assisted degradation was efficiently demonstrated by GP-Pnz and GP-Thio, where a dramatic increase in MB and RhB removal were observed. Although, GP-Pnz has the lowest surface area (152 m^2/g) and low adsorption capacity of 77% but it has the highest photocatalytic capacity of 36%.

5 Thesis Conclusion and Future Work

Covalent radical modification of graphene nanoplatelets with six different organic dyes (chromophores) have been successful using a facile one-pot functionalization method. To enhance the adsorption capabilities of both graphene and chitosan as composite in two and three component system, covalent radical and non-covalent functionalization methods were designed and successfully synthesized using a simple reaction conditions. Both the two and three component systems were synthesized *in-situ*. However, another modification method of the three component system has been introduced using simple organic molecules (H_2N-ArCOOH) as a linker to graphene and chitosan. This method replaces the use of expensive GO or RGO for other covalent modifications. Fabrication of three component system aim at leveraging on the advantages of high surface area of graphene, adsorption property of the chitosan and light harvesting property of the dyes to create a multifunctional catalyst. Finally, a physical mixture of graphene with chitosan was established through one-pot method assisted by ultrasonication. A range of characterisation techniques such as FTIR, PXRD, SEM, BET, TGA, UV-Vis and fluoresce spectroscopy were used to confirm the successful modification of the graphene surface.

FWHM values obtained from XRD data for the modified samples in chapter 1, revealed an increase of 12-38 % as compared to the unmodified graphene, while d_{002}-spacings did not show any significant variation from the unmodified sample (3.33Å). This indicates that all the modification took place on the basal plane and probably the edges of the graphene rather the interlayer (sandwich), because d_{002} spacing of 3.32-3.33Å is too small to contain entities as large as an epoxy group (1.25Å) or a water molecule (2.75Å).[26]

.

Adsorption and photocatalytic activities of the modified samples (graphene-chromophore) have been tested and results show that most hybrids can successfully remove MB and RhB from aqueous media showing a superior performance to that of unmodified graphene. Future work will therefore review the methodology of the covalent radical functionalisation of the graphene by de-stacking the graphene layers using ultrasonication and further characterization methods such as XPS and or Raman spectroscopic analysis will be conducted.

Catalyst recyclability and mechanistic study are two essential aspects that are missing in chapter 4 of this research which need to be captured in our future work.

Also, work to be conducted in the future will include fabrication of graphene-composites in the form of sponges, aero- and hydro- gels. Photocatalytic activities of other organic waste pollutants, membrane filtration and desalination tests of the graphene-polymer hybrids can be carried out.

References

1. M. Zhang, J. Gong, G.Zeng, P. Zhang, B. Song, W. Cao, H. Liu, S. Huan, *Colloid and Surf. A,* 2018, **559**, 169-183.

2. C. Chen, W. Ma, J. Zhao, *chem. soc. Rev.,* 2010, **39**, 4206-4219.

3. J. Carlos, R. Luque, *Chem. Soc. Rev.,* 2014, **43**, 765-778

4. K. Kakaei, M. D. Esrafili, A. Ehsani, *Inter. Sci.& Tech.* 2019, **27**, 153-202.

5. P. Avouris, C. Dimitrakopoulos, *Materials Today,* 2012, **15**, 86-97.

6. Z. Youssef, L. Colombeau, N. Yesmurzayeva, F. Baros, R. Vanderesse, T. Hamieh, J. Toufaily,C. Frochot, T. R.-Carmes, S. Acherar, *Dyes and Pigments,* 2018, **159**, 49-71.

7. S. P. Davis, Biotech. In Agric. Ind. and Med., *Nova Sci. pub. Inc. NY.,* 2011, 71, ISBN: 978-1- 61942-780-8.

8. P. Nechita, Application of Chitosan in Wastewater Treatment, *Intech Open.* 2017, 209-228.

9. K. He, G. Chen, G. Zeng, A. Chen, Z. Huang, J. Shi, T. Huang, M. Penga, L. Hu, *App. Cat.B: Env.* 2018, **228**, 19-28.

10. H. Zhang, X.J. Lu, Y.M. Li, Y. Wang, J.H. Li, *ACS Nano,* 2010, **4**, 380.

11. Y.H Ng, A. Iwase, A. Kudo, R. Amal, *J. Phys. Chem. Lett.* 2010, **1**, 2607.

12. Y.T. Liang, B.K. Vijayan, K.A. Gray, M.C. Hersam, *Nano let.* 2011, **11**, 2865.

13. Y.T. Liang, B.K. Vijayan, O. Lyandres, K.A. Gray, M.C. Hersam, *J. Phys. Chem. Lett.* 2012, **3**, 1760.

14. J.G. Yu, J. Jin, B. Cheng, M. Jaroniee, *J. Mat. Chem. A,* 2014, **2**, 3407.

15. P.Q. Wang, Y. Bai, P.Y. Luo, J.Y. Liu, *Catal. Commun.* 2013, **38**, 82.

16. E.P Gao, W.Z. Wang, M. Shang, J.H. Xu, *Phys. Chem.* 2011, **13**, 2887.

17. E. Bekyarova, M.E. Itkis, P. Ramesh, C. Berger, M. Sprinkler, W.A. deHeer, R.C.

Huddon. *J. Am.* Chem*. Soc.,* 2009, 131, 1336.

18. H. Liu, Y. Liu, D. Zhu, *J. Mat. Chem.* 2011, **21**, 3335-3345.

19. L.C. Geraldine, Q. Paulus, H. Wang, M.S. Strano, *Accts. Of Chem. Res.* 2013, **46**, 160-170.

20. D.P. Martin, A. Tariq, B.D.O Richards, G. Jose, S.A. Krasnikov, N.N Sergeeva, *Chem. Com- mun.* 2017, **53**, 10715-10718.

21. J.M. Englert, C. Dotzer, G. Yang, M. Schmid, C. Papp. J.M. Gottfried, H.-P Steinrueck, E. Spiecker, F. Hauke, A. Hirsch, *Nat. Chem.* 2011, **3**, 279-286.

22. M.Z. Hossain, M.A. Walsh, M.C. Hersam, *J. Am. Chem. Soc.,* 2010, **132**, 15399-15403.

23. F.M Koehler, A. Jacobson, K. Ensshin, C. Stamfer, W.J. Stark, *Small,* 2010, **6**, 1125-1130.

24. A. Das, S. Pisana, B. Chakraborty, S. Piscanee, U. Waghmare, K. Novoselov, H. Khrishna- murthy, A. Geim, A. Ferrari, *Nat. Nanotech.* 2008, **3**, 210-215.

25. Q. Xiang, B. Cheng, J. Yu, *Angew. Chem. Int. Ed.* 2015, **54**, 11350-11366.

26. G.L.C. Paulus, M.H. Ham, Q.H. Wang, A.J. Hilmer, K.K. Kim, C.J. Shih, Z. Ulissi, J. Kong, M.S. Strano. *APS,* 2012, **57**, 1.

27. Q. H. Wang, Z. Jin, K. K. Kim, A. J. Hilmer, G. L. C. Paulus, C.-J. Shih, M.H. Ham, J. D. Sanchez-Yamagishi, K. Watanabe, T. Taniguchi, J. Kong, P. Jarillo-Herrero, M.S.S. Stranos, *Nat. Chem*. 2012, **4**, 724-732.

28. N.N. Sergeeva, A.N Chaika, B. Walls, B.E. Murphy, K. Walshe, D.P. Martin, B.D.O Richards, G. Jose, K. Fleischer, V.Y. Aristov, O.V. Molodtsova, I.V. Shrets, S.A. Krasnikov, *nanotech.* 2018, **29**, 275705.

29. J.M Hermann, *Cat.today*, 1999, **53**, 115-129.

30. L.I Granone, F. Sieland, N. Zheng, R. Dillert, D.W. Bahnemann, *Green Chemistry*,

2018 **20**, 1169-1192.

31. Y. Obeng, P. Shrinivasan, *Electrochem. Soc. Int.,* 2011, 47-52.

32. S. Gadipelli, Z.X. Guo, *Prog. In Mat. Sci.,* 2015, **69**, 1-60.

33. M. Zhang, J. Gong, G. Zeng, P. Zhang, B. Song, W. Cao, H. Liu, S. Huan, *Colloids and Surface A.,* 2018, **559**, 169-183.

34. Y. Zhang, H. Li, L. Kuo, P. Dong, F. Yan, *Current Opinion in Colloid and Int. Sci.*, 2015, **20**, 406-415.

35. K.P. Loh, Q. Bao, P. Kailin, J. Yang, *J. of Mat. Chem.,* 2010, **20**, 2277-2289.

36. H.C. Lee, W-W. Liu, S-P. Chai, A. Mohamed, C.W. Lai, C-S. Khe, C.H. Voon, U. Hashim, N.M.S Hidayah *Procedia Chemistry,* 2016, **19,** 916-921.

37. P. Singh, P. Shandaliya, P. Raizada, A. Sudhaik, A.R-Sani, A. H-Bandegharaei, *Arabian Chemistry*, 2018.

38. M. Pelaez, N.T., Nolan, S.C. Pillai, M.K. Seery, P. Falaras, A.G. Contos, M.H. Entazari, *App. Catal.B: Environ.* 2012, **125**, 331-349.

39. R. Haberl, *Water Sci. Tech.*, 1999, **40**, 11-17.

40. C. Dametgül and N. Beyazit, *carbohydrate polymer*, 2018, **181**, 812-817.

41. D. Ravelli, D. Dondi, M. Fagnoni, A. Albini, *Chem. Soc. Rev.* 2009, **38**, 1999-2001.

42. M.A. Rauf, S.S. Ashraf, *J. of Chem. Eng.* 2009, **151**, 10-18.

43. S. Ahmed, M.G. Rasul, W.N. Martens, R. Brown, M.A. Hashib, *A Review on Current Status Dev. Desalination,* 2010, **261**, 3-18.

44. Y. Lin, C. Ferronato, N. Deng, J.-M. Chovelon, *Appl. Catal. B: Environ.* 2011, **104**, 353-360.

45. D. Haaken, V. Schmalz, T. Dittmar, E. Worch, *J. of Water Supply: Research and Tech.- Aqua*., 2013, **62**, 442-451.

46. P. Raizada, P. Singh, A. Kumar, G. Sharma, B. Pare, S. B. Jonnalagada, P.

Thakur, *Applied Catalysis A: General*, 2014, **486,** 159-169.

47. A. R. Khataee, M. B. Kasiri, *J. of Mol. Catal. A: Chemical*. 2010, **328**, 8-26.

48. C. Combellas, F. Kanoufi, D. Mazouzi, A. Thiebault, P. Bertrand, N. Medard. *Polymer,* 2003, **44,** 19-24.

49. G. Zeb, P. Gaskell, X. T. Le, X. Xio, T. Szkopek, M. Cerruti, *Langmuir.* 2012, **28**, 13042- 13050.

50. P. Viel, X.T. Le, V. Huc, J. Bar, A. Benedetto, A. Le-Goff, A. Filaramo, D. Alamarguy, S. Noel, L. Baraton. S. Palacin, *J. of Mat. Chem.* 2008, **18**, 5913-5920.

51. B. D. Assresahegn, T. Brousse, D. Be'langer, *Carbon*, 2015, **92**, 362-381.

52. N.I Zaaba, K.L. Foo, U. Hashim, S.J Tan, W-W. Liu. C.H. Voon, *Procedia Engineering,* **184**, 469-477.

53. J. Park, M. Yan, *Accounts of Chemical Research,* 2013, **46**, 181-189.

54. S. Sarkar, E. Bekyarova, R.C. Haddon, *Material Today,* 2012, **15**, 276-285.

55. V. Georkilas, M. Otyepka, A.B Bourlinos, V. Chandra, N. Kim, K. C. Kemp, P. Hobza, R. Zboril, K.S. Kim, *Chem. Rev.,* 2012, **112**, 6156-6214.

56. I.A. Vacchi, C.M. Moyan, A. Bianco, *Phy. Sci. Rev.* 2017, 1-18.

57. W.-G. Weng, G.-H. Chen., D.-J Wu, Z.-Y. Lin, W.-L. Yan, *Synthetic Metals*, 2003, **139**, 221-225.

58. X. Huang, Z. Yin, S. Wu, X. Qi, Q. He, Q. Zhang, Q. Yan, F. Boey, H. Zhang, *Small*, 2011, **14**, 1876-1902

59. Y. Zhu, S. Murali, W. Cai, X. Li, J.W. Suk, J.R. Potts, R.S Rauf, *Advanced Material,* 2010, **22**, 3906-3924.

60. A.K. Geim, K.S. Novoselov, *Nat. Mat.*, 2007, **6**, 18.

61. P. Mukhopadhyay, R.K Gupta, *CRC Press,* 2012, ISBN: 978-4398-2779-6. **9**, 271.

62. A.H.C Neto, F. Guinea, N.M.R. Peres, K.S. Novoselov, A.K. Geim, *Rev. in Modern*

Phys., 2009, **89**, 109.

63. S. Sarkar, E. Bekyarova, R.C. Haddon, *Accounts of Chem. Res.,* 2012, **45**, 673.

64. K.S. Novoselov, A.K Geim, S.V. Morovoz, D. Jiang, Y. Zhang, S.V. Dubonos, I.V. Griegorieva, A.A. Firsov, *Nature*, 2005, **438**, 197–200.

65. Y.B. Zhang, Y.W. Tan, H.L. Stormer, P.Kim, *Nature,* 2005, **438**, 201.

66. F. Schedin, A.K. Geim, S.V. Morovoz, E.W. Hill, P. Blake, M.I. Katsnelson, K.S. Novoselov, *Nat. Mat.,* 2007, **6**, 652.

67. K.S. Novoselov, S.V. Morovoz, T.M.G Mohinddin, L.A. Ponomarenko, D.C. Elias, R. Yang, I.I. Barbolina, P. Blake, T.J. Booth, D. Jiang, J. Giesbers, E. W. Hill, A.K. Geim, *Phy. Stat. Sol.*, 2007, **244**, 4106-4111.

68. T. Kuila, S. Bose, A.K. Mishra, P. Khanra, N.H. Kim, J.H. Lee, *Prog. In Mat. Sci.* 2012, **57**, 1061-1105.

69. C.D. Reddy, S. Rajendran, K.M. Liew, *Nanotech.* 2006, **17**, 864. [70] J-W. Jiang, J-S. Wang, B. Li, *Phy. Rev.* 2008, **80**, 113405.

70. J.P. Lu. *Phys. Rev. Lett.* 1997, **79**, 1297.

71. K.F Mak, M.Y. Sfeir, Y. Wu, C.H. Lui, J.A. Misewich, T.F. Heinz, *Phys. Rev. Lett.* 2008, **101**, 196405.

72. S. Niyogi, E. Bekyarova, M.E. Itkis, J.L Macwilliams, M.A. Hamaan, R.C. Haddon, *J. of American Chem. Soc.* 2006, **128**, 7720-7721.

73. H.J. Salavagione, G. Martinez, G. Ellis, *Macromol. Rapid Commun.* 2011, **32**, 1771-1789.

74. J.Y Lim, N.M. Mubarak, E.C. Abdullah, S. Nizamuddin, M. Khalid, Inamuddin, *J. of Ind. and Eng. Chem.,* 2018, **66**, 29-44.

75. W. Choi, I. Lahiri, Y. Seelaboyina, Y.S. Kang, *Critical Reviews in Solid States and Mat. Sci.,* 2010, **35**, 52-71.

76. Y. Zhong, Z. Zhen, H. Zhu, *Chem. Soc. Rev*., 2017, **46**, 4417-4449

77. C. Berger, Z. Song, X. Li, X. Wu, N. Brown, C. Naud, D. Mayau, T. Li, J. Hass, A.N. Marchenkov, E.H. Conrad, P.N. First, W.A. Heer, *Science,* 2006, **312**, 1191-1196.

78. Y. Miyamoto, K. Nakada, M. Fujita, *Phys. Review:B,* 1999, **59**, 9858-9861.

79. M. Fujita, K. Wakabayashi, K. Nakada, M. Fujita, K. Kusakabe, *J. of Phys. Soc. Japan,*

1996, **65**, 1920-1923.

80. S. Niyogi, E. Bekyarova, J. Hong, S. Khizroev, C. Berger, ‘’W. de heer’’. R.C. Haddon, *J of Phys. Chem. Lett.,* 2011, **2**, 2487-2498.

81. M. Delamar, R. Hitmi, J. Pinson, J.M Saveant, *J of American Chem. Soc.* 1992, **114**, 5883- 5884.

82. Y.C. Liu, R.L. Macreery, *J. of American Soc.* 1995, **117**, 11254-11259.

83. F. Li, X. Jiang, J. Zhao, S. Zhang, *Sci. Direct*, 2005, **16**, 488-515.

84. D. Rajamanickam, M. Shanthi, *Arabian J. of Chem*., 2012, **9**, 1858-1868.

85. R.S Dariani, A. Esmaeili, A. Mortezaali, S. Dehghanpour, *Optiks*, 2016, **127**, 7143-7154.

86. J. Lin, Z. Luo, J. Liu, P. Li, *Mat. Sci. in Semiconductor Processing,* 2018, **87**, 24-31.

87. S.K Tammina, B.K. Mandal, N.K. Kadiyala, *Env. Nanotech. Monitoring and Man.,* 2018, **10**, 339.350.

88. E. Bulut, M. Ozacar, I.A. Ongil, *Microporous and Mesoporous Materials*, 2008, **115**, 234–246.

89. Y.S. Ho, G. McKay, *Water Research*, 2000, **34**, 735–742.

90. J. Liu, J. Tang, J. J Gooding, *J. of Mat. Chem.* 2012, **22**, 12435.

91. The world’s worst pollution problem, The toxic beneath our feet, Green Cross Switzerland and Pure Earth, 2016.

92. J. Xu, B. Zhang, L. Jia, N. Bi, T. Zhao, 2020, *J. of Hazardous Mat*., 2020, **386**, 121630.

93. A. B. Habiba, Bangladesh Text. Today, 2022.

94. M. Ziatia, S. Hazourli, *Microchemical Journal*, 2019, **146**, 164–16.

95. J. Phiria, L-S Johanssona , P Ganea , T. Maloney, *Composites Part B* **147** (2018) 104–113

96. S. Sharma, J. H. Baik, C. J. Perera, and M. S. Strano, *Nano Lett*. 2010, **10**, 398-405.

97. S. Sarkar, 2012, *Mat. Today*, 15, 276-285

98. D. V. Potorochin, A. N. Chaika, O. V. Molodtsova, V. Y. Aristov, D. E. Marchenko, D. A. Smirnov, A. A. Makarova, B. Walls, K. Zhussupbekov, K. Walshe, I. V. Shvets, A. S. Ciobanu, M. K. Rabchinskii, N. V. Ulin, M. V. Baidakova, P. N. Brunkov, S. L. Molodtsov, *App. Surface Sci.* 2022, **585**, 152542

99. A. D. Broadbent, Basic Principles of Textile colouration, Society of dyers and colourist, 2001.

100. J. Shore, Colorants and auxiliaries, 1990, 2.

101. K McLaren, The Colour Science of Dyes and Pigments, 1986, 2.

102. P. Suppan Chemistry and Light, *Royal Society of Chemistry*, 1994.

103. General Introduction to the Chemistry of Dyes, *IARC* 2010

104. N. A. Romero and D. A. Nicewicz, *Chem. Rev*. 2016, **116**, 10075−10166.

107. Fukuzumi, S. and Ohkubo, K. *Chemical Science.* 2013, **4**, 2, 561-574.

108. Ohkubo, K., Suga, K. and Fukuzumi, S. *Chemical Communications.* 2006, **19**, 2018-2020.

109. M. L. Marin, L. S-Juanes, A. Arques, A. M. Amat, and M. A. Miranda, *Chem. Rev*. 2012, 112, 1710–1750.

110. J. Greenwood, T. H. Phan, Y. Fujita, Z. Li, O. Ivasenko, W. Vanderlinden, H. V. Gorp, W. Frederickx, G. Lu, K. Tahara, Y. Tobe, H. Uji-i, S. FL Mertens, and S. De Feyter. *ACS Nano,* 2015.

111. T. Patel, J Huang, K. Krukiewicz, *Biosensors and Bioelectronics:X*,

112. J. Pinson and F. Podvorica, *Chem. Soc. Rev*., 2005, **34**, 429.

113. M. Delamar, R. Hitmi, J. Pinson and J. M. Save´ant, *J. of Am. Chem.Soc*., 1992, **114**, 5883.

114. P. Allongue, M. Delamar, B. Desbat, O. Fagebaume,R. Hitmi, J. Pinson, and J-M Save´ant, *Carbon* 1997.

115. F. Farivar, P. L. Yap, R. U. Karunagaran, D. Losic *J of Carbon Research*, 2021.

116. M. Bagherzadeh A. Farahbakhsh, *Graphene materials: Fundamentals and emerging application*, 2015, ISBN 978-118-99837-3

117. C. K. Chua and Martin P., Covalent chemistry on graphene, *Chem. Soc. Rev*. 2013.**42**, 3222.

118. A. Bellunato, H. A. Tash, Y. Cesa, and G. F. Schneider, *Chem. Phys. Chem.,* 2016, **17**, 785 – 801.

119. J. Liu, L. Cui, D. Losic, *Acta Biomaterialia*, 2013, **9**, 9243–9257.

120. M. Shabbir, Z. A. Raza, T. H. Shah, M. R. Tariq, *J. of Nanostructure in Chem.* 2022 **12**, 1033–1051.

121. J. Han and C. Gao, *Nano-Micro Letters*, 2010, **2**, 213-226.

122. S-E Zhu, F. Li and G-W. Wang, *Chem Soc. Rev*. 2013, **42**, 7487–7740.

123. M. T. Baei, S. F. Rastegar & A. A. Peyghan, *Physics Letters A*, 2014, 378, 2184–2190.

124. C. Zhang, R. F. Li , Y. Liang, Z. Shang, G. Wang, Y. Xing, Y. Pan , Z. Cai, X. Zhao, C. Liu, *Journal of Molecular Structure*, 2006, **764**, 33–40.

125. X. Yang, F. Chen, M. A. Kim, H. Liu, L. M. Wolf and M. Yan, *Phys. Chem.chem.phys.* 2022, **24**, 20082-20093

126. R. B-Garrido, R. Rodriguez, M. A´ lvaro, H. Garcia, *Carbon,* 2014, **74,** 113-119.

127. K. E. Snell, H. Ismaili, and M. S. Workentin, *Chem. Phys. Chem* 2012, **13**, 3185 – 3193.

128. X. Yang , F. Chen , M. A. Kim, H. Liu, L. M. Wolf, and Mingdi Yan, Chem. Eur. J. 2021, **27**, 7887–7896.

129. P. Shukla, S. Mahata, A. Sahu, M. Singh, V. K. Rai and A. Rai, *RSC Adv*., 2017, **7**, 48723–48729.

130. C. Wentrup, *Acct. of Chem Res*. 2011, **44,** 393–404

131. P. G. Wenthold, *J. Org. Chem*. 2012, **77**, 208−214.

132. R. Belloli, *California State College Fullerton*, July 1971, 92631, **48**, 7.

133. M. S. Platz, *Acc. Chem. Res*. 1995, 28, 487-492.

134. S. Murata, Y. Tsubone, R. Kawai, D. Eguchi and H. Tomioka, J. Phys. Org. Chem.2005, **18**, 9–20.

135. R. Warmuth and S. Makowiec, *J. of Am. Chem. Soc*. 2007, **129**, 1233-1241.

136. K. Balasubramanian and M. Burghard, *small*, 2005, **1**, 180 –192.

137. C. A. Dyke, M. P. Stewart, F. Maya, J. M. Tour, *Synlett* 2004, 1, 155–160.

138. A. Bensghaïer, F. Mousli, A. Lamouri, P. S. Postnikov, M. M. Chehimi, *Chemistry Africa* 2020, **3**, 535–569.

139. R. L. McCreery in Electroanalytical Chemistry, New York, 1991, **17**. 221 – 374.

140 J. L., Bahr, J. M. Tour, J. of *Mater. Chem*. 2002, **12**, 1952.

141. X. T. Le, N. D. Doan, T. Dequivre, P. Viel and S. Palacin, *ACS Appl. Mater. Interfaces* 2014, **6**, 9085−9092.

142. D. O. Li, X. S. Chu, and Q. H. Wang, *Langmuir* 2019, **35**, 5693−5701.

142. L. Daukiya, J. Teyssandier, S. Eyley, S. El Kazzi, M. C. R. González, B. Pradhan, W. Thielemans, J. Hofkens S. D. Feyter, *nanoscale*, 2021, **13**, 2972-2981.

143. H. Jing, H. Yeo, B. Lyu, J. Ryou, S. Choi, J.-H. Park, B. H. Lee, Y.-H. Kim, and S. Lee, *ACS Nano* 2021, 15, 1388−1396.

144. D. L. Yun, L. Delphine, O. Li, H. Ming, J. Florence, G. Jean, P. C. Mangeney, *Adv. in Coll. and Int. Sci* 2021, 294, 102479.

145. J. Xu, M. Xu, J. Wu, H. Wu, W-H Zhang and Y-X Li, *RSC Adv*., 2015, 5, 72361–72368.

146. S. S. Rathnam, V. Tarun, A. Senthilguru, K. Biswaranjan, M. Chandra, S. B. Tapas K. M. Sumit, P. Kunal, P. Banerjee, *Materials Science & Engineering C*, 2020, 110, 110647.

147. H. Wang, Y. Wang, T. Deng, C. Chen, Y. Zhu, X. Hou, *Catalysis Communications,* 2015, 59 127–130.

148. R. Sharma, J. H. Baik, C. J. Perera, and M. S. Strano, *Nano Lett*. 2010, *10*, 398-405.

149. X. J. Leea, B. Yan, Z. Hiewa, K.C. Lai, L. Y. Leea , S. Gana, S. T.-Gopakumar, S Rigby, *J. of Taiwan Inst. of Chem. Eng.*, 2019, 98, 163-180.

150. R. S. Edwards and K. S. Coleman, *nanoscale*, 2013, **5**, 38.

151. K. E. Whitener Jr, P. E. Sheehan, *Diamond & Related Materials* 46, 2014, 25–34.

152. S. A. Bhuyan. N. Uddin, M. Islam, F. A. Bipasha, S. S. Hossain, *Int Nano Lett*, 2016, **6**, 65–83.

153. B. Jayesena, S. Subbiha, *Nanoscale Res. Lett*. 2011, **6**, (1), 95.

154 M. Yi, Z. Shen, *J of Mat. Chem A,* 2015, **3**, (22), 11700-15.

155. S. Chaitoglou, PhD project: 2016, Universitat DE Barcelona

156. Y. Chen, H. Zhao, L. Sheng, L. Yu, K. An, J. Xu, Y. Ando and X. Zhao, *Chem.*

Phys. Lett., 2012, **538**, 72–76.

157. K. S. Subrahmanyam, L. S. Panchakarla, A. Govindaraj and C. N. R. Rao, *J. Phys. Chem. C*, 2009, **113**, 4257–4259.

158. D. V. SmovzhIlya, A. KostogrudSalavat, Z. SakhapovAlexey, V. ZaikovskiiSergey A. Novopashin, *Carbon*, 2017, **112**, 97-102 .

159. B. Li, X. Song, P. Zhang, *Carbon*, 2014, **66** 426 – 435.

160. A. V. Zaikovskii, D. V. Smovzh, S. Z. Sakhapov, and A. V. Fedoseev, *J. of Physics*, 2018, 012135.

161. E. P. Randviir, D. A. C. Brownson and C. E. Banks, *Materials Today,* 2014

162. D. L. Mafra, Using inelastic scattering of light to understand the nature of electron-phonon interactions and phonon self-energy renormalizations in graphene materials, 2021.

163. Mitch Jacoby, *Material*, 2009.

164. U. A. M. Romero, M. Á. V. Soto, L. L. Jiménez, J. Á. Quintana and S. A. P. García, *Intech.,* 2017 4 81.

165. L. Staudenmaier, *Ber. Dtsch. Chem. Ges*., 1898, 31, 1481– 1487.

166. B. C. Brodie, *Philos. Trans. R. Soc. London*, 1859, 149, 249– 259.

167. W. S. Hummers and R. E. Offeman, *J. Am. Chem. Soc*., 1958, 80, 1339.

168. Szabó T, Berkesi O, Forgó P, Josepovits K, Sanakis Y, Petridis D, Dékány I, *Chem Mater* 2006, 18, 2740–9.

169. D. R. Dreyer, S. Park, C. W. Bielawski and R. S. Ruoff, *Chem. Soc. Rev*., 2010, 39, 228–240.

170. A. Lerf, H. He, M. Forster and J. Klinowski, *J. Phys. Chem. B*, 1998, 102, 4477–4482.

171. H. He, J. Klinowski, M. Forster and A. Lerf, *Chem. Phys. Lett*., 1998, 287, 53–56.

172. A. Buchsteiner, A. Lerf and J. Pieper, *J. Phys. Chem. B*, 2006, 110, 22328–22338

173. S. Revathi, M. Vuyyuru, m. D. Dhanaraju, *Asian j. of pharm. and clin. res.* 2015. 8, 1, 25-3.

174. D. A. C. Brownson and C. E. Banks, *Chem. Phys*., 2012, 14, 8264–8281.

175. X. J. LeeL. Y. LeeL. P. Y. FooK. W. TanD. G. Hassell, *J. of Env. Sci*. 2012, **24** 1559–1568.

176. R. M. Jacobberger, R. Machhi, J. Wroblewski, B. Taylor, A. Lynn, G.-Daniel, and M. S. Arnold, *J. of Chem. Educ*. 2015, **92**, 1903−190.

177. R. Muñoz and C. G-Aleixandre, *Chem. Vap. Deposition,* 2013, **19**, 297–322.

178. O. J. Wintterlin and M. L. Bocquet, *Surf. Sci*., 2009, **603**, 1841– 1852.

179. M. Batzill, *Surf. Sci. Rep*., 2012, 67, 83–115

180. S.-M. Kim, J.-H. Kim, K.-S. Kim, Y. Hwangbo, J.-H. Yoon, E.-K. Lee, J. Ryu, H.-J. Lee, S. Cho and S.-M. Lee, *Nanoscale*, 6, 4728 - 4734.

181. M. I. Kairi, M. Khavarian, S. A. Bakar, B. Vigolo, and A. R. Mohamed, *J Mater Sci* 2018, **53**, 851–879.

182. D. Wei, Y. Lu, C. Han, T. Niu, W. Chen, and A. T. S. Wee, *Angew. Chem. Int. Ed.* 2013, **52**, 14121 –14126.

183. N. Mishra, J. Boeckl, N. Motta, and F. Iacopi, *Phys. Status Solidi A*, 2016, **213**, 9.

184. G. R. Yazdi, T. Iakimov and Rositsa Yakimova, *Crystals* 2016, **6**, 53.

185. T. M. Hoang, Georgia Institute of Technology, *PhD Thesis*, 2017.

186. S. Tang, H. Wang , H. S. Wang, Q. Sun, X. Zhang, C. Cong, H. Xie , X. Liu , X. Zhou, F. Huang, X. Chen, T. Yu, F. Ding, X. Xie, & M. Jiang, *nature communications,* 2015, **6**, 6499.

187. Z. Liua , Q. Xua, C. Zhanga , Q. Suna , C. Wanga , M. Dongb , Z. Wangb , H. Ohmoric, M Kosinovad , Takashi Gotoa , Rong Tua , Song Zhang, *Applied Surface*

Science 2020, **514**, 145938.

188. R. Kumar, S. Sahoo, E. Joanni, R. K. Singh, W. K. Tane, K. K. Kar, A. Matsuda, *Progress in Energy and Combustion Science,* 2019, **75**, 100786.

189. H. Tan, D. Wang and Y Guo, *Coatings* 2018, **8**, 40.

190. S. A. Speakman, Basics of X-Ray Powder Diffraction, *MIT*, (617) 253-6887.

191. M. Hu, Z. Yao, and X. Wang, *Mat. Sci.* 2017, **4**, 3, 755-788.

192. Sun Z, Yan Z, Yao J, Beitler E, Zhu Y, Tour JM. *Nature* 2010, **468**, 549–52.

193. D. Geng, S. Yang, Y. Zhang , J. Yang , J. Liu, R. Li, T-K Sham, X. Sun, S Ye, S. Knights, *Applied Surface Science* 2011, **257,** 9193–9198.

194. F. Tavakoli, M. S-Niasari, A. badiei, F. Mohandes, *Materials Research Bulletin* 2015, **63,** 51–57.

195. Y. Ding, H. Shi, M. Zeng, and L. Fu, *Adv. Func. Mats.* 2022, 2202469.

196. A. Ibrahim, A. Klopocinska, K. Horvat and Z. A. Hamid, *Polymers* 2021, **13**, 2869.

197. Ferrari, A.C., *Solid State Commun*. 2007, **143**, 47–57.

198. G. Mariappan, N. Sundaraganesan, *J. of Mol. Str* 2014, **1063**, 192–202.

199. V. H. Harnisch, L. Ann. *Chem*., (1972), **765**, 8-14

200. P. Mucha, M. Małecka, B. Kupcewicz, K. Lux, A. Dołega, J. Jezierska, E. Budzisz, *Polyhedron* 2018, **153**, 181–196.

201. K. S. Mali, J. Greenwood, J. Adisoejoso, R. Phillipson and S. D. Feyter, *nanoscale*, 2015, **7**, 1566–1585.

202. J. Li, R. Cui, Y. Chang, H. Huang, X. Guo, J. Wang, R. Liu, K. Chen, J. Kong, G. Xing and B. Sun, *RSC Adv*., 2020, **10**, 36378–36385.

203. M. Gharbi, Z. H. Sun, P. Sharma, K. White, *App. Phy. Lett.* 2009, **14**, 95.

204. N. G. Shang, P. Papakonstantinou, S. Sharma, G. Lubarsky, M. Li, D. W. McNeill, A. J. Quinn, W. Zhoue and R. Blackley, *Chemical Communications*, 2012, **48**, 1877–1879.

205. D. Jariwala, A. Srivastava, and P. M. Ajayan, *Journal of Nanoscience and Nanotechnology,* 2011, **11**, 6621–6641.

206. A. Schedy , D. Quarthal, M. Oetken, *World Journal of Chemical Education*, 2018, 6, 1, 43-53.

207. H P Bei, Y. Yang, Q. Zhang, Y. Tian, X. Luo , M. Yang, and X. Zhao, *Molecules* 2019, **24**, 658

208. L. Yan, Y. B. Zheng, F. Zhao, S. Li, X. Gao, B. Xu, P. S. Weiss and Y. Zhao, *Chem. Soc. Rev*., 2012, **41**, 97–114.

209. X. Zhang, W. R. Browne, B. J. Van Wees, and B. L. Feringa, *Graphene Science Handbook, Fabrication Method*, 2016, 187-204, ISBN; 9781466591288.

210. J-M Seo and J-B Baek, *Chem. Commun*., 2014, **50**, 14651-14653.

211. J. Zhang, J. Wang, S. Wen, S. Li, Y. Chen, J. Wang, Y. Wang, C. Wang, X. Yu and Y. Mao, *Coatings* 2021, **11**, 251.

212. I. Khan, K. Saeed, I. Zekker, B. Zhang, A. H. Hendi , A. Ahmad, S. Ahmad , N. Zada, H. Ahmad, L. A. Shah, T. Shah and I. Khan, *Water* 2022, **14**, 242.

213. H.D. Bouras, Z. Isik, E.B. Arikan, A.R. Yeddou, N. Bouras, A. Chergui, L. Favier, A. Amrane, N. Dizge, *Int. J. Environ. Stud*. 2020, **78**, 365–381.

214. J. Zhang, Y. Zhang, Y. Lei and C. Pan, *Catal. Sci. Technol.* 2011, **1**, 273-278.

215. S. Sahu, S. Pahi, J. K. Sahu, U. K. Sahu, R. K. Patel, *Env. Sci. and Pol. Res.,* 2020 **27**, 22579–22592.

216. T. Soltani, M. H. Entezari, *Journal of Molecular Catalysis A: Chemical* 2013, **377**, 197–203.

217. A. B. dos Santos, F. J. Cervantes, J. B. van Lier, *Bioresource Technology* 2007, **98** 2369–2385.

218. J. O. Amode, J. H. Santos, Z. M. Alam, A. H. Mirza, C. C. Mei, *Int J Ind Chem* 2016

7 333–345.

219. Y. Kuang, X. Zhang, S. Zhou, *Water,* 2020, **12**, 587.

220. M. I. Din, R. Khalid, J. Najeeb, Z. Hussain, *Journal of Cleaner* Production 2021, **298** 126567.

221. B. H. Taymaz, R. Taş, H. Kamış, M. Can, *Polymer Bulletin* 2021, **78**, 2849–2865.

222. N.P. Mohabansi, V. B. Patil, and N.Yenkie, *RASAYAN J. of Chem,* 2011, **4**, 814-819.

223. M. Soniya, G. Muthuraman, *J. of Ind. and Eng. Chem.*, 2015, **30**, 266–273.

224. J. Pomicpic, G.C. Dancel, P.J. Cabalar, J. Madrid, *Radiat. Phys. Chem*. 2020, **172**, 108737.

225. Methylene Blue Market - Global Industry Analysis, Size, Share, Growth, Trends, and Forecast 2016 – 2024.

226. S.M. Siddeeg, M.A. Tahoon, W. Mnif, R. F. Ben, *Processes*, 2019, **8**, 5.

227. F. Arias, M. Guevara, T. Tene, P. Angamarca, R. Molina, A. Valarezo, O. Salguero, G. C. Vacacela, M. Arias, L.S. Caputi, *nanomaterials*, 2020, **10**, 681.

228. J. Cheng, C. Zhan, J. Wu, Z. Cui, J. Si, Q. Wang, X. Peng, L.S. Turng,. *ACS Omega* 2020, **5**, 5389–5400.

229. A. K. Moorthy, B. G. Rathi, S. P. Shukla, K. Kumar, V. S. Bharti, *Env. Toxic. and Pharmac.* 2021, **82,** 103552.

230. M. Contreras, C.D. Grande-Tovar, W. Vallejo, C. Chaves-López, *Water,* 2019, **11**, 282.

231. L. Sun, D. Hu, Z. Zhang, X. Deng, *Int. J. Environ. Res. Public Health,* 2019, **16**, 4773.

232. E. Santoso, R. Ediati, Y. Kusumawati, H. Bahruji, D.O. Sulistiono, D. Prasetyoko, *Mater. Today Chem*. 2020, **16**, 100233.

233. E.A. Abdelrahman , R.M. Hegazey, R.E. El-Azabawy, *J. Mater. Res. Technol.* 2019, 8, 5301–5313.

234. A.H. Jawad, A.S. Abdulhameed, M.S. Mastuli, *J. Taibah Univ. Sci*. 2020, **14**, 305–313.

235. L.F. Cusioli, H.B. Uesada, A.T.A. Baptista, R.G. Gomes, R. Bergamasco, *Environ. prog. sustainable energy,* 2020, **39**, 13328.

236. Staro ´n P., Chwastowski J., Banach M., *Int. J. Environ. Sci. Technol*. 2019, **16**, 8449–8460.

237. Lebron Y.A.R., Moreira V.R., de Souza Santos, L.V., *Environ. Technol*. 2019, **42**, 279–297.

238. Bharti V., Vikrant K., Goswami M., Tiwari H., Sonwani R.K., Lee, J., Tsang D.C.W., Kim K.H., Saeed M., Kumar S., *Environ. Res*. 2019, **171**, 356–364.

239. Zhou S., Du Z., Li X., Zhang Y., He Y., Zhang Y., *R. Soc. Open Sci*. 2019, **6**, 190351.

240. Lawagon C.P., Amon R.E.C., *Environ. Eng. Res*. 2019, **25**, 685–692.

241. Rashad M., Shaalan N.M., Abd-Elnaiem A.M., *Desalin. Water Treat*. 2016, **57**, 26267–26273.

242. Siong V.L.E., Lee K.M., Juan J.C., Lai C.W., Tai X.H., Khe C.S., *RSC Adv*. 2019, **9**, 37686–37695.

243. D. Heger, J. Jirkovsky, P. Kla´n, *J. Phys. Chem. A*, 2005, **109**, 30, 6703.

244. S. A. Raza, S. Q. Naqvi, A. Usman, J. R. Jennings, Y. W. Soon, *J. of Photochemistry & Photobiology, A: Chemistry* 2021, **418**, 113417.

245. J. Wei, R. Atif, T. Vo and F. Inam, *J. of nanomaterial*, 2015, 3.

246. S. Koltzenburg, M. Fraunhofer, O. N. Garching, Polymer Chemistry, *Springer-Verlag Berlin Heidelberg*, 2017, ISBN 978-3-662-49277-2, DOI 10.1007/978-3-662-49279-

6.

247. A Ravve, Principles of Polymer Chemistry, *Springer New York Heidelberg Dordrecht London,* 2012, ISBN 978-1-4614-2211-2, DOI 10.1007/978-1-4614-2212-9.

248. D. Braun, M. Rehahn, B. Voit, H. Cherdron, H. Ritter, Polymer Synthesis: Theory and Practice, *Springer Heidelberg New York Dordrecht London*, 2012, **5**, ISBN 978-3-642-28979-8, DOI 10.1007/978-3-642-28980-4.

249. G. ODIAN, Principles of Polymerization, *John Wiley Publication & Sons Inc. Hoboken, New Jersey* 2004, **4**, 1, ISBN 0-471-27400-3.

250. S. P. Davis, Biotech. In Agric. Ind. and Med., *Nova Sci. pub. Inc. NY.,* 2011, **71**, ISBN: 978-1- 61942-780-8.

251. P. Nechita, *Intech Open.* 2017, 209-228.

252. P.K. Dutta, J. Dutta and V. S. Triphathy, *J of Scientific and Industrial Research,* 2004, **63**, 20-31.

253. M. Ulbricht, *Polymer*, 2006 **47,** 2217–2262.

254. B.J. McCoy, *Sep Sci Tech.* 1995, **30**, 487.

255. D.K. Roper, E.N. Lightfoot. *J of Chrom. A.* 1995, **3** 702.

256. S.C.H. George, S.H. Thomas, *Prog Polym Sci.* 2001, **26**, 985.

257. W.J. Koros, A.H. Chan, D.R. Paul, *J Membr Sci* 1977 **2**, 165.

258. R.D. Noble, *J Membr Sci* 1992 **75,** 121.

259. Y.JI, G.M. Geise, *Ind. Eng. Chem. Res.* 2017, **56**, 7559−7566.

260. E. D. Revellame, D. L. Fortela, W. Sharp, R. Hernandez, M. E. Zapp, *Cleaner Eng. and Tech.*, 2020, **1**, 100032.

261. Y. Liu and L. Shen, *Langmuir* 2008, **24**, 11625-11630.

262 M. R. Khan, J. M. Khan, A. A. Alqadami, Spectrochimica Acta Part A: Molecular and Biomolecular Spectroscopy 2019, **206**, 72–77.

263. R. Jain, M. Mathur, S. Sikarwar, A. Mittal, *J. of Env.Man.*, 2007, **85,** 956–964.

264. D. Sun, X. Yang, *Food Anal. Methods,* 2017, **10**, 2046–2052.

265. G. H. Ayres, *J. of Analytical Chem.* 1949*,* **2,** 1, 6.

266. K. H. Leong, L. C. Sim, S. Pichiah and S. Ibrahim, nanoscience in Food and Agriculture 3, Sustainable Agriculture Reviews 23, 2016.

267. F. Mohamed, M. Shaban, S. K. Zaki, M. SElsamie, R. Sayed, M. Zayed, N.Khalid, S. Saad, S. Omar, A. M. Ahmed, A. Gerges, H. R.Abd ElMageed & N. K. Soliman, *Scientific reports,* 2022, **12**, 18031

268. Z. Shui, L. Yao, X. Pu, L. Yang, W. Jiang and X. Jiang, *Ind. Eng. Chem. Res*. 2020, **59**, 14616−14624.

269. W.A. Khandaya , F. Marrakchi a,b , M. Asif c , B.H. Hameed, Journal of the Taiwan Institute of Chemical Engineers 2017, **70**, 32–41.

270. R. Sadri, M. Hosseini, S. N. Kazi, S. Bagheri, M. Sayuti, M. Dahari, *Energy Conv. and Mngt.* 2017, **150** , 26-36.

271. M. Korivand, M. Zamani, *J. of Solid State Chem.* 2021, **294**, 121851

272. M. S. Ahmed, H. Begum, Y-Bae Kim, S. Jung *App. Surface Sci.* 2021 **536**, 147760.

273. V. G. S. Veerakumar, B. P. Shanmugavel, *Appl. Composite Mat.* 2021, **28**, 1127–1152

274. Chowdhury S., Balasubramanian R., *Advances in Colloid and Interface Science* 2014, ***204***, 35-56.

275. Zhu S., Huang X., Ma F., Wang L., Duan X., Wang S., *Environmental Science & Technology* 2018, ***52,*** 15, 8649-8658.

276. Saini D., Gunture, Kaushik J., Aggarwal R., Tripathi K. M., Sonkar S. K., *ACS Applied Nano Materials* 2021, **4**, 9303-9314.

277. Mollar-Cuni A., Ventura-Espinosa D., Martín S., García H., Mata J. A., *ACS*

Catalysis **2021**, 14688-14693

278. Sun H., Kwan C., Suvorova A., Ang H. M., Tadé M. O., Wang S., *Applied Catalysis B: Environmental* 2014, ***154-155***, 134-141.

279. Wang Y., Wang X. C., Antonietti M., *Angewandte Chemie-International Edition* 2012, **51**, 1, 68-89.

280. Baig N., Ihsanullah S. M., Saleh T. A., *J. of Environmental Management* 2019, **244**, 370-382.

281. Zhu Y., Murali S., Cai W., Li X., Suk J. W., Potts J. R., Ruoff R. S., *Advanced Materials* **2**010, **22**, 35, 3906-3924.

282. Kuila T., Bose S., Mishra A. K., Khanra P., Kim N. H., Lee J. H., *Prog. in Mat. Sci.* 2012, **57**, 7, 1061-1105.

283. Hu M., Yao Z., Wang X., *Ind. and Eng. Chem. Res.* 2017, **56**, 13, 3477-3502.

284. Li F., Zhang L., Tong J., Liu Y., Xu S., Cao Y., Cao S., *Nano Energy,* 2016, **27**, 320-329.

285. Xiong H., Jewell L. L., Coville N. J., *ACS Catalysis,* 2015, **5,** 4, 2640-2658

286. Albero J., Mateo D., García H., *Molecules,* 2019, **24**, 5, 906,

287. Quintanilla A., Carbajo J., Casas J. A., Miranzo P., Osendi M. I., Belmonte M., *Catalysis Today* 2020, **356**, 197-204.

288. Wang M., Cai L., Wang Y., Zhou F., Xu K., Tao X., Chai Y., *J. of American Chem. Soc.* 2017, **139**, 11, 4144-4151.

289. Xiang Q., Yu J., Jaroniec M., *Chem. Soc. Rev.* 2012, **41**, 2, 782-796.

290. Lee C., Wei X., Kysar J. W., Hone J., *Science* 2008, **321**, 5887, 385-388.

291. Zhang J., Dai L., *ACS Catalysis* 2015, **5**, 12, 7244-7253.

292. Mali K. S., Greenwood J., Adisoejoso J., Phillipson R., De Feyter S., *Nanoscale* 2015, **7**, 5, 1566-1585,

293. Englert J. M., Dotzer C., Yang G., Schmid M., Papp C., Gottfried J. M., Steinrück H.-P., Spiecker E., Hauke F., Hirsch A., *Nature Chemistry* 2011, **3**, 4, 279-286.

294. Ju H.-M., Huh S. H., Choi S.-H., Lee H.-L., *Materials Letters* 2010, **64,** 3, 357-360.

295. Huh S. H., *Carbon* 2014, **78**, 617-621.

296. I. Kaura , S. Yadavb , S. Singhc , V. Kumard , S. Arorae , D. Bhatnagarf, *Solid State Phenomena,* 2015, **222**, 99-116.

297. Q Tang, Z. Zhou and Z. Chen, *Nanoscale*, 2013, **5**, 4541.

298. Z. Sun, D.o Guo, S. Wang, C. Wang, Y. Yu, D. Ma, R. Zhengb and P. Yan, *RSC Adv*., 2016, **6**, 65422.

299. T. M. Radadiya, *European J. of Mat. Sci*., 2015, 2, 1, 6-18.

300. Dalian institute of chemical physics, chinese academy sciences, 2022.

301. O. F. Unsal and A. C. Bedeloglu, 2018, *Mat. Sci. Res. India*, 15, pp 114-130

Appendix

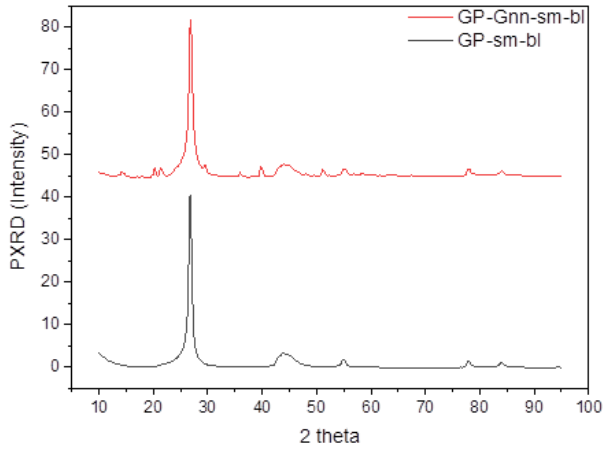

Figure 3.16: PXRD spectra of pristine graphene and Graphene-Guanine

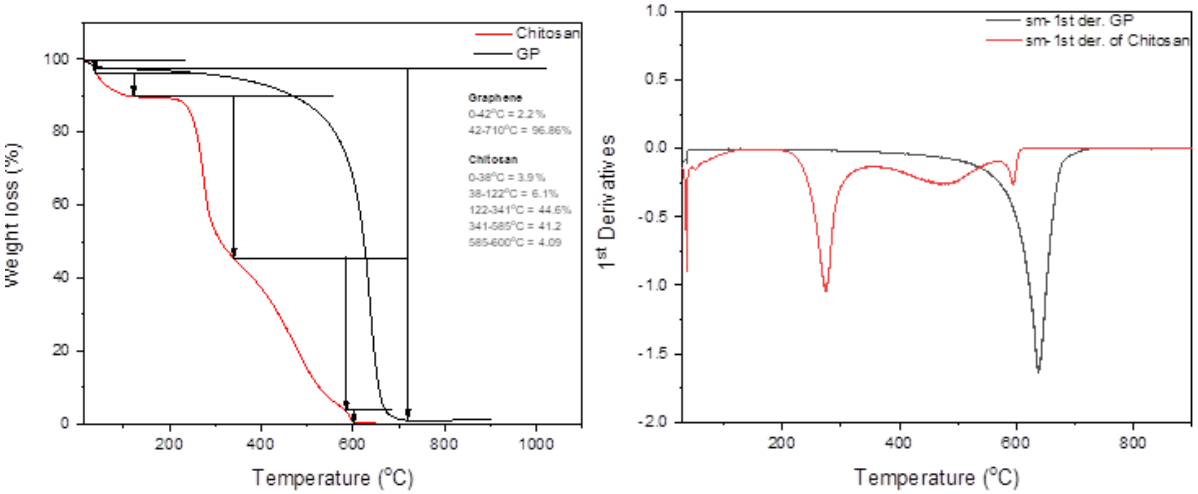

Figure 3.17: TGA analysis (left) Weight loss (%) and (right) Normalized 1st Derivatives of Graphene and Chitosan

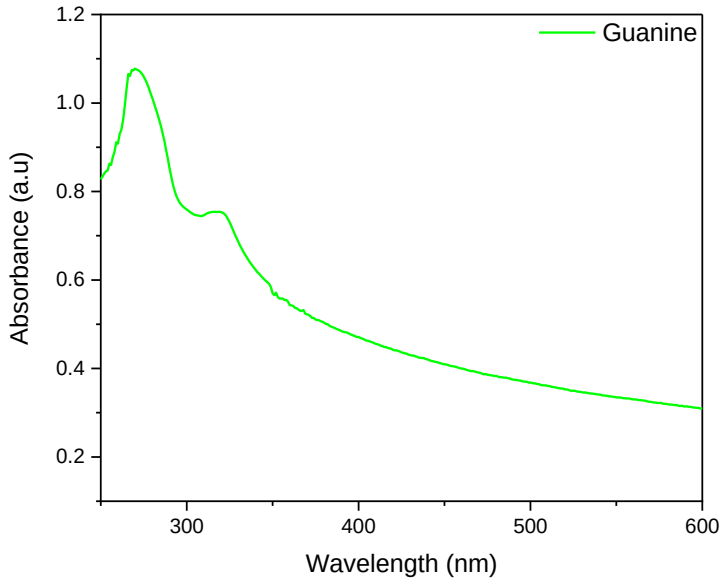

Figure 3.18: UV-Vis spectrum of guanine dye

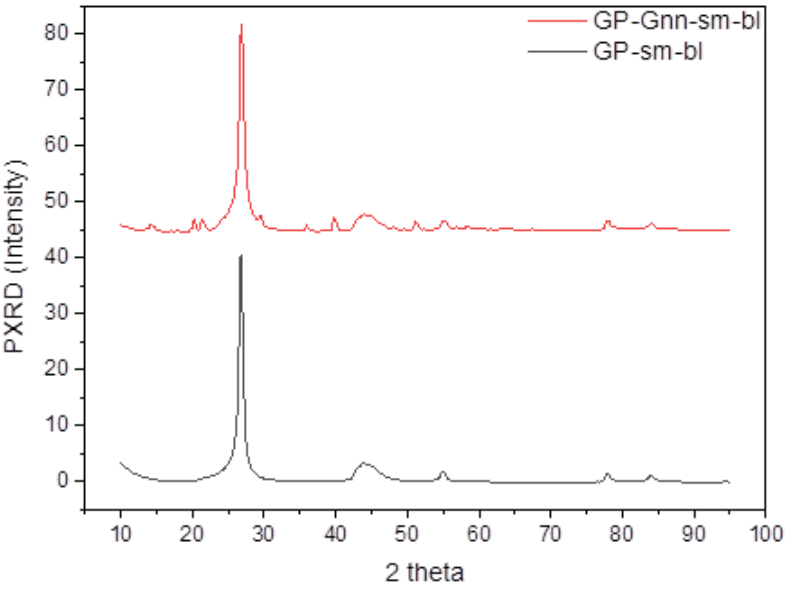

Figure 2.16: PXRD spectra of pristine graphene and Graphene-Guanine

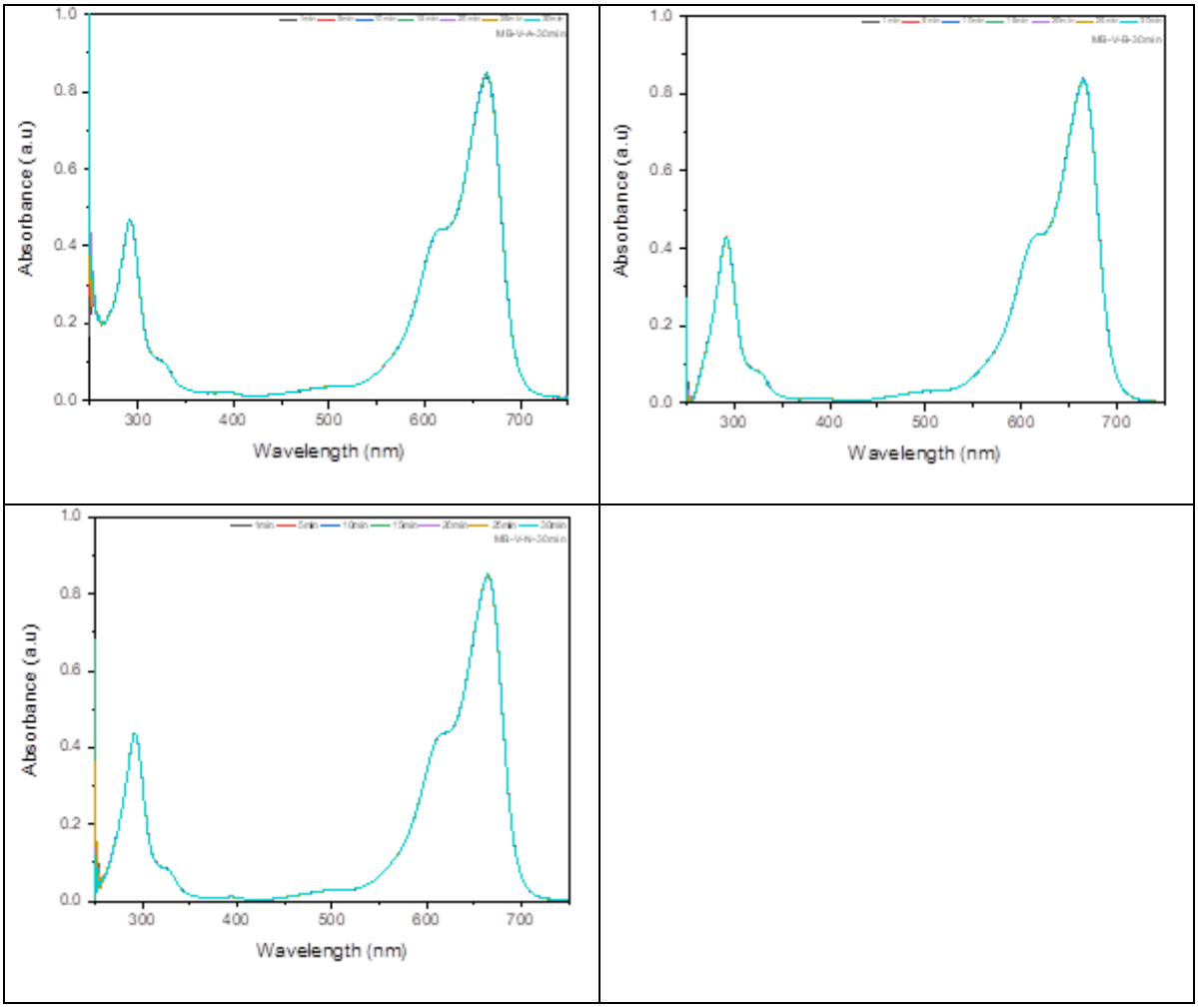

Figure 4.11. Photostability of MB under acidic, basic and Neutral condition with 75W for 30min

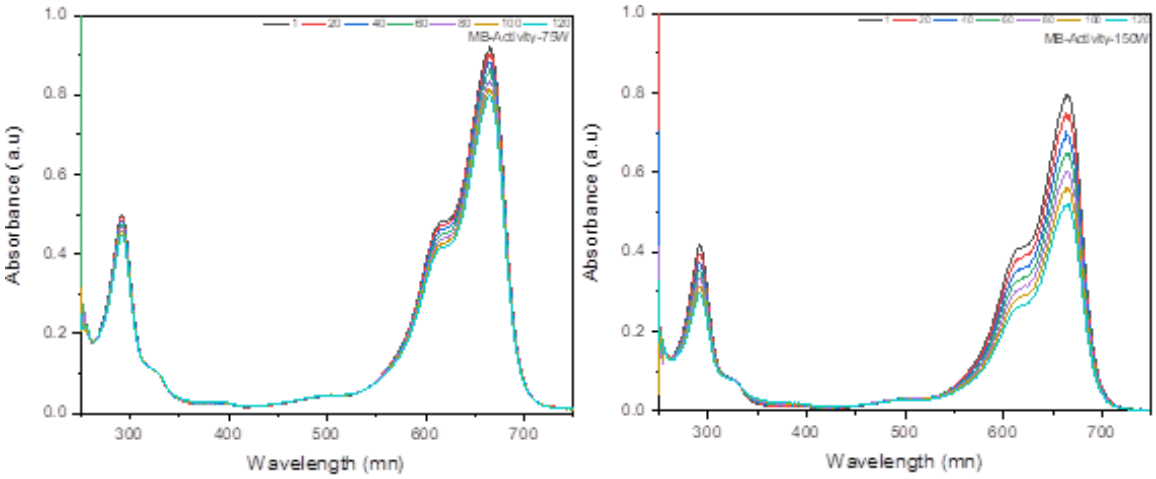

Figure 4.12. Photostability of MB under 75W and 150W light source

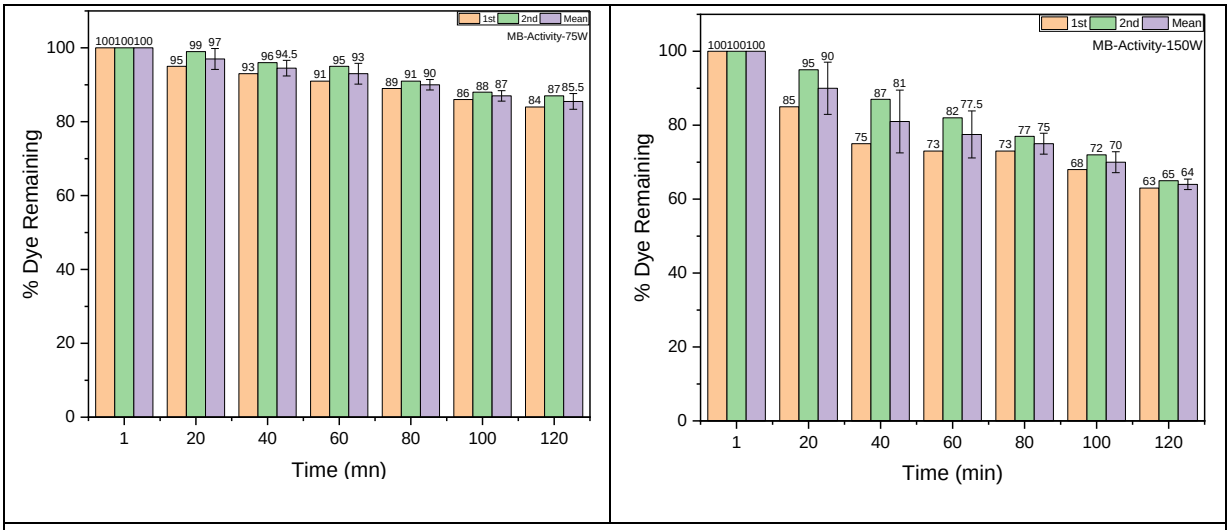

Figure 4.13. Photostability of MB under 75W and 150W light source

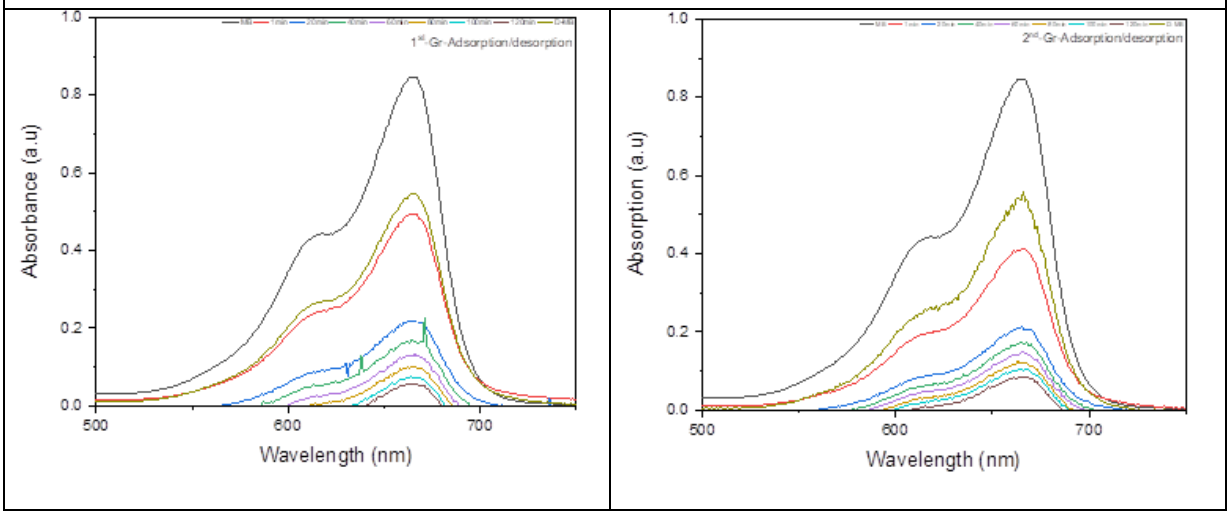

Figure 4.14: Plot of Adsorption/desorption of MB on Graphene under light (75W) and neutral condition for 120min (2 runs)

Mass loading MB

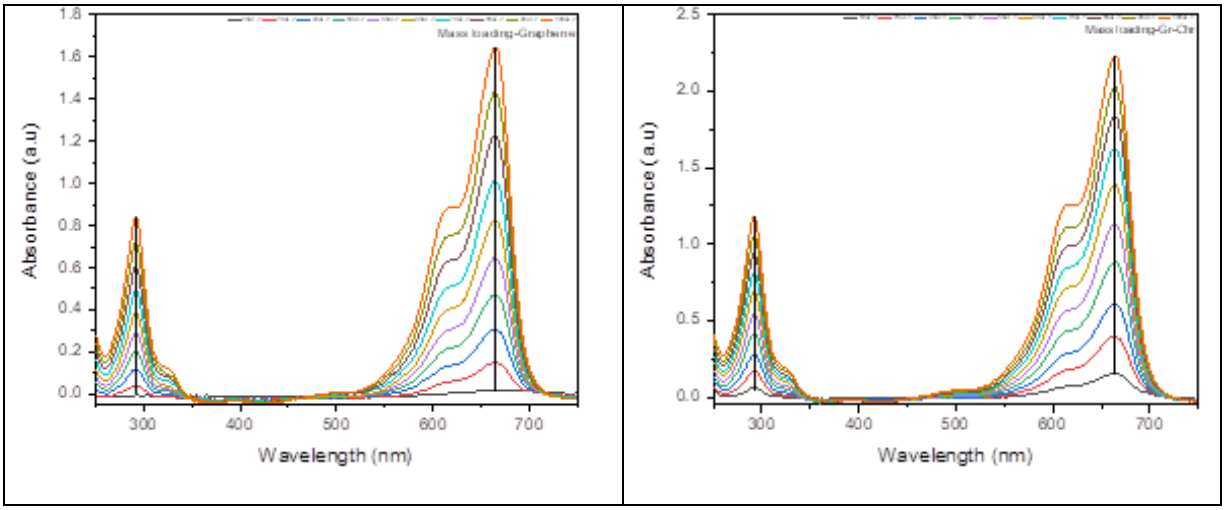

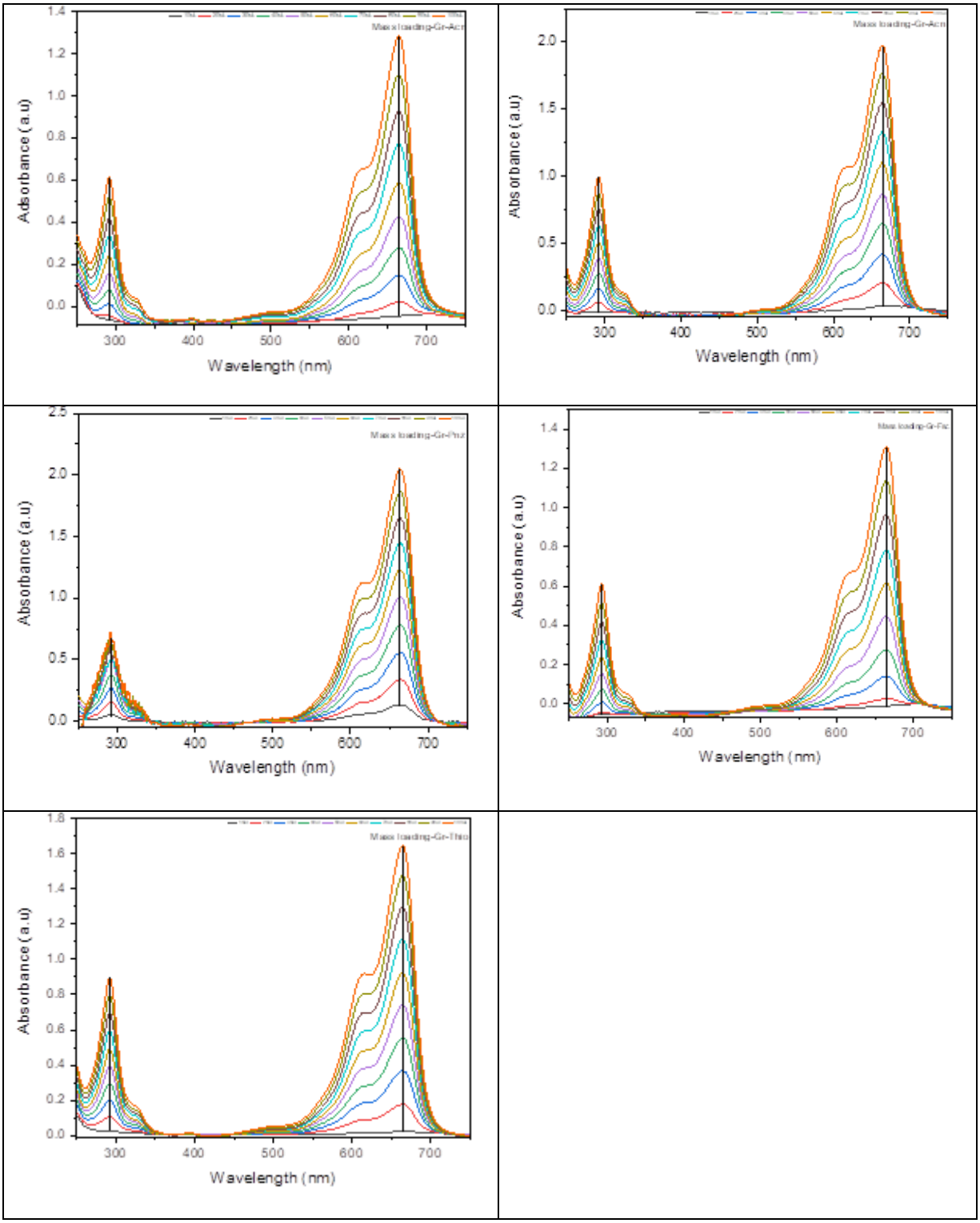

Figure 4.14: Plots of mass loadings of MB on different catalysts

Mass loading (RhB)

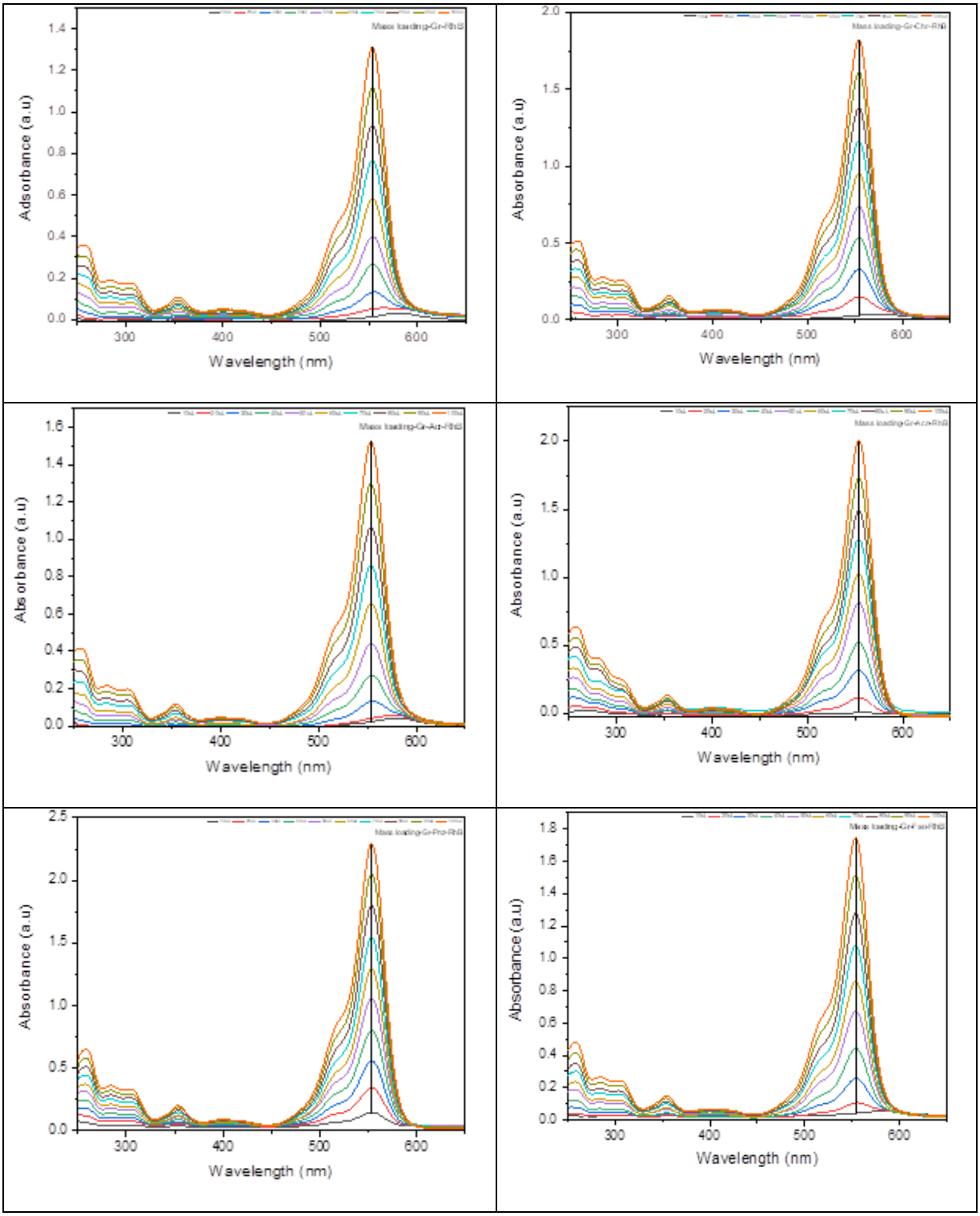
Absorbance (a.u)
Wavelength (nm)
300
400
500
600

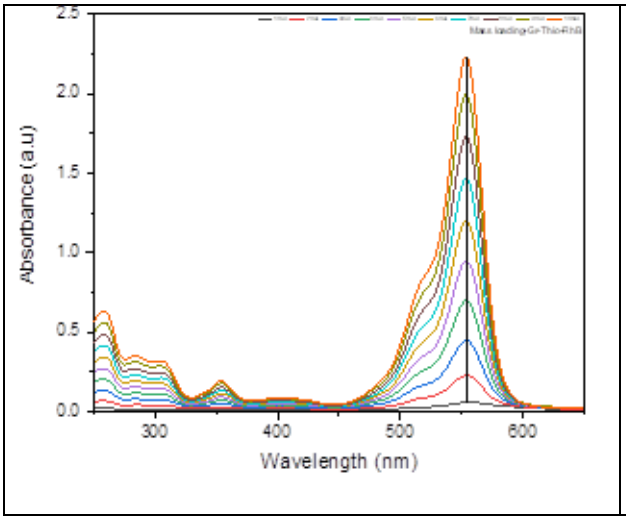

Figure 4.15: Plots of mass loadings of RhB on different catalysts